Fall 1975

NEUTRON MEASUREMENTS AT BALLOON ALTITUDES USING ORGANIC SCINTILLATORS AND APPLICATION FOR GAMMA-RAY MEASUREMENTS

CHIA YU CHEN

Follow this and additional works at: https://scholars.unh.edu/dissertation

INFORMATION TO USERS

This material was produced from a microfilm copy of the original document. While the most advanced technological means to photograph and reproduce this document have been used, the quality is heavily dependent upon the quality of the original submitted.

The following explanation of techniques is provided to help you understand markings or patterns which may appear on this reproduction.

1. The sign or "target" for pages apparently lacking from the document photographed is "Missing Page(s)". If it was possible to obtain the missing page(s) or section, they are spliced into the film along with adjacent pages. This may have necessitated cutting thru an image and duplicating adjacent pages to insure you complete continuity.

2. When an image on the film is obliterated with a large round black mark, it is an indication that the photographer suspected that the copy may have moved during exposure and thus cause a blurred image. You will find a good image of the page in the adjacent frame.

3. When a map, drawing or chart, etc., was part of the material being photographed the photographer followed a definite method in "sectioning" the material. It is customary to begin photoing at the upper left hand corner of a large sheet and to continue photoing from left to right in equal sections with a small overlap. If necessary, sectioning is continued again — beginning below the first row and continuing on until complete.

4. The majority of users indicate that the textual content is of greatest value, however, a somewhat higher quality reproduction could be made from "photographs" if essential to the understanding of the dissertation. Silver prints of "photographs" may be ordered at additional charge by writing the Order Department, giving the catalog number, title, author and specific pages you wish reproduced.

5. PLEASE NOTE: Some pages may have indistinct print. Filmed as received.

76-11,678

CHEN, Chia Yu, 1947-
   NEUTRON MEASUREMENTS AT BALLOON ALTITUDES
   USING ORGANIC SCINTILLATORS AND APPLICATION
   FOR GAMMA RAY MEASUREMENTS.

   University of New Hampshire, Ph.D., 1975
   Physics, atmospheric science

Xerox University Microfilms, Ann Arbor, Michigan 48106

NEUTRON MEASUREMENTS AT BALLOON ALTITUDES USING ORGANIC

SCINTILLATORS AND APPLICATION FOR GAMMA RAY MEASUREMENTS

by

CHIA YU CHEN

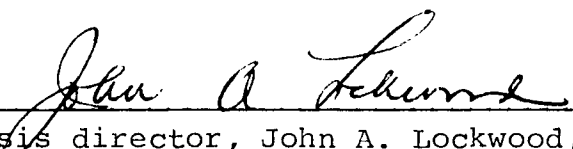B.S., Cheng Kung University,   1969

M.S., University of New Hampshire,   1972
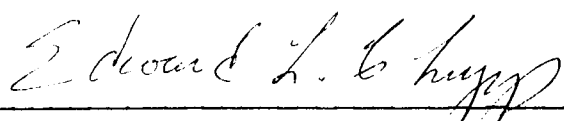
A THESIS
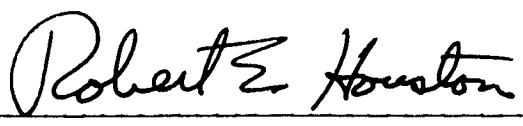
Submitted to the University of New Hampshire

In partial Fulfillment of

The Requirements for the Degree of

Doctor of Philosophy

Graduate School

Department of Physics

September, 1975

This thesis has been examined and approved.

Thesis director, John A. Lockwood, Prof. of Physics

Edward L. Chupp, Prof. of Physics

Robert E. Houston, Prof. of Physics

William R. Webber, Prof. of Physics

Harvey Shepard, Assoc. Prof. of Physics

November 26 1976

Date

ACKNOWLEDGEMENTS

I would like to express my deepest gratitude to
Dr. John Lockwood for providing me the opportunity to be
involved in this work and giving me his guidance, assistance,
and encouragement throughout whole work.

Appreciation is extended to Mr. Lawrence Friling
and Mr. Richard Simmons for their excellent technical support
which made the experiment successful.

Thanks are due to Dr. Aaron Galonsky and Dr. Robert
Doering of Michigan State University for their generous
assistance and corporation which made the calibrations
avalible.

I am also grateful to Dr. Richard N. St. Onge for
his invaluable discussions, Dr. David Klumpar for his assis-
tance in the initial phase of the work, Mr. Lwo Hsieh for
his assistance in the data analysis and Miss Janet Varney in
drafting.

I am gladly to acknowledge the constant encourage-
ment and assistance of my wife, Lee Lyne.

DEDICATION

To my parents

TABLE OF CONTENTS

ABSTRACT

NEUTRON MEASUREMENTS AT BALLOON ALTITUDES USING ORGANIC

SCINTILLATORS AND APPLICATION FOR GAMMA RAY MEASUREMENTS
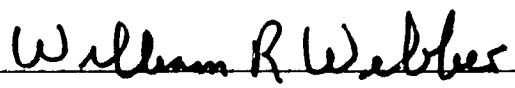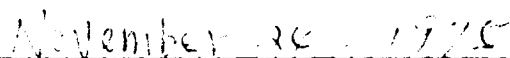
by

CHIA YU CHEN

The neutron differential energy spectrum at altitudes

from 4.2 g/cm^2 to 2.9 g/cm^2 has been measured by two liquid

organic cylindrical scintillators (NE213) during a balloon

flight at Palestine, Texas, $\lambda=42^{\circ}N$ on June 22, 1973. These

detectors were calibrated at the University of New Hampshire

Van der Graaf accelerator and at the Michigan State University

cyclotron. Experimental response functions from calibrations

are used to unfold the observed neutron spectrum.

The neutron leakage current spectrum measured in

this flight normalized to sunspot minimum at $E_n=2$ Mev is

$0.065 \, {}^{+0.014}_{-0.012}$ neutrons/cm^2-sec-Mev, and at $E_n=10$ Mev is

$3.1 \times 10^{-3} \, {}^{+7.5 \times 10^{-4}}_{-7.2 \times 10^{-4}}$ neutrons/cm^2-sec-Mev. From $E_n=2$ Mev

to $E_n=10$ Mev the spectrum can be described by a power law

energy spectrum with an index of -1.9. From 10 Mev to 75

Mev the spectrum required to fit the data must be much

flatter. At $E_n=50$ Mev the leakage current is $7.1 \times 10^{-3} \, {}^{+2.3 \times 10^{-3}}_{-1.3 \times 10^{-3}}$

neutrons/cm^2-sec-Mev. Between 20 Mev and 50 Mev the neutron

leakage current spectrum from our measurement is approximately

a factor of 3 lower than the measurement of White et al. (1972),

but about a factor of 8 higher than the calculations of

Lingenfelter (1963b) at 50 Mev.

A computer program using the Monte Carlo technique
to unfold the measured gamma ray spectrum was developed and
applied to the gamma ray data obtained. A prototype neutron-
gamma ray telescope system was also included which incorporated
a time of flight system between the two detectors and used
the double scattering technique to measure the directional
fluxes and energy spectra of neutrons and gamma rays.

CHAPTER I

INTRODUCTION

Atmospheric neutrons are produced in the earth's atmosphere by the bombardments of galactic and solar cosmic rays. It was also suggested that solar neutrons produced during a solar flare could reach the earth (Biermann, 1951). For solar neutron measurements a directional detector is necessary because solar neutron fluxes from most flare events do not exceed the background of atmospheric neutrons. Up to now there is no positive evidence of any solar neutrons from solar flares. Some of the neutrons produced in the atmosphere degrade in energy to become thermal neutrons and are then absorbed by nitrogens through the reaction $N^{14}(n,p)$ C^{14} to produce C^{14} which is used as an age-dating agent. Since the discovery of the radiation belts much effort has been made to understand the behavior of the trapped radiations. A theory proposes that some atmospheric neutrons escape and subsequently decay in the magnetosphere into protons, electrons, and anti-electron neutrinos and become the source of the energetic protons and electrons trapped in the Van Allen radiation belts (Singer, 1958a, 1958b). To test this theory it is essential to have the information about the source strength. The purpose of this experiment is to measure the neutron source strength directly.

Measurements of this source have not been pushed very far until very recently. Many of the early measurements

used slow neutron (below 20 kev) detectors with hydrogenous

moderators to measure the fast neutrons (1 Mev to 10 Mev)

(Bame et al. 1963, Albert et al. 1962). This method suffers

from serious background problems, as well as very low

efficiency for detecting high energy neutrons. The scintil-

lator technique, which is much more efficient, suffers from

the problem of contamination by gamma rays (Forrest, 1969).

The breakthrough came with the development of the pulse-shape

-discrimination (PSD). By the PSD technique one can identify

the different charged particle types interacting in the scin-

tillator (St. Onge, 1969a). Consequently, the neutron meas-

urements are relatively free of background counts and are more

reliable.

Most neutron measurements are in the energy range

below 10 Mev and there are not many measurements in the energy

range 20 Mev to 75 Mev. The recent measurements of White

et al. (1972) and Klumpar et al. (1973) indicate that the

theoretical predictions of Lingenfelter (1963b) are not

appropriate in the energy range above 10 Mev (Fig. 10-1, Fig.

10-2).

In this balloon flight we used two organic liquid

scintillators (NE213) to measure both omniderectional and

directional fluxes of atmospheric neutrons in the energy range

2 Mev to 75 Mev and the particular interest is in the region

20 Mev to 75 Mev.

The composition of NE213 is $CH_{1.213}$. The cross

section of the neutron-proton (n-p) scattering is well known

but cross sections of inelastic scatterings of neutron-carbon, such as $C^{12}(n,\alpha)Be^9$, $C^{12}(n,n3\alpha)$, $C^{12}(n,p)B^{12}$ ..., etc., which are important for neutrons with energies above 20 Mev are poorly known. To have reliable response functions of the detectors, both detectors were extensively calibrated by neutron beams from accelerators (Chapter VII). The calibrated response functions reveal several mistakes in the widely used theoretical neutron efficiency calculations (Kurz, 1964; Stanton, 1971). We used these calibrated response functions to unfold the observed neutron spectrum. It shows a significant difference between our results and previous measurements in the region 20 Mev to 75 Mev. The neutron leakage current from this measurement is about a factor of three lower than that measured by White et al. (1972) and by Klumpar et al. (1973) (Chapter X).

Since the pulse shape discrimination technique was incorporated into the electronics of both detectors, we were able to separate the electrons produced by gamma rays from the protons and the alpha particles produced by neutrons. By this technique, the balloon flight data can be displayed in a three dimensional matrix (Fig. 5-2, Fig. 5-3) and the electron recoil spectrum and the proton recoil spectrum in each matrix can be extracted (Chapter IX). It is possible to use the electron recoil spectrum to unfold the incident gamma ray spectrum. A technique using the Monte Carlo method to calculate the gamma ray response function of a detector has been developed in this laboratory for the gamma

ray spectral unfolding (Appendix B1). In this Monte Carlo
calculation we consider the multiple scattering effect of a
gamma ray, the Landau fluctuations of the energy loss, the
escape effect and the self gating effect of electrons and
positrons. The importance of this calculation is in its
ability to predict the escape effect and the self gating
effect of electrons and positrons. These two effects are
important when the effective ranges of electrons or positrons
are comparable to the size of a detector. Because we have not
calibrated extensively the detectors with high energy gamma
ray beams, we do not have the calibrated response functions
to compare with the response functions calculated by the Monte
Carlo method. Consequently, the gamma ray spectrum unfolded
by the Monte Carlo technique is not included in this thesis.

We also incorporated a time of flight system between
the two detectors. Using the double scattering technique,
the time of flight system and the two detectors form a proto-
type telescope system. This prototype telescope system was
used as a test for the large telescope system in the coming
balloon flight to measure the directional fluxes of neutrons
and gamma rays (Appendix A).

CHAPTER II

THE PRODUCTION AND THE TRANSPORT OF ATMOSPHERIC NEUTRONS

Atmospheric neutrons are produced by the interaction of primary and secondary cosmic rays with air nuclei. Most neutrons with energies less than 10 Mev are produced by nuclear evaporation, in which the air nucleus is excited during the interaction and is deexcited by emitting one or more nucleons. The neutrons from this process are isotropic in the center of mass system. Most neutrons with energies higher than 10 Mev are produced in the knock-on process. In this process the incoming cosmic ray interacts with only a few nucleons in the nucleus and gives part of its energy to one or several nucleons. The direction of the knock-on neutrons are in the direction of the incident cosmic ray. The ratio of neutrons with energies less than 10 Mev from evaporation to neutrons from the knock-on process with energies greater than 10 Mev is estimated to be four to one (Hess et al., 1961).

Protons emitted from the sun during a solar proton event may reach the earth's atmosphere and interact with the air nuclei, consequently producing neutrons. Lingenfelter (1964) showed that 90% of these neutrons are produced by the solar protons with energies greater than 100 Mev. But this source does not make a big contribution to the protons trapped in the radiation belts (Hess et al., 1966).

Most neutrons produced in these processes are moving away from the places where they are produced. As far as the

neutrons are concerned, the whole space may be regarded as
a neutron field and the life history of these neutrons can
be described by the Boltzmann transport equation.

Let the neutrons per unit volume in the energy
interval E, E+ΔE, flight directions in a unit solid angle
around unit vector $\hat{\Omega}$ and with the position vector $\vec{r}$ be
$n(\vec{r},\hat{\Omega},E)$, then the differential neutron flux $F(\vec{r},\hat{\Omega},E)$ equals
$n(\vec{r},\hat{\Omega},E)$ v, where v is the velocity of the neutron. The
neutron flux is $\phi(\vec{r},E)=\int_{4\pi} F(\vec{r},\hat{\Omega},E)\ d\Omega=n(\vec{r},E)$ v. In
a certain volume element dV the neutron leakage out of dV
is $\nabla\cdot[\hat{\Omega}\ F(\vec{r},\hat{\Omega},E)]$ dV dΩ dE$=\hat{\Omega}\cdot \nabla F(\vec{r},\hat{\Omega},E)$ dV dΩ dE.
The loss due to absorption and scattering into other directions
is $\Sigma_t(E,\vec{r})\ F(\vec{r},\hat{\Omega},E)$ dV dΩ dE, where $\Sigma_t(E,\vec{r})$ is the total
cross section. The gain due to in-scattering of neutrons from
other directions and energy intervals is

$\int_{4\pi}\int_0^\infty \Sigma_s(\hat{\Omega}'\to\hat{\Omega},E'\to E,\vec{r})\ F(\vec{r},\hat{\Omega}';E')\ d\Omega'\ dE'$ dV dΩ dE,
where $\Sigma_s(\hat{\Omega}'\to\hat{\Omega},E'\to E,\vec{r})$ is the cross section for scattering from
$\hat{\Omega}'\to\hat{\Omega}$ and $E'\to E$.
The production of neutrons by sources in dV is
$S(\vec{r},\hat{\Omega},E)$ dV dΩ dE.
These contributions give the time rate of change of the
differential density,

$$\partial n(\vec{r},\hat{\Omega},E)/\partial t=-\hat{\Omega}\cdot \nabla F(\vec{r},\hat{\Omega},E)-\Sigma_t(E,\vec{r})\ F(\vec{r},\hat{\Omega},E)+$$

$$+\int_{4\pi}\int_0^\infty \Sigma_s(\hat{\Omega}'\to\hat{\Omega},E'\to E,\vec{r})\ F(\vec{r},\hat{\Omega}',E')\ d\Omega'\ dE'+$$

$$+S(\vec{r},\hat{\Omega},E) \qquad\qquad (1)$$

This integro-differential equation is the Boltzmann transport equation (Beckurts et al., 1964).

In the early measurements of Hess et al. (1959), it was found that the neutron energy spectrum from sea level to within 200 g/cm^2 for energies from thermal to 500 Mev was an equilibrium spectrum. Since the atmospheric neutrons are in an equilibrium state, the Boltzmann transport equation can be simplified to

$$S(\vec{r},\hat{\Omega},E) = \hat{\Omega} \cdot \nabla F(\vec{r},\hat{\Omega},E) + \Sigma_t(E,\vec{r}) \ F(\vec{r},\hat{\Omega},E) -$$

$$- \int_{4\pi} \int_0^\infty \Sigma_s(\hat{\Omega}' \to \hat{\Omega}, E' \to E, \vec{r}) \ F(\vec{r},\hat{\Omega}',E') \ d\Omega' \ dE' \quad (2)$$

In the energy region below 10 Mev, Hess et al. (1961) used the diffusion approximation to solve this equation. In their calculations the principle source was a neutron evaporation spectrum $N(E) \ dE \propto E \exp(-E/\theta)$, where θ was chosen to be 1 Mev to agree with the neutron spectrum arising from 190 Mev protons incident on carbons (Gross, 1956). For knock-on neutrons with energies greater than 10 Mev, about 52% were degraded to less than 10 Mev and a ratio of evaporation to knock-on sources of 4.1 was found necessary to give the experimental ratio of fluxes in the knock-on region to the evaporation region. So the source for the diffusion calculation was an evaporation source strength R, plus a contribution from the knock-on source of magnitude 0.52 x R/4.1. In addition, the altitude distribution of the source function was assumed by Hess et al. to be the same as for the equilibrium neutron flux: $S(E,x) \propto \exp(-x/155)$, where x is the atmospheric

depth in g/cm^2.

Lingenfelter (1963a) recalculated the neutron strength
in the atmosphere using the altitude dependence from the
rate of production of cosmic ray stars in emulsions versus
altitudes observed by Lord (1951). Both Hess et al. and
Lingenfelter used the multigroup diffusion theory to carry
out the calculations. Hess et al. (1961) used the absolute
neutron fluxes in the atmosphere at depthes 200 g/cm^2 to 1030
g/cm^2. Lingenfelter used the various neutron measurements
at different altitudes, latitudes and times in the solar
activity cycle to normalize the calculated neutron spectrum.
In his calculation he also predicted the variations of neutron
spectra with altitude, latitude, and solar cycle.

Newkirk (1963) used another approach to solve the
problem. He began directly from equation (2) and rewrote it

to be $\quad S(\vec{r},\hat{\Omega},E) + \int_{4\pi}\int_0^\infty \Sigma_s(\hat{\Omega}'\to\hat{\Omega},E'\to E,\vec{r}) \ F(\vec{r},\hat{\Omega},E) \ d\Omega' \ dE'$

$$= \hat{\Omega}\cdot\nabla F(\vec{r},\hat{\Omega},E) + \Sigma_t(E,\vec{r}) \ F(\vec{r},\hat{\Omega},E)$$

The left hand side describes neutrons from cosmic ray disin-
tegrations occuring in the atmosphere and neutrons that
scattered down from higher energies. To solve this equation,
the equation was reduced to a system of linear differential
equations. The integration over the angle in the transport
equation was replaced by a summation over a discrete number
of directions. This method is known as S_n method. In his
calculations, Newkirk used an angular distribution derived
from the experiments of Miyake et al. (1957) and the altitude

dependence from Lord's experiment (1951) for the source neutrons. The calculation was normalized to one neutron measurement which was done at $\lambda=57°N$ in 1960, but no solar modulation was considered.

Another approach to solve the neutron transport problem is to use the Monte Carlo technique. In this method the galactic cosmic rays are followed from the moment they enter the atmosphere. The different reactions they have with the air nuclei are registered. The nuclear reactions and the electromagnetic cascade due to the original primary cosmic rays are shown vividly during the propagation of the particles. This is a very natural way to solve the problem if the cross sections of all reactions are well known. Wilson et al. (1969) used a Monte Carlo transport calculation and found that two pronounced peaks at about 2.5 Mev and 4.9 Mev and two apparent points of inflection at about 6.6 Mev and 9 Mev on the atmospheric neutron spectrum. They attributed these to the nuclear resonance structures of oxygens and nitrogens. Merker (1972) and Armstrong et al. (1973) used the Monte Carlo technique to simulate the galactic protons and alphas incident isotropically on the top of the atmosphere, assumed to be an infinite slab with thickness 1033 g/cm^2. In the calculations of Armstrong et al. (1973), the production and the transport of protons, charged pions, and neutrons were simulated by the Monte Carlo method. At each nuclear interaction the energy, the direction, the number of the interaction products and the recoil energy, the charge, and

the mass of the residual nucleus were determined. The parti-
cles produced might be protons, neutrons, charged pions and
neutral pions from the intranuclear cascade and protons, neu-
trons, deuterons, tritons, He^3 nuclei, and alpha particles
from the evaporation process. The produced neutral pions
were assumed to decay, but the two gamma rays emitted were
not traced. Because gamma rays do not play a significant
role in the production of neutrons. Particles from the evapo-
ration process with mass numbers greater than one were assumed
to have no more nuclear interactions. The neutrons were
divided into two major groups, above 12 Mev and below 12 Mev,
and treated separately. Neutrons and protons above 12 Mev
and charged pions above 1.8 Mev were followed until they
escaped from the atmosphere or had nuclear interactions, or
in the case of charged pions, decayed. Protons produced with
energies below 12 Mev and charged pions below 1.8 Mev were
not traced. For neutrons with energies below 12 Mev the
neutrons were divided into 57 spatial intervals and 32 energy
groups. In these 32 energy groups upscattering was allowed
and neutrons could gain as well as lose energy in the colli-
sions with nuclei. It was necessary to consider this in order
to properly predict the shape of the neutron spectrum near
thermal energy. In the very first step if the incident
particle was an alpha particle an approximate model (Gabriel
et al. , 1971) was used in which an alpha particle was assumed
to be four separate nucleons, with each nucleon having a
kinetic energy equal to one-quarter of the difference between

the kinetic energy and the binding energy of the alpha parti-
cle. Each nucleon entered the nucleus separately and independ-
ently, except for their relative spatial locations when they
entered the nucleus. The neutron spectrum was calculated
at geomagnetic latitude 42°N for solar minimum activity. At
0 g/cm^2, for neutrons in the energy range less than 10 Mev,
this calculation shows a good agreement with the calculations
of Lingenfelter (1963b), but for neutrons with energies
higher than 10 Mev this calculation predicts a considerable
higher neutron flux (Fig 10-1).

CHAPTER III

REVIEW OF EARLIER NEUTRON MEASUREMENTS

As indicated in Chapter I, if neutron leakage from the
atmosphere and subsequent decay in the magnetosphere is the
source of the Van Allen radiation belts, then it is essential
to determine the source strength. Many neutron measurements
have been conducted in the last 25 years at different altitudes,
latitudes and times in the solar activity cycle. The large
number measurements yield different results but if these
results are corrected to the same altitude, latitude, solar
cycle and converted correctly to a neutron leakage current,
then a large number of results are in better agreement. The
status of fast neutron leakage measurements has been reviewed
by Lockwood (1973). At 10 Mev, except for the results of
Baird et al. (1966) the differential energy fluxes agree to
±25% (Lockwood, 1973). All the measurements at 1 Mev are in
general agreement. Before 1972, most neutron measurements
were limited to the neutron energy range below 10 Mev. Recent-
ly, the neutron measurements have been extended to high energy
region (>10 Mev), but there are few measurements. The general
tendency indicates that the spectrum cannot be extrapolated
from the measurements in the 1 Mev to 10 Mev region. Some of
the experimental results of neutron measurements are converted
to the neutron leakage current, corrected to $\lambda=42^{\circ}N$, solar
minimum, and plotted in Fig. 10-1 and Fig. 10-2. The recent

measurements are briefly reviewed in the following. The values of corrected neutron leakage currents of some measurements are given for comparison.

Holt et al. (1966) conducted seven balloon flights between September 1964 and August 1965 at geomagnetic latitudes ranging from $8°N$ to $69°N$ at altitudes of about 4 g/cm^2. A phoswich type detector incorporating pulse shape discrimination was used in these measurements. In their phoswich type detector, a liquid scintillator (NE213 or NE218) was surrounded by a plastic scintillator (NE102) and both were viewed by a single photomultiplier tube. The pulses produced by charged particles in the plastic NE102 had similar characteristics of the pulses produced by electrons in the liquid scintillator. In the case that a charged particle produced in the liquid scintillator escaped into the plastic NE102 the combined pulse produced also had a similar pulse shape to that of an electron. Thus, they pulse-shape-discriminated pulses with pulse shapes of protons from the pulses with pulse shapes of electrons and obtained the proton recoil spectrum induced by neutrons. From these measurements the neutron spectrum in the energy range of 1 Mev to 10 Mev was described by a power law with index -1.05 ± 0.15. Later, Merker et al. (1973) summarized all measurements by balloons and by aircrafts from 1964 to 1971 and described the average spectrum as a power law with index $-1.08^{-0.13}_{+0.2}$ at 3 g/cm^2 to 5 g/cm^2. The corrected neutron leakage current, from 1 Mev to 10 Mev, was 0.16 ± 0.01 neutrons/cm^2-sec.

Haymes (1964) applied the phoswich technique to a NE213 scintillator surrounded by a CsI(Tl) layer and measured the spectrum from 1 Mev to 14 Mev during a series of balloon flights up to the altitudes about 3.6 g/cm^2 at $\lambda=41^{\circ}$N. A power law differential energy spectrum with index -1.3 ± 0.1, and the corrected neutron leakage current, from 1 Mev to 14 Mev, 0.13 ± 0.02 neutrons/sec-cm^2 were measured.

Albernhe et al. (1969) used stilbene surrounded by a plastic charged particle shield to measure atmospheric neutrons from 3 Mev to 14 Mev. From two balloon flights at $\lambda=46^{\circ}$N and altitudes of 4.2 mb and 4.5 mb the spectra measured were described again by power law spectra with indices -1.23 and -1.25 respectively. The corrected neutron leakage current from 3 Mev to 14 Mev was 0.12 ± 0.03 neutrons/sec-cm^2.

Baird et al. (1966) used a phoswich technique on a cylindrical crystal of Anthracene surrounded by a plastic scintillator of NE102 to measure neutrons from 2 Mev to 11 Mev at Fort Churchill in 1964-1965. Six rocket flights and two balloon flights were made. From two balloon flights at depths greater than 100 g/cm^2 the power law indices -1.35 ± 0.3 and -1.42 ± 0.3 were obtained by assuming that the spectra did not change with altitudes. The result of rocket flights yeilded an index of -0.8 and the corrected neutron leakage current from 2 Mev to 11 Mev was 0.25 ± 0.10 neutron/sec-cm^2.

Jenkins et al. (1971) conducted neutron measurements in the 1 Mev to 10 Mev range on the OGO-6 satellite from June 7 to September 30, 1969. The detector was a He^3 filled

proportional counter surrounded by the plastic scintillator which acted as a charged particle guard counter and a neutron moderator. From measurements in the polar region ($P_c \leq 0.3$ GV) the index of the power law spectrum was limited to be within -1 and -0.8. At equatorial regions ($P_c \geq 12$ GV) the upper limit of the index was -1.2. The corrected neutron leakage current from 1 Mev to 10 Mev was 0.16 ± 0.02 neutrons/sec-cm^2.

Klumpar et al. (1973) flew a 5 cm x 5 cm cylindrical liquid scintillator NE213 completely surrounded by a NE102 charged particle shield. Pulse shape discrimination was also incorporated in the NE213 scintillator which covered the proton energy range from 3 Mev to 18 Mev. It was concluded from two balloon flights that the power law spectrum in energy with a single index could not be fitted to the results (St. Onge, 1968). Instead, as shown in Fig. 10-2, the spectrum became flat from 10 Mev to 20 Mev.

White et al. (1972) reported the measurements on a balloon flight made at Palestine, Texas, $\lambda=40^\circ$N on 26 September, 1971. The double scattering method used two banks of liquid scintillators filled with NE223 spaced 100 cm apart. Each bank contained 8 cells and a charged particle shield surrounded each bank. Both the energy spectrum and the angular distribution were obtained. The differential energy spectrum reported was flat from 20 Mev to 50 Mev and from 50 Mev to 90 Mev the flux dropped by a factor of two (Fig. 10-1, Fig. 10-2).

Heidbreder et al. (1970) applied the double scattering technique to spark chambers and made measurements at

Palestine, Texas at an atmospheric depth 7 g/cm^2 on September 15, 1969. Out of the 17 valid events, 10 upward moving events were used to construct the neutron albedo differential energy spectrum from 100 Mev to 400 Mev. The corrected leakage current at 100 Mev is about 6 x 10^{-5} neutrons/sec-Mev-cm^2. Kanbach et al. (1974) extended the measurements of Heidbreder et al. from 70 Mev to 250 Mev. From the two balloon flights in May, 1971 at Palestine, Texas at altitudes 8.6 g/cm^2 and 4.7 g/cm^2 they found that the neutron leakage rate was 2.53 x $E_n^{-1.89}$ neutrons/sec-Mev-cm^2.

In Fig. 10-1, we also show the predicted neutron spectrum of Freden et al. (1962), which is derived from the measured inner radiation belt proton spectrum. The magnitude has been increased by a factor of 7 to take care of the injection coefficient (White et al., 1972).

CHAPTER IV

DETECTION PRINCIPLES FOR NEUTRONS

Since neutrons are neutral particles and do not interact with matter through Coulomb interaction, techniques for the neutron detection involve detecting the secondary particles produced by the neutrons. Some of the fast neutron detection principles are reviewed in the following.

The earliest type of detectors were BF_3 gaseous proportional counters. The cross section of $B^{10}(n,\alpha)Li^7$ for neutrons with energies less than 30 kev can be described as

$$\sigma = 3840 \times 2.2 \times 10^5 / v \quad \text{barns}$$

where σ is the cross section and v is the velocity of the neutron in cm/sec. For fast neutrons, the cross section is very small but an improvement can be made by slowing down the fast neutrons before they reach the counter. Based on this idea the BF_3 filled gaseous counter surrounded by a moderator has been used for the fast neutron detector. It has the inherent disadvantage that no spectral information is obtained.

In an attempt to deduce some spectral information about the neutrons, He^3 proportional counters were developed. He^3 has a large cross section, about 5400 barns, for thermal neutrons. The cross section of the reaction ($He^3 + n \rightarrow H^3 + p + 765$ kev) varies smoothly without resonances. Because there are no excited daughter products, the reaction products have the entire energy, so the energy of the neutron can be

measured. The major disadvantage of this reaction arises
from the competing effect of the elastic scattering between
the neutron and the He^3, which has a cross section of approxi-
mately twice that of the reaction $He^3(n,p)H^3$. To use this
reaction in the fast neutron detection neutrons are usually
moderated before they reach the detector. With the low
efficiency, however, it has been used for spectral measurements
in the region E_n < 10 Mev.

To extend the energy range of neutron detectors,
nuclear emulsions were developed specifically for the neutron
detection. The neutrons interact with elements in the emul-
sion, usually by a resonance capture reaction, and produce
charged particles which are detected. Alternatively hydro-
genous material, or radiator, can be placed in front of the
emulsion and the ranges of proton recoils determined so that
a neutron energy spectrum can be unfolded. In the case where
the neutron direction is known through collimation; the energy
and the direction of the neutron are then determined simulta-
neously.

For high energy neutron measurements, the spark cham-
ber technique can be used. The system usually consists of
hydrogenous radiators, a spark chamber, and stereoscopic
cameras. When neutrons interact with the radiators, recoil
protons are produced. The high voltage of the chamber causes
sparks along tracks of the protons, so the ranges and the
directions of the protons are determined. Using the informa-
tion provided by these tracks, energies and directions of

neutrons can be derived.

Semiconductors have also been used for neutron detectors. The semiconductor is sensitive to charged particles, and it can be used in an analogous fashion to an emulsion. A radiator is placed in front of the detector and the charged particle produced by the neutron in the radiator is detected in the semiconductor. The resolution of the detector is good, but in order not to absorb the energy of the charged particle the radiator has to be very thin. Consequently the efficiency is low.

The scintillators are widely used for neutron detectors. Since the technique of placing a radiator in front of a detector is not efficient, the scintillator gets around this problem by combining the radiator and the detector. When a neutron interacts with the material of the scintillator, it may produce a charged particle; the charged particle then loses energy through ionizations and molecular excitations in the scintillator itself. Some of the excited molecules emit light as they return to the ground state. By collecting the ligh output, the recoil particle can be detected, and if no other particles are incident, it is inferred that the neutron produced the recoil. Because in many kinds of scintillators different charged particles produce different shapes of light pulses, it is possible to use the pulse shape discrimination technique to identify the charged particles interacting in a scintillator. Consequently, in most cases, identify the type of the incident particle (Chapter V). The scintillator

technique was chosen for the measurements described in this thesis.

CHAPTER V

DESCRIPTION OF NEUTRON AND GAMMA RAY DETECTORS USED IN

THIS EXPERIMENT

The detector system follows the basic design of
St. Onge (1968). Improvements have been made in the pulse
shape discrimination (PSD), electronics system, and charged
particle anti-coincidence system. In this system the neutron
and gamma ray measurements are made reliable by the applica-
tion of the PSD to the organic scintillators by the technique
described in the section 5.1.

5.1 PULSE SHAPE DISCRIMINATION

Because neutrons and gamma rays are neutral particles,
neutron measurements may often be contaminated by gamma rays.
For atmospheric gamma ray measurements the neutron contamina-
tion is not a serious problem because the neutron flux is
relatively low compared with the gamma ray flux. But for
cosmic gamma ray measurements, because of the low intensity,
the neutron contamination problem is not negligible. Especial-
ly, when neutrons interact with the detector system and
produce local gamma rays. Sometimes this problem is even
more difficult to handle than the cosmic gamma ray measure-
ment itself.

The discovery of the different decay times associated
with different charged particles in organic scintillators
makes it possible to identify the types of particles by the
shapes of the light pulses produced in the scintillator

(Lynch, 1968; Kuchnir et al., 1968; Owen, 1959; Phillips et al., 1953; Wright, 1956). This possibility offers an unique opportunity to separate the electrons produced by gamma rays from the other charged particles (p, α, C, etc.) induced by neutrons. The significant progress made in this PSD technique not only makes neutron and gamma ray measurements more reliable but also makes it possible to measure them both simultaneously in the same detector.

In many organic scintillators, for example, stilbene, NE213, NE218, NE213M, etc., the scintillation pulses decay with combination of four decay constants; T1, T2, T3, and T4. For NE213, the values of four decay constants are 1.66, 3.16, 32.2, and 270 nanoseconds respectively (Lynch, 1968). Different charged particles produce pulses with different durations in the three periods with decay constants T2, T3, and T4. The duration of the first period with decay constant 1.66 nanoseconds is the same for different charged particles. From the observations that T1 is changed with the concentration of the solute in the scintillator only, it is explained that T1 is the mean life for the energy transfer from solvent to solute. Since the time for the excited molecules to go back to the ground state is in the order of nanoseconds while the time for ionized molecules to be neutralized is in the order of 10^{-7} seconds, the second period with decay constant T2 and the fourth period with decay constant T4 are attributed to the excitation of molecules and the recombination of the ionized molecules, respectively. Since the durations of

period two, three, and four are dependent upon the particle

type, if we integrate the scintillation pulse (for 30 microsec-

onds, in our case) then the time T between the beginning

of the pulse and the time at which the integrated pulse

reaches some fixed fraction of its final average value is

only dependent on the particle type. By this characteristic

time T the particle type is identified.

5.2 DESCRIPTION OF DETECTOR

In Fig. 5-1, we show the schematic drawing of the

detector system used in this flight. The system consisted

of two cylindrical cells filled with liquid scintillant NE213,

manufactured by Nuclear Enterprises, Inc. The composition of

NE213 is $CH_{1.213}$ and the density is 0.867 g/cc. One of the

cells has dimensions of 4.65 cm diameter by 4.60 cm length

(2 inch detector); the other 12.3 cm diameter by 12.3 cm

length (5 inch detector). Each detector was viewed by a fast

photomultiplier tube (RCA8575) and the detector was complete-

ly surrounded by a plastic charged particle shield, or anti-

coincidence dome (ACD), which was made of NE102 (St. Onge,

1969b). To be very sensitive to charged particles each ACD

was viewed by two photomultiplier tubes (RCA C70132A) and

operated in anti-coincidence or coincidence with the detector

so the events due to neutral particles or external charged

particles were measured respectively. The PSD technique

was applied to identify the types of charged particles and,

consequently, to separate events due to neutrons from those

due to gamma rays.

When an event occurred in the detector, an integrated
pulse from dynode 10 was fed into a double-delay-line (DDL)
amplifier. The bi-polar pulse from the DDL amplifier had
a pulse width proportional to the characteristic time T of
the light pulse (Section 5.1). The zero cross-over technique
was applied in the time-single-channel analyzer (TSCA). When
the zero point of the bi-polar pulse reached the TSCA, a
pulse was generated. The output pulse from the TSCA was fed
into the start terminal of the time-to-amplitude converter
(TAC). The TAC has two input terminals: one for a start pulse
and the other for a stop pulse. From the output of the TAC
a pulse is generated; the amplitude of which is proportional
to the time difference between the start pulse and the stop
pulse. The fast pulse from the anode was fed into the
constant fraction pick-off (CFPO) which gave a signal when
the pulse reached 10% of its maximum amplitude. The CFPO
reduced the random walk problem usually occuring in the
constant pulse-height triggering method. The pulse from the
CFPO was delayed for 1 microsecond by the gate & delay gener-
ator (G&DG). The pulse from the G&DG was fed into the TAC
for the stop pulse. So the amplitude of the output pulse
from the TAC was proportional to the characteristic time T of
the light pulse from the detector. Hence, this pulse was
used to identify the particle type. We then fed this pulse
to the pulse-shape-PHA of the two dimensional PHA. To measure
the energy loss of the particle in the event a unipolar signal
was taken from the DDL amplifier and sent to the pulse-height

PHA of the two dimensional PHA to measure its pulse height. So the particle type and the energy loss were known simultaneously. The reason we did not use the fast pulse from the anode for a start pulse of the TAC is because there are usually many small noise-pulses in the anode. Too much dead time will be created in the TAC if these noise-pulses trigger the TAC.

A time-of-flight (TOF) system was incorporated between the 2 inch detector and the 5 inch detector. For an event due to a neutral particle occurring in the 2 inch detector the fast pulse from the anode served as a start pulse for the TAC of the TOF system (TOF/TAC) and opened the gate of TOF/TAC for 40 nanoseconds. During this period, if a neutral event occurred in the 5 inch detector, then the fast pulse from the anode of the photo tube of the 5 inch detector was delayed for 20 nanoseconds and then fed into the TOF/TAC to serve as a stop pulse. The reason for delaying the stop signal for 20 nanoseconds is because the TAC has the characteristic that for the time differences less than 20 nanoseconds the amplitude of the output pulse is the same. Only for time differences greater than 20 nanoseconds is the amplitude of the output pulse proportional to the time difference. The output pulse from the TOF/TAC was fed into a 64-channel time-of-flight PHA (TOF/PHA) to analyze the pulse height. If during these 40 nanoseconds an event occurred in the ACD of the 2 inch detector, or 5 inch detector, then the system was turned off for 4 microseconds.

Logic pulse from the ACD of the 2 inch detector and from the ACD of the 5 inch detector were fed into the control logic. In the control logic a time sharing system was used so that in one second, 0.1 second was used to analyze events which were detected when the ACD and the detector were in the conincidence mode, and 0.9 second was used to analyze events obtained when the ACD and the detector were in the anti-coincidence mode. The logic signals from control logic were fed into the TOF/PHA, the two dimensional PHA of the 2 inch detector, and the two dimensional PHA of the 5 inch detector.

It took 55 microseconds to analyze an event, and the information was transmitted in series to telemetry output.

Because the PSD technique was applied to both detectors the events detected by the 2 inch detector, or by the 5 inch detector, could be displayed in a matrix according to their energies and particle types (Fig. 5-2, Fig. 5-3). In each matrix all data fell into four bands; each band corresponded to one particle type. They were identified as electrons, protons, alpha particles, and light pulses of an in-flight-calibrator (IFC) (Fig. 5-2). The IFC was a small NaI crystal doped with Am^{241} which decays by emitting alpha particles with a half life of 458 years. The alpha particles lose energy in the NaI crystal and produce light pulses with fairly constant amplitude and very different pulse shape. Thus, the IFC could be used to monitor the stability of the PHA (St. Onge et al., 1969a, 1969b).

In each flight matrix, there were 128 channels for the pulse height and 128 channels for the pulse shape. In order to extract the electron band and the proton band from a flight matrix it was necessary to print all data on a pulse height versus pulse shape matrix, recognizing that a two dimensional matrix is equivalent to the top view of a three dimensional matrix. In each two dimensional matrix we determined the valley between the electron peak and the proton peak, and then could draw the boundaries for the electron band and the proton band. Since the resolution of the pulse shape PHA was not perfect, there was a dispersion in the pulse shape channels for each pulse height channel so that in each band, at every pulse height channel we summed all counts in the pulse shape channels and determined an energy loss spectrum over the 128 pulse height channels for both protons and electrons. From calibrations the relation between proton energies and pulse height channel numbers was found so that it was possible to convert the pulse height spectrum in counts per channel to counts per energy interval for either particle species.

CHAPTER VI

SPECTRAL UNFOLDING TECHNIQUES FOR NEUTRONS

A single omnidirectional detector behaves similarly to a recoil-proton scintillation spectrometer provided that the proton energy loss spectrum is extracted by the pulse shape discrimination technique from electrons, protons, and alpha particles produced. This spectrum can then be related to the spectrum of incident neutrons. Our goal is to deduce the spectrum of incident neutrons from the recoil proton spectrum. There are several techniques to unfold the neutron spectrum, but only two methods used in this experiment will be discussed.

6.1 GENERAL METHOD

The most reliable method is to send a monoenergetic neutron beam into the detector and observe the recoil proton spectrum, which is the response function. By knowing the response functions of the detector to the neutrons with energies in the range we are interested, we can then use a least squares test technique to deduce the neutron spectrum which produces the proton recoil spectrum best fitting the observed recoil spectrum (Chapter IX). We obtained the calibrated response functions from the accelerator calibrations (Chapter VII) and used this method to unfold the neutron spectrum measured in this balloon flight.

6.2 Monte Carlo Method

Another method to have the response functions needed

for the neutron spectrum unfolding is by the Monte Carlo
calculations. This technique is a very reasonable way to
learn the details of various neutron reactions in the detector
provided that we have accurate information about the cross
section for each reaction. This method automatically takes
care of multiple scattering and the resolution of the detector
system. The Monte Carlo calculations for neutrons in a
scintillator used here was originally written by Stanton (1971).
We used the response functions calculated by the Monte Carlo
method to compare with the calibrated response functions.
The result of the comparison is discussed in Chapter VII.

In this Monte Carlo calculation, the incident neutron
is traced as follows.

1. The direction and energy of the neutron are chosen
as well as the position it enters the detector.

2. From total cross sections of neutron-proton (n-p)
and neutron-carbon (n-C) collisions determine the mean free
path of the neutron and the distance between the place it
entered and the place where scattering occurs.

3. Decide whether the scattering is inside the
detector or outside. If it is outside the detector, then we
go back to step 1 and pick a new neutron.

4. If the scattering is inside the detector, then
decide if the scattering is n-p or n-C.

5. If it is a n-p scattering, then determine the
energy of the proton and the neutron. The scattered neutron
with new energy will be traced from step 2.

6. If it is a n-C reaction then determine if it is an elastic or inelastic scattering. The inelastic scatterings considered in this calculation are:

a. $n + C \rightarrow n + C^* \rightarrow n + C + \gamma$

b. $n + C \rightarrow \alpha + Be$

c. $n + C \rightarrow n + 3\alpha$

d. $n + C \rightarrow p + B$
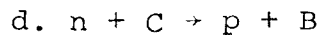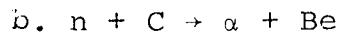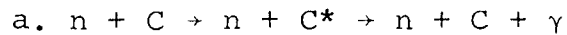
7. The information on the angular distribution of produced particles is supplied so that the energies and the angles of the emitted particles in the laboratory frame may be determined. If there is an emitted neutron, then this neutron will be traced from step 2.

8. It is assumed that a charged particle loses all its energy in the detector. The energy loss is converted to light output and then to the pulse height. The light output in each reaction is added to the previous total for its history.

9. Also, the resolution at each pulse height channel may be simulated so the finite resolution effect is included (Appendix B1).

The proton spectrum from this calculation is the proton response function needed to get the neutron spectral information.

CHAPTER VII

CALIBRATION OF THE NEUTRON DETECTORS

The calibration of the neutron detectors was done at
the University of New Hampshire (UNH) Van der Graaf accelerator
and at the Michigan State University (MSU) cyclotron. At UNH,
two neutron reactions were used: (D,D) and (D,T). In the
(D,D) reaction, $D + D \rightarrow He^3 + n$, Q = 3.266 Mev, the energies
of the neutrons are dependent on the energy of the incident
deuterons and the angle at which the neutrons are emitted.
We placed the detectors at a position perpendicular to the
deuteron beam. For deuterons of 300 kev, the energy of the
neutron beam was 2.52 Mev. In the (D,T) reaction, $D + T \rightarrow$
$He^4 + n$, Q = 17.586 Mev, the energy of the neutron beam was
14.17 Mev at $90°$ for deuterons of 300 kev.

In the MSU calibrations the neutron beam was produced
in the reaction $Be^9 (He^3, n)C^{11}$. The He^3 beam was accelerated
to 70 Mev by isochronous cyclotron. Since the Q value of
this reaction is 7.56 Mev, the neutron spectrum from the Be^9
target was a continuous spectrum with the highest energy
around 77 Mev and a broad maximum around 20 Mev.

We selected the neutron energy by the time of flight
(TOF) technique. Before each run, the time of flight PHA of
the MSU facility (MSU-TOF-PHA) was calibrated. In this cali-
bration neutrons and gamma rays were registered by their
arrival times so that a time of flight spectrum was obtained.

In this spectrum each neutron burst was preceded by a sharp peak which was identified as the gamma ray burst emitted at the instant when the He^3 nuclei hit the Be^9 target. To avoid the overlap of the fast neutrons with the slow neutrons of the previous burst, only one out of four bursts of He^3 was directed into the Be^9 target. For some runs the radio frequency of the cyclotron was 14.343 MHz so the time between two He^3 bursts was 278.9 nanoseconds. Consequently, the time between two gamma ray peaks should also be 278.9 nanoseconds. The MSU-TOF-PHA used was linear and there were 680 channels between two gamma ray peaks so each channel of the MSU-TOF-PHA was 0.41 nanoseconds. The first gamma ray peak was at channel 863. The distance between Be^9 target and the detector was 576.5 cm, so channel 863 corresponded to the time 19.29 nanoseconds. The arrival time of neutrons which were preceded by the first gamma ray peak was $T(I) = 19.29 + 0.41 \times (863 - I)$ nanoseconds, where I is the MSU-TOF-PHA channel number and $T(I)$ is the arrival time of the event registered in channel I. The energy of the neutron corresponding to channel I was

$$E(I) = M_n c^2 \left\{ \frac{1}{\sqrt{1 - [\frac{19.29}{T(I)}]}} - 1 \right\} \text{ Mev, where } M_n c^2 \text{ is the rest}$$

mass energy of the neutron. During each run a single channel analyzer (SCA) was used to select a certain portion of the TOF spectrum. This SCA gated the detector's two dimensional PHA, so the detector analyzed a "monoenergetic" neutron beam.

For the 5 inch detector, the angle between the neutron beam and the detector was 0°. The distance was 576.5 cm from

the Be^9 target. The detector was uniformly illuminated in the direction perpendicular to the cylindrical axis. The signals were both pulse shape and pulse height analyzed so electrons, protons, and alpha particles were identified. Also, all events were printed on two dimensional matrices so both energy and particle type were known. From these matrices we extracted proton spectra. The proton spectrum for each run was used as our response function.

For the 2 inch detector, the angle between the neutron beam and the detector was also 0°. The distance from the target was 405.1 cm. The detector was placed so that the neutron beam was again perpendicular to the axis of the detector. For one run we rotated the detector such that the axis of the detector was along the direction of the neutron beam. In another run we rotated the detector so the angle was 45°. The purpose of these changes was to check if the response of the detector was isotropic. Also, in another run we disabled the charged particle shield to see if this caused any effect.

We draw the following conclusions from these calibrations:

(1) The relation between proton energy and the flight PHA channel number can be described as,

for the 5 inch detector:

$$E_p(I) = 4.42 + 0.63I + 3.8 \times 10^{-3}I^2 - 6.9 \times 10^{-5}I^3 +$$
$$+ 1.3 \times 10^{-6}I^4 \quad \text{Mev} \qquad \text{(Fig. 7-1)}$$

for the 2 inch detector:

$$E_p(J) = 1.65 + 0.115J + 1.18 \times 10^{-3}J^2 - 1.94 \times 10^{-5}J^3 +$$

$$+ 1.3 \times 10^{-7}J^4 \quad \text{Mev} \qquad \text{(Fig. 7-2)}$$

where, I and J refer to the pulse-height PHA channel numbers of the 5 inch and the 2 inch detectors respectively.

(2) The detectors are isotropic with respect to the incident neutron directions.

In Fig. 7-10, the three response functions correspond to the neutrons with energies about 23.6 Mev incident at different incident angles. Three response functions are almost identical so the detector is isotropic with respect to the incident neutron directions. For Run 34, neutrons with incident angle 45° and mean energy 23.6 Mev, and Run 35, neutrons with incident angle 90° and mean energy 23.55 Mev, we calculated the average number of protons per channel per microcoulomb He^3 nuclei at about $E_p=11$ Mev of these two response functions. For Run 34 and Run 35 we found that there were 4.08 and 4.09 protons/channel/microcoulomb respectively. This indicates that the effeciency of the 2 inch detector is not dependent on the incident angle of the neutron.

(3) The charged particle shields do not change the shape of the recoil proton spectrum in the NE213 scintillators.

In Fig. 7-6, it shows two calibrations of the 5 inch detector with and without the ACD connected at the mean energy 70.6 Mev. The total charge of the incident He^3 nuclei was 55.38 microcoulombs for Run 11 and 55.41 microcoulombs for Run 12, therefore, same total number of incident neutrons.

From Fig. 7-6, within the statistical accuracy of the observed
counting rates, it indicates that the ACD neither changes
the efficiency of the detector nor distorts the recoil proton
spectrum.

(4) The phase space distribution which is assumed in the
theoretical calculations of Kurz, (1964) and Stanton, (1971)
is not appropriate to describe the energy distribution of
the protons from the reaction $C^{12}(n,p)B^{12}$.

The calibrated response functions from the MSU
calibrations are shown in Fig. 7-3 to Fig. 7-12. In these
figures every spectrum is corresponding to 10,000 incident
neutrons unless 'arbitrary scale' is indicated. From the
response functions of the 5 inch detector we clearly see the
structures in the proton spectra (Fig. 7-4, Fig. 7-5).
There is a plateau at the higher energy side, which extends
to the proton energy corresponding to the incident neutron
energy. Since only in the n-p scattering can a proton
absorb all neutron energy, we can identify this portion of the
recoil proton spectrum as due to the protons from the n-p
scattering. The n-p scattering has been well studied and
both the cross section and the proton energy distribution are
known, so we have normalized the height of the plateau of
each response function such that the proton spectrum is
corresponding to the response function for 10,000 incident
neutrons. This normalization factor was calculated in the
following way. For a NE213 detector with length d, the

36

efficiency of the n-p scattering is

$$A = \frac{n_{H}\sigma_{H}(E_{n})}{n_{H}\sigma_{H}(E_{n}) + n_{C}\sigma_{C}(E_{n})} \{1 - \exp[-n_{H}\sigma_{H}(E_{n})d - n_{C}\sigma_{C}(E_{n})d]\} \quad (7-1)$$

where, n_{H} : the density of hydrogen of NE213

n_{C} : the density of carbon of NE213

$\sigma_{C}(E_{n})$: the total cross section of n-C scattering

$\sigma_{H}(E_{n})$: the total cross section of n-p scattering

$$= 3\pi[1.206E_{n} + (-1.86 + 0.09415E_{n} + 0.0001306E_{n}^{2})^{2}]^{-1} +$$

$$+ [1.206E_{n} + (0.4223 + 0.13E_{n})^{2}]^{-1} \text{ barns}$$

E_{n} : the energy of the incident neutron (Mev) in

the laboratory (Lab) system

(Marion et al. 1963)

The probability for a proton to have energy between E_{n} and

$E_{n}-1$ is

$$B = \frac{(\cos\theta + 1) + \frac{b}{3}(\cos^{3}\theta + 1)}{2 + \frac{2}{3}b}$$

where, $b = 2(\frac{E_{n}}{90})^{2}$

$\theta = 2 \sin^{-1} \sqrt{(E_{n}-1)/E_{n}}$ (Appendix A)

so, the normalization factor is A x B x 10,000.

Normalizing the response function by this method
implicitly assumes that the resolution of the detector is
perfect. This assumption will introduce errors in the
absolute intensity of the response function. The error
depends on the energy of incident neutrons and the resolution
of the detector. To estimate the error we choose the highest
energy response function in our calibrations. Since the
anisotropy of the proton distribution in the n-p scattering

is the greatest for the highest energy response function, we can estimate the largest error in our normalization process. The procedure to estimate the error is as follows.

1. From the spectrum of the incident neutrons with energies from 71.6 Mev to 78 Mev (Run 10) we calculate the proton recoil spectrum from n-p scattering. The number of the recoil protons per Mev is on an arbitrary scale and the resolution of the detector is assumed to be perfect (Fig. 7-16a).

2. We use the Monte Carlo method to simulate the resolution of the detector (Appendix B1). We keep changing the resolution parameter L_0 until the proton recoil spectrum with the specified finite resolution effect matches the observed response function of 74.3 Mev (Run 10) in the energy region above 70 Mev (Fig. 7-16b, Fig. 7-5).

3. For neutrons with energy 74.3 Mev we then calculate the proton recoil spectrum from n-p scattering (Fig. 7-17a) and use the Monte Carlo method to simulate the resolution effect of the detector with the resolution parameter obtained in step 2.

4. From comparing the intensity at 74.3 Mev in the proton recoil spectrum with perfect resolution (Fig. 7-17a) and the intensity of the plateau in the proton recoil spectrum with the finite resolution (Fig. 7-17b) we are able to estimate the percentage error.

For Run 10 with E_n=74.3 Mev the error introduced by the normalization method we used is 20%. In this estimation we have not considered the multiple scattering effect. For

a neutron elastically scatters with carbon it loses small amount of energy; if it then scatters with proton we tend to have more recoil protons than we estimated by considering only single n-p scattering. For neutron with energy 74.3 Mev, we estimate the latter effect in the following way. Since in a n-C elastic scattering the neutron loses small amount of energy, we assume that the neutron has same energy before and after the n-C scattering. The probability for a neutron to have an elastic n-C scattering followed by a n-p elastic scattering is $[1-e^{-n_H \sigma_H (E_n) d - n_C \sigma_C (E_n) d}]$

$$\frac{n_C \sigma_{Ce} (E_n)}{n_H \sigma_H (E_n) + n_C \sigma_C (E_n)} \; [1-e^{-n_H \sigma_H (E_n) \ell - n_C \sigma_C (E_n) \ell}] \; \frac{n_H \sigma_H (E_n)}{n_H \sigma_H (E_n) + n_C \sigma_C (E_n)}$$

where, ℓ is the effective length of the detector with respect to the scattered neutron after the n-C elastic scattering, and $\sigma_{Ce} (E_n)$ is the cross section of n-C elastic scattering. For a neutron with energy 74.3 Mev the mean free path of a n-C elastic scattering is in the order of 40 cm which is larger than the length of the detector so the average distance where a n-C elastic scattering occurs is d/2. Hence, ℓ is taken to be d-d/2=d/2. Taking cross section data from Kurz, (1964) the probability of a n-C elastic scattering follower by a n-p scattering is 6% of that of a single n-p scattering. If we considered this effect then the normalization method just described overestimates the effeciency by 13% at E_n=74.3 Mev, and 4% at E_n=40 Mev. At E_n=25 Mev this method under-estimates the efficiency by 3%. In the neutron spectrum unfolding process we corrected this effect on all normalized

response functions used in the least squares test.

There is also a Gaussian bump in every response function for incident neutron energies above 27.9 Mev. We attribute this to the protons from the reaction $C^{12}(n,p)B^{12}$ for two reasons. First, it is the most prolific reaction yielding protons in this energy range. Second, the energy range covered by the Gaussian bump of the proton spectrum is close to the energy range of the proton, calculated from kinematic relations, in this reaction. To estimate the cross section of the reaction $C^{12}(n,p)B^{12}$ we first subtracted the protons due to n-p scattering from the proton spectrum and calculated the number of protons under the Gaussian bump. The calculated proton recoil spectrum from n-p scattering was obtained in the following way.

The differential cross section $\dfrac{d\sigma_H(\theta_c, E_n)}{d\Omega_c}$ in the center of mass (CM) system is

$$\frac{d\sigma_H(\theta_c, E_n)}{d\Omega_c} = \frac{\sigma_H(E_n)}{4\pi} \left[\frac{1 + b\,\cos^2\theta_c}{1 + \frac{b}{3}}\right] \text{ barns/ster.} \qquad (7\text{-}2)$$

(Marion et al. 1963)

where, θ_c : the neutron scattering angle in the CM system

Ω_c : the solid angle in the CM system.

In the n-p scattering, the probability for the neutron to be scattered into $d\Omega_c$ is P = Eqn. (7-1) x Eqn. (7-2) x $\dfrac{d\Omega_c}{\sigma_H(E_n)}$

This is also the probability for the recoil proton to be in the energy range $d(E_n \sin^2\theta_1)$, where θ_1 is the scattering

angle of the neutron in the Lab system. If there are N_n incident neutrons, the number of protons per unit energy is

N_n x P / d($E_n \sin^2\theta_1$). By the relation $\theta_c = 2\theta_1$, the number of protons per unit energy turns out to be

$$\{1 - \exp[-n_H \sigma_H(E_n)d - n_C \sigma_C(E_n)d]\} \frac{n_H \sigma_H(E_n)}{n_H \sigma_H(E_n) + n_C \sigma_C(E_n)} \cdot$$

$\cdot \frac{1}{E_n} \left(\frac{1+b \cos^2\theta_c}{1 + \frac{b}{3}} \right) N_n$. In this expression we can write $\cos\theta_c$

as $\cos\theta_c = 1 - 2\frac{E_p}{E_n}$, where E_p is the energy of the recoil proton.

We calculated the proton recoil spectrum from the n-p scattering for 10,000 incident neutrons and obtained the value of protons/Mev at each pulse height channel. For each pulse height channel we then subtracted the value of protons/Mev in the proton spectrum of the n-p scattering from the response function, and obtained a proton energy spectrum due to reactions other than the n-p scattering. Assuming that the protons from the reaction $C^{12}(n,p)B^{12}$ were under the Gaussian bump, we located the center energy of the Gaussian peak in the resulting proton spectrum and then counted the number of protons from the center energy to the high energy side. The total number of protons under this Gaussian peak is then twice this number. After we obtained the total number of protons under the Gaussian peak, we calculated the total number of protons in the proton recoil spectrum from the n-p scattering. The ratio of the number of protons under the Gaussian bump to the protons from the n-p scattering is $n_C \sigma_{pB}/n_H \sigma_H$, where σ_{pB} is the cross section of the reaction

$C^{12}(n,p)B^{12}$. The resulting cross sections of the reaction

$C^{12}(n,p)B^{12}$ as a function of neutron energy are shown in

Fig. 7-13. We show the center energy of the Gaussian peak

versus the energy of incident neutrons in Fig. 7-14. In

Fig. 7-15, the energy difference between the Gaussian peak

and the energy of the incident neutrons is plotted as a

function of neutron energy. We called this energy difference

the 'Q' value.

A comparison between calibration and the Monte Carlo

calculation following the method of Stanton (1971) is shown

in Fig. 7-7. In this calculation perfect resolution was

assumed and E_n=70 Mev. The corresponding calibrated response

function was made at the mean neutron energy of 70.6 Mev.

The calculated and measured response functions do not agree.

The disagreement does not imply that the Monte Carlo calcula-

tion is not a resonable way to handle the problem of interac-

tions of neutrons in a detector. In order to predict the

proton spectrum both cross sections and the energy distribu-

tions of charged particles emitted from n-C inelastic scat-

terings have to be known. Unfortunately, the cross sections

for inelastic scattering of neutrons on carbon are not well

known for neutron energies higher than 20 Mev. Furthermore,

from our calibrations we are convinced that the energy distri-

bution of protons from the reaction $C^{12}(n,p)B^{12}$ can not be

described by the phase space distribution (Kurz, 1964; Stanton,

1971). In the phase space distribution the number of protons

with energy T in the CM system is N(S) dS $\propto \sqrt{S}$ (1-S)^2 dS, where, S is the ratio of T to the maximum energy of the proton in the CM system. The distribution of protons in the phase space distribution is thus similar to an evaporation spectrum. For E_n=70 Mev, according to this phase space distribution, most protons from the reaction $C^{12}(n,p)B^{12}$ have energies less than 20 Mev, and the most probable energy is around 10 Mev. If the threshold energy of the neutron detector is not zero, then the assumption of the phase space distribution tends to assign more protons from this reaction below the threshold energy. Consequently, the efficiency of the neutron detector is underestimated.

The details for the response functions of the MSU calibrations are in the following page.

Detector type	Run#	$\overline{E}_n$ Mev	$E_{n\ min}$ Mev	$E_{n\ max}$ Mev	ACD[*]	Angle[**] degree	Fig.
5"	22	4.9	4.84	4.96	yes	90	7-3
5"	21	9.96	9.82	10.1	yes	90	7-3
5"	20	14.5	14.5	14.6	yes	90	7-4
5"	19	19.9	19.6	20.2	yes	90	7-4
5"	18	27.7	25.3	34	yes	90	7-4
5"	17	39.4	35.3	45	yes	90	7-4
5"	14	48.5	46.1	51.7	yes	90	7-5
5"	13	60.7	57.6	64.6	yes	90	7-5
5"	12	70.6	66.8	75.6	no	90	7-5,7-6,7-7
5"	11	70.6	66.8	75.6	yes	90	7-5,7-6
5"	10	74.3	71.6	78	yes	90	7-5
2"	27	2.89	2.86	2.92	yes	90	7-8
2"	26	4.85	4.8	4.9	yes	90	7-8
2"	25	9.55	9.5	9.6	yes	90	7-8
2"	23	12.78	11.8	13.8	yes	90	7-9
2"	24	14.7	14.4	14.9	yes	90	7-9
2"	32	23.4	22.8	24	yes	0	7-10
2"	34	23.6	22.8	24.4	yes	45	7-10
2"	35	23.55	23.1	24	yes	90	7-10
2"	28	27.4	27	27.8	yes	90	7-11
2"	29	46	44.7	47.4	yes	90	7-12
2"	30	64.12	62.7	65.7	yes	90	7-12

* charged particle shield connected or not

** angle between neutron beam and the axis of the detector being calibrated

CHAPTER VIII

BALLOON FLIGHT

The experiment was conducted on June 22, 1973 at the National Scientific Balloon Facility, Palestine, Texas $(\lambda=42^{\circ}N)$. The balloon was launched at 05:33:04 UT and cut down at 16:47:43 UT. The balloon system ascended at an average rate of 3.61 meters per second to a float altitude $4.2 \ g/cm^2 - 2.9 \ g/cm^2$ and was allowed to float at altitude for 8.5 hours.

From 05:33 to 11:22 UT the 2 inch detector was moved to be below the 5 inch detector and the central line of the two detectors was 32° from the zenith. The distance between the two detectors was 50 cm. In order to make the central line of the detectors point toward zenith the gondola was rotated 32° from the zenith. In this mode, the time of flight (TOF) system measured upward moving particles.

From 11:32 to 12:36 UT two detectors were moved to be side by side. The distance between them was 28 cm. The gondola was then oriented along the zenith, so horizontally moving particles were measured by the TOF system.

From 12:49 to 15:11 UT the 5 inch detector was moved to be below the 2 inch detector and again the gondola was tilted 32° from the zenith. The distance between two detectors was 50 cm. This period was used to measure the downward moving particles.

From 15:25 to 16:47 UT the detectors were moved side

by side again.

During the entire experiment, not only the directional fluxes of neutrons and gamma rays were measured by the TOF system, but also omnidirectional fluxes were measured in each detector separately.

Each event was transmitted to a ground receiving station where it was recorded on a seven track video tape recorder operating at 30 inches per second. Every event consisted of a 47 bit data word and contained the following information:

Bit	Information
1-6	110011 to identify the beginning of data string
7	TOF identification (ID)
8	5 inch detector (ID)
9-15	5 inch detector pulse-shape PHA channel number
16-22	5 inch detector pulse-height PHA channel number
23	time bit
24	2 inch detector (ID)
25-31	2 inch detector pulse-shape PHA channel number
32-38	2 inch detector pulse-height PHA channel number
39	time bit
40-45	TOF PHA channel number
46	parity bit
47	time bit

Three time bits served to identify the separation of the data group.

After the flight the video tapes were returned to UNH where they were played back into an F.M. subcarrier discriminator and a ground station. The ground station checked the string of data word to verify that the identification and parity bit were correct. Those correct events were then transferred onto the digital tapes by an incremental recorder and the tapes then processed by an IBM 360 computer. The resulting true events were printed onto a two dimensional matrix for each tape.

CHAPTER IX

ANALYSIS OF FLIGHT DATA

For this balloon flight 12 video data tapes were
obtained at float altitudes and were analyzed. Data on the
omnidirectional and directional detectors were retrieved
from the tapes but only data from two operating independently
omnidirectional detectors are presented here.

The house keeping data obtained at float altitudes
have been checked. There is no significant fluctuations.
This indicates that the system was very stable during the
flight. Before and after the flight, we checked the gains
of the pulse height (PH) PHAs with the various gamma ray and
neutron radioactive isotope sources, the IFCs and the maximum
energy deposited peak of the minimum ionizing sea level muons.
During the flight we checked the gains of the system with the
IFCs, and found no gain shifts in the PH-PHAs.

From each data tape we retrieved four flight matrices;
two matrices for each detector. For the 5 inch detector,
the two matrices were: 1) neutral particle, obtained when
the detector was in the anti-coincidence mode with the ACD;
2) charged particle, obtained when the detector was in the
coincidence mode with the ACD. For the 2 inch detector,
there were also both a neutral and a charged particle matrices.
In Fig. 5-2, we show an example of three dimensional plot of
a neutral particle matrix of the 2 inch detector. As already

described in section 5.2, from each neutral particle matrix
it was possible to extract 4 particle bands, corresponding
to electrons, protons, alpha particles, and the IFC. Due to
the finite resolution effect of the pulse shape (PS) PHA,
there was a spread in the PS channels for each PH channel, so
for each band at each PH channel we added all counts in the
PS channels which corresponded to this particular PH channel.
In this way, a 128-channel PH distribution was obtained for
each band. From the IFC we could make the necessary dead
time corrections. From each flight matrix we calculated the
total number of IFC counts, then the counting rate of the IFC
was calculated by dividing the total IFC counts by the flight
time of this matrix. The counting rate of the IFC of the 5
inch detector is 3.96 counts/sec so the dead time correction
was (3.96 counts/sec)/(the IFC counts/sec of a matrix).
For the 2 inch detector, the counting rate of the IFC without
dead time is 1.55 counts/sec, and the same method of the dead
time correction was applied to its flight matrices. The IFC
band was also used to monitor the stability of the PHAs.
During the flight the IFC light pulses stayed at the same
channels of the PH-PHAs, hence, it was not necessary to make
any correction in the energy assignment to the channels of
the PH-PHAs. For the 2 inch detector, at float altitudes,
the gain of the PS-PHA drifted about 10 channels toward the
lower PS channels. The shift was about one channel per
matrix, but this caused no problem in the separation of the
particle bands, therefore, no correction was necessary .

After the dead time correction had been made for each band we
added all 128-channel PH distributions of flight matrices
together. The PH distribution of the proton band obtained
in this way is the proton recoil spectrum in protons/channel
versus PH channel number. From proton energy calibrations
we had the relationship between proton energies and channel
numbers of the PH-PHAs. Dividing the number of protons of
each PH channel by its channel width, we derived a proton
recoil spectrum in protons/Mev versus proton energy. The
proton spectrum in protons/Mev versus proton energies of
the 5 inch detector is shown in Fig. 9-1. The proton recoil
spectrum of the 2 inch detector in protons/Mev versus proton
energies is shown in Fig. 9-2.

To unfold the proton recoil spectra we used the first
method in Chapter VI, section 6.1. In the MSU calibrations
we could not calibrate the detectors in energy steps of 1 Mev
or less, because there was not enough time, so an interpola-
tion and extrapolation method was used to construct the set
of response functions needed to unfold the neutron spectrum.
For example, to construct the response function at 66 Mev
from calibrated response functions at 60.7 Mev (Run 13) and
70.6 Mev (Run 12) of the 5 inch detector (Fig. 7-5), we
followed an interpolation method:

1. Determine the value of protons/Mev of the plateau
at 66 Mev: Since this plateau is due to the n-p scattering
(Chapter VII) we calculated the value of protons/Mev at 66
Mev by the same method as we did for the normalization of the

response function in Chapter VII.

2. Determine the energy at the intersection of the Gaussian bump and the plateau: In the response function of 60.7 Mev the energy difference between the mean energy of the incident neutrons and the base of the Gaussian bump is 13 Mev; it is also 13 Mev for the response function of 70.6 Mev. The average is still 13 Mev, so the energy at the intersection of the Gaussian bump and the plateau was taken to be 53 Mev for the response function of 66 Mev.

3. Determine the slope of proton energy versus protons/Mev between the base of the Gaussian bump and the plateau at 66 Mev: The slope in the response function at 60.7 Mev is 0.2, and it is 0 for the response function at 70.6 Mev, hence, the slope in the response function at 66 Mev was taken to be 0.1.

4. Determine the value of protons/Mev at 53 Mev of the response function of 66 Mev: We drew a line with slope 0.1 from the plateau at 66 Mev to 53 Mev. The value of protons/Mev at 53 Mev was automatically determined when this line reached 53 Mev.

5. Determine the energy of the Gaussian peak: The energy of the Gaussian peak at the response function of 60.7 Mev is 35 Mev, and at the response function of 70.6 Mev is 43.5 Mev, therefore, we took the average value 39.3 Mev as the energy of the Gaussian peak of the response function of 66 Mev.

6. Determine the value of protons/Mev at the Gaussian

peak of the response function of 66 Mev: The values of protons
/Mev at the Gaussian peaks are 27.3 and 23.8 for the response
functions of 60.7 Mev and 70.6 Mev respectively. So, for
the response function of 66 Mev, the average value 25.6 was
taken to be the value of protons/Mev of the Gaussian peak.

7. Determine the energy at the intersection of the
Gaussian bump and the broad bump at low energy side of the
response function at 66 Mev: For the response function of
60.7 Mev the energy at the intersection is 28 Mev; for the
response function of 70.6 Mev it is 35 Mev, so the average
value 32 Mev was assumed to be the energy at the intersection
for the response function of 66 Mev.

8. Determine the value of protons/Mev at 32 Mev of
the response function of 66 Mev: The value of protons/Mev
at 28 Mev of the response function of 60.7 Mev is 23.3, and
at 35 Mev of the response function of 70.6 Mev is 19.4, so
for the response function of 66 Mev the average value 21.4
protons/Mev was assumed to be the value at 32 Mev.

9. Determine the center of the broad bump at low
energy side of the response function of 66 Mev: The energy
at the center of the broad bump was estimated to be 14 Mev
for the response function of 60.7 Mev; 18 Mev for the response
function of 70.6 Mev. For the response function of 66 Mev
we took the average value 16 Mev as the center of the broad
bump.

10. Determine the value of protons/Mev at the center
of the broad bump: The value of protons/Mev at 14 Mev of the

response function of 70.6 Mev is 35, and at 18 Mev of the response function of 70.6 Mev is 30. The average value 32.5 protons/Mev was taken to be the value of protons/Mev at 16 Mev of the response function of 66 Mev.

11. Determine the slope of proton energy versus protons/Mev between the center of the broad bump at low energy side and the intersection of this broad bump and the Gaussian bump in the response function of 66 Mev: The slopes in this region are -0.8 and -0.6 for the response functions of 60.7 Mev and 70.6 Mev respectively, so the average value -0.7 was taken to be the slope in this region for the response function of 66 Mev.

12. Determine the slope of proton energy versus protons/Mev between the center of the broad bump at low energy side and the lowest few channels: The slope in this region is 0 for the response function of 60.7 Mev; 0.5 for the response function of 70.6 Mev. We took 0.25 as the slope in this region for the response function of 66 Mev.

To construct the response functions by the extrapolation method we followed the tendency of the systematic changes of the response functions and found the relations between the stuctures on the response functions. For example, to construct the response functions for energies higher than 74.3 Mev for the 5 inch detector we followed these procedures.

1. We divided a response function into three major regions: (1) the plateau at the high energy side, (2) the Gaussian bump, and (3) the broad bump at the lower energy

side of the response function (Fig. 7-5).

2. The ratios of the intensities of (1) the Gaussian bump, (2) the broad bump, and (3) the base between the Gaussian bump and the broad bump to the plateau were found from calibrated response functions from 48.5 Mev to 74.3 Mev (Fig. 9-3).

3. From Fig. 7-14 and Fig. 7-15, the position of the Gaussian bump was found to be 23 Mev less than the energy of incident neutrons for the response functions above 60.7 Mev.

4. The shape of the Gaussian bump was preserved in the extrapolated response functions, because we noticed that the Gaussian bump had similar standard deviation.

5. Determine the central energy of the broad bump at lower energy side of the response function: From response functions of 60.7 Mev, 70.6 Mev and 74.3 Mev (Fig. 7-5), we determined the relation between the central energy of the broad bump and the energy of incident neutrons (Fig. 9-4). This broad bump, from its systematic changes, tends to become flat as energies of incident neutrons increase so that the determination of the central energy of the broad bump is not critical.

In Fig. 9-5, we show examples of the interpolated response functions of 66 Mev and 69 Mev as well as the extrapolated response functions of 77 Mev and 80 Mev along with the calibrated response functions of 70.6 Mev and 74.3 Mev.

54

For the 2 inch detector, the response functions were constructed as follows.

1. Response functions of neutrons with energies less than 10 Mev: Below 10 Mev the only dominate reaction in the detector is the n-p scattering. For neutrons with energies less than 9.55 Mev the calibrated response functions show typical proton recoil spectra from n-p scattering (Fig. 7-8), so that the calculated proton recoil spectra of n-p scatterings were used as the response functions.

2. In the neutron energy range 10 Mev to 27.4 Mev we used the interpolation method to construct response functions. The principle of interpolation has been described in detail in the construction of the response function for 66 Mev neutrons on the 5 inch detector. To interpolate the response functions of the 2 inch detector in this energy range the procedure is simpler because the structures are not that complicated. The spike at lower energies is attributed to the contamination by alpha particles because this spike begins for the response function at E_n=9.55 Mev. Since the threshold energy of the reaction $C^{12}(n,\alpha)Be^9$ is 6.2 Mev and the threshold energy of the reaction $C^{12}(n,n3\alpha)$ is 7.9 Mev, alpha particles are produced for neutrons with energies exceeding 6.2 Mev. The pulse shape resolution is poor for small light pulses (Fig. 5-2, 5-3, 5-4, 5-5), so it is probable that some alpha particles are mixed with protons in the first few channels. In the construction of response functions we included this spike (Fig. 9-6), because in the

flight data there is same kind of alpha contamination in the first few channels.

3. Construct the response functions between 27.4 Mev and 46 Mev: To interpolate the response functions in this energy region, it was necessary to know the absolute magnitude of the protons/Mev in the response function for 46 Mev; we normalized the response function of 46 Mev with following method.

As the energy of neutrons increases the average energy of alpha particles produced from n-C inelastic scatterings increases, consequently, the total light output from alpha particle is larger. When the light output is larger, the pulse shape resolution improves (Fig. 5-2, Fig. 5-3, Fig. 5-4, Fig. 5-5) so that the structures at lower channels in the proton spectrum tend to diminish (Fig. 7-12). But the contribution of protons from the reaction $C^{12}(n,p)B^{12}$ remains because our detectors are not sensitive enough to distinguish all protons of the reaction $C^{12}(n,p)B^{12}$ completely from protons of n-p scatterings (Fig. 5-4). The effect of the reaction $C^{12}(n,p)B^{12}$ has been observed by Riddle et al. (1974). In their experiment a 7 inch diameter by 3 inch thick plastic detector NE102 was used. Although the pulse shape discrimination technique was not incorporated in their system a very broad bump from $C^{12}(n,p)$ B^{12} was observed. A factor of two is estimated for the ratio of the intensity of the broad bump to the plateau in their pulse height spectrum at a neutron energy of 45 Mev. Despite of the difference in

sizes of detectors this is consistent with our observation

(Fig. 7-5, Run 14). The agreement is expected because of

the similar composition of NE213 and NE102. For 10,000

incident neutrons with an energy of 46 Mev we calculated the

proton recoil spectrum of n-p scatterings and determined the

height of the plateau at 46 Mev. From our calibrated response

function of the 5 inch detector at 48.5 Mev and the result

of Riddle et al. (1974) we learned that the intensity of

proton spectrum in the region 20 Mev to 25 Mev is twice the

intensity of the proton recoil spectrum from n-p scatterings

near the proton energy equal to the energy of the incident

neutrons. Hence, we normalized the average value of protons

/Mev in the region 20 Mev to 25 Mev for the response function

of the 2 inch detector at 46 Mev to be twice that of the

intensity of the plateau at $E_p = 46$ Mev.

4.   The response functions in the energy range 46

Mev to 100 Mev: In this energy range we assumed that the

proton energy distribution in a response function of the 2

inch detector was the same as that for the 5 inch detector

but the magnitude of protons/Mev was reduced by a factor K,

where K is the ratio of the efficiency of the 2 inch detector

to the efficiency of the 5 inch detector. Because both the

2 inch detector and the 5 inch detector are made of NE213;

incident neutrons should interact by the same reactions in

the detectors. Since we observed that our 5 inch detector

has a similar response function to the 7 inch diameter by 3

inch thick NE102 detector of Riddle et al. (1974) at a

neutron energy of about 45 Mev. It is reasonable to expect that the response functions of the 2 inch detector and the 5 inch detector at higher neutron energies have similar relative intensities between the plateau and the structures.

Since the threshold of the 5 inch detector is 4.41 Mev and the threshold energy of the 2 inch detector is 1.65 Mev, we assumed that the intensity at 1.65 Mev was zero and interpolated the intensity between 4.41 Mev and 1.65 Mev. This does not introduce large errors because the number of protons produced by the neutrons with energies in the region around 4.41 Mev greatly exceeds the number of protons produced by neutrons with energies between 46 Mev and 100 Mev.

To construct a set of response functions required for unfolding the neutron spectrum we used the interpolation and extrapolation method just described to get a complete set of response functions from 2 Mev to 100 Mev for the 2 inch detector, and from 5 Mev to 136 Mev for the 5 inch detector. Also, for the 5 inch detector, from 136 Mev to 300 Mev at steps of 5 Mev, we calculated the theoretical proton recoil spectrum of n-p scattering for 10,000 neutrons, and assumed that it represented the response function. The method used to calculate this proton recoil spectrum from n-p scattering has been discussed in Chapter VII, and we will discuss the justification for this assumption.

The proton energy range covered by the 2 inch detector was 1.61 Mev to 29.4 Mev, and by the 5 inch detector was 4.41 Mev to 75 Mev. Due to the poor pulse shape resolution

of the 2 inch detector below 2 Mev, and the 5 inch detector

below 7 Mev and above 75 Mev, in order to have data without

the contamination by the recoil electrons we excluded the

data in these energy ranges. Because of the better resolu-

tion of the 2 inch detector we tried to extract the maximum

information from it. But due to the efficiency of the

detector, the statistics at energies greater than 20 Mev were

poor. Hence, it was decided to deduce from it the neutron

energy spectrum only in the energy range 2 Mev to 20 Mev.

To do so, it was necessary to have the information on the

neutron energy spectrum above 20 Mev. Since the 5 inch

detector covered the energy range from 4 Mev to 75 Mev, the

neutron spectrum in this region might be deduced if the

spectrum above 75 Mev was known. Since high energy neutrons

are produced primarily by the knock-on collisions of primary

cosmic rays with the constituents of atmosphere, it is rea-

sonable to expect that the resulting neutron spectrum is

closely related to the spectrum of the primary cosmic rays.

The measurements of Kanbach et al. (1974) indicate that the

neutron spectrum above 100 Mev can be described by a power

law in energy with index of -1.89. For these reasons we

assumed that beyond 100 Mev the neutron energy spectrum was

a power law with index of -2. We assumed that the neutron

spectrum at lower energies was a smooth power law in energy

but that the index was a function of energy. The total

neutron energy spectrum in the range below 100 Mev was divided

into several segments. In the i_{th} segment, the differential

energy spectrum was $dN/dE = A_i E^{-\gamma i}$, where A_i is the coefficient

of the i_{th} segment, γi is the index of the power law of the

same segment. The relation between two adjacent segments is

$A_i E_{i+1}^{-\gamma i} = A_{i+1} E_{i+1}^{-\gamma i+1}$, where, E_{i+1} is the beginning energy of

the $i+1_{th}$ segment.

From an assumed incident neutron spectrum we calcu-

lated the relative intensity at each energy corresponding to

each response function. From the relative magnitude of

every response function and the complete set of response func-

tions, the theoretical proton recoil spectrum was determined.

The counts N_j^{cal} at channel j of the theoretical spectrum was

$N_j^{cal} = \sum_i n_{ji} \times (T_{i+1} - T_i)$, where T_i is the energy of the i_{th}

response function and n_{ji} is the protons per Mev of the i_{th}

response function at channel j.

This calculated spectrum was compared with the

flight data by the Chi-square test. We calculated the

reduced Chi-square by

$$\frac{1}{T-I-1} \sum_j \frac{(N_j^{obe} - N_j^{cal})}{N_j^{obe}}$$

where, T: total channels used in the test

   I: total segments of the assumed spectrum

   N_j^{obe}: the observed protons at channel j.

We kept adjusting the intensity and the indices of the

assumed spectrum until we got the best reduced Chi-square value.

If we assumed different segments for the incident

neutron spectrum we could obtain another spectrum which also

gave a good fit to the observed data. By 'good fit' we mean

that when the calculated proton recoil spectrum was plotted
along with the observed proton recoil spectrum it fell within
two standard deviations of the statistical uncertainty in the
range of the observed proton recoil spectrum. From the least
squares fit we found a set of spectra from 20 Mev to 100 Mev
which gave good fits to the observed proton recoil spectrum
of the 5 inch detector. Since we could deduce detailed in-
formation from the 2 inch detector in the energy range 2 Mev
to 20 Mev the spectra derived from the 5 inch detector in the
region 20 Mev to 100 Mev were used as constraints in deducing
the energy spectra in the energy range 2 Mev to 20 Mev from
the 2 inch detector. We took one of the neutron spectra
deduced from the 5 inch detector and fixed the value of the
differential neutron flux at 20 Mev, consequently, fixing both
the energy spectrum shape and differential fluxes in the
energy range 20 Mev to 300 Mev. This neutron spectrum was
used as the constraint in deducing the neutron energy spectrum
in the energy range 2 Mev to 20 Mev from the proton recoil
spectrum of the 2 inch detector. For every neutron spectrum
deduced from the 5 inch detector in the energy range 20 Mev
to 100 Mev we found a corresponding neutron spectrum in the
energy range 2 Mev to 20 Mev from the 2 inch detector.
After we determined the neutron spectra between 2 Mev to 20
Mev we then repeated the procedure, using them as the con-
straints, to refine the spectra in the energy range 20 Mev
to 100 Mev for the 5 inch detector. Due to the statistics
of the observed data, it was theoretically possible to deduce

an infinite set of spectra if we broke the spectrum into

different segments. Every spectrum which gave a good fit

to the observed data should be included. We observed,

however, that all spectra tended to fall within a common

region. This region defines the uncertainty associated

with this technique and, consequently, for our results.

In Fig. 10-1 and Fig. 10-2, we indicate this region by the

error bars associated with the spectrum. The error bars

should not be misunderstood as the uncertainties of the

measurements at the corresponding energies. In Fig. 10-3

we show the observed proton recoil spectrum of the 5 inch

detector along with the calculated proton recoil spectra which

correspond to three different assumed incident neutron spectra.

The one marked 'calculated"best fit"' is the proton recoil

spectrum produced by the neutron fluxes corresponding to

our deduced neutron leakage spectrum shown in Fig. 10-1 and

Fig. 10-2. The one marked 'lower limit' is the proton recoil

spectrum produced by the neutron fluxes corresponding to the

lower limits of the error bars associated with our deduced

neutron leakage spectrum. Also, we show the proton recoil

spectrum produced by the neutron fluxes measured by the

Preszler et al., (1974) for comparison.

In this procedure an assumption was made about

the construction of the response functions of the 5 inch

detector. For neutrons with energies greater than 136 Mev

and less than 300 Mev, we considered only the proton recoil

spectra from n-p scatterings in constructing the response

functions. We had noticed from the measured response functions obtained at the MSU facility that for neutrons with energies greater than 23.4 Mev the reaction $C^{12}(n,p)B^{12}$ began to contribute a broad bump, more or less a Gaussian shape, on top of the proton spectrum and that its center was about 20 Mev below the incident neutron energy. For neutrons with energies greater than 136 Mev this bump would be beyond 75 Mev. And from the systematic changes of the calibrated response functions a tendency was noted that the structures in the proton spectrum diminished with increasing neutron energy except for the Gaussian bump. In the least squares test, the observed proton data and the theoretically calculated proton recoil spectra from the assumed neutron spectra were compared up to 75 Mev only. We found that unless the neutron spectra in the region 100 Mev to 300 Mev were dramatically different from that assumed, the result was not sensitive to the contribution from this energy region. So this assumption would not distort our result.

CHAPTER X

RESULTS OF THE NEUTRON MEASUREMENT

In order to compare our results with other measure-
ments we normalized all results to the minimum in solar
activity at $\lambda=42°N$, and converted the measured fluxes to
neutron leakage currents as follows.

1.   Solar Cycle Correction:

Lingenfelter (1963b) made calculations on the
variation of neutron leakage rate with respect to neutron
energies, latitudes, and cycle of solar activity.   His
results were used for these corrections.

For fast neutrons with energies between 1 Mev and
10 Mev the leakage rate at geomagnetic latitude $40°N$ during
solar minimum (1953-1954) was calculated to be 0.112 neutron/
sec-cm^2, and during solar maximum (1957-1958) was 0.091
neutron/sec-cm^2.   The difference was 18.7%.   Using the Mt.
Washington neutron monitor counting rate as the reference
for the cosmic ray intensity the maximum counting rate was
100% in 1953-1954 solar minimum period while in 1957-1958
solar maximum period the minimum counting rate was 75.7%.
On June 22, 1973, the neutron monitor counting rate was 88.8%.
The difference of the leakage rate between June 22, 1973
and solar minimum was $(100\%-88.8\%) \times \dfrac{18.7\%}{24.3\%} = 8.7\%$.   Thus,
the neutron leakage rate on June 22, 1973 was 91.3% of the
leakage rate at solar minimum yeilding a correction factor
of 100%/91.3% -- 1.1 for fast neutrons.   Based on the same

argument, the correction factor for neutrons with energies greater than 10 Mev was also assumed to be 1.1.

2. Altitude Correction

To convert the observations to a neutron leakage rate we first extrapolated our results to the top of the atmosphere using the experimental results of Preszler et. al (1974). The ratio of the neutron flux at 0 g/cm^2 to the neutron flux at 4 g/cm^2 is 0.8 in the energy range 10 Mev to 100 Mev. This factor was assumed to be also valid in the energy range 2 Mev to 10 Mev.

3. Conversion of Leakage Flux to Leakage Current:

In order to convert the neutron leakage flux to the neutron current it is necessary to know the angular distribution of neutrons at the top of the atmosphere. The experimental data on the neutron angular distribution at this moment are incomplete. For the relation between leakage current and leakage flux we have:

$I = \int_{2\pi} F(E_n,\theta) \cos\theta \, d\Omega$, where I: leakage current

$F(E_n,\theta)$: leakage flux

θ: zenith angle.

If the neutron flux is isotropic, the ratio of I to $F(E_n,\theta)$ is 0.5. According to the calculations of Merker (1972), the ratio for 19 Mev$\leq E_n \leq$40 Mev is 0.46, for 40 Mev$\leq E_n \leq$100 Mev is 0.49, and for 100 Mev$\leq E_n \leq$400 Mev is 0.42. They are not significantly different from 0.5 which was taken as the correction factor.

The total correction factor was 1.1x0.8x0.5=0.44.

The neutron leakage current spectrum measured in this flight normalized to solar minimum at $\lambda=42^{\circ}N$ is shown in Fig. 10-1 and Fig. 10-2. The leakage current at $E_n=2$ Mev is $0.065 \begin{smallmatrix} +0.014 \\ -0.012 \end{smallmatrix}$ neutron/cm^2-sec-Mev, and at $E_n=10$ Mev is $3.1 \times 10^{-3} \begin{smallmatrix} +7.5 \times 10^{-4} \\ -7.2 \times 10^{-4} \end{smallmatrix}$ neutron/cm^2-sec-Mev. From $E_n=2$ Mev to $E_n=10$ Mev the spectrum can be described by a power law energy spectrum with an index of -1.9. From 10 Mev to 75 Mev the spectrum becomes flat. At $E_n=50$ Mev the leakage current is $7.1 \times 10^{-3} \begin{smallmatrix} +2.3 \times 10^{-3} \\ -1.3 \times 10^{-3} \end{smallmatrix}$ neutron/cm^2-sec-Mev.

CHAPTER XI

DISCUSSION AND CONCLUSION ON NEUTRON MEASUREMENTS

The theoretical calculations and the previous meas-
urements of neutron energy spectra, fluxes, and leakage cur-
rents have been reviewed in Chapter II and Chapter IV.

Our measurement of the neutron leakage current below
10 Mev agrees with the general tendency of most measurements
(Fig. 10-1, Fig. 10-2). Above 10 Mev the neutron spectrum
becomes flat, as shown by the measurements of White et al.
(1972), Klumpar et al. (1973), and the calculations of Arm-
strong et al. (1973). But, in the region 20 Mev to 50 Mev
our results show a significant difference from the three
fore-mentioned results by approximately a factor of three.
There are two main reasons for the difference between the
previous measurements and ours. First, our assumption of the
power law spectrum with index -2 above 100 Mev may not be
correct. If the spectrum above 100 Mev is steeper than that
assumed, then the deduced neutron spectrum in the region 20
Mev to 50 Mev tends to have a higher magnitude. But, the
magnitude of the calibrated proton response function is
decreasing with the increasing incident neutron energy; the
number of recoil protons per Mev is becoming less as the
neutron energy increases (except those channels under the
Gaussian peak). Thus, in the energy region 20 Mev to 50 Mev
the proton recoil spectrum is not sensitive to the incident
neutrons with energies above 100 Mev unless the neutron

spectrum beyond 100 Mev changes dramatically. Second, the difference arises because we used calibrated response functions directly to unfold the neutron spectrum. The total cross section of the neutron-carbon (n-C) scattering is well studied, but the cross section of individual inelastic scattering such as $C^{12}(n,p)B^{12}$, $C^{12}(n,np)B^{11}$, $C^{12}(n,n3\alpha)$, ..., etc., is not. The widely used theoretical calculations (Kurz, 1964; Stanton, 1971) are not able to reproduce the calibrated response functions for neutrons with energies above 30 Mev. The main reason is because the energy distribution of the protons from the reaction $C^{12}(n,p)B^{12}$ is not treated properly. As we pointed out in Chapter VII, Kurz, (1964) and Stanton, (1971) assumed that the proton energy distribution was a phase space distribution. This assumption tends to pile up the protons from the reaction $C^{12}(n,p)B^{12}$ at low energies. By this assumption, for high energy neutron measurements, we not only have wrong energy distribution of protons but also underestimate the efficiency of the detector if the proton threshold energy is not set near zero. From Fig. 7-7, it is clear that this assumption introduces a large error in high energy neutron response functions.

In the measurement of Klumpar et al. (1973) the same kind of 2 inch detector was used as in this flight. The energy range covered was from 3 Mev to 18 Mev proton energy. The discrepancy between their results and ours comes from the different response functions used to unfold the spectrum. In their unfolding process the proton recoil spectrum from

the neutron-proton (n-p) scattering was used for the response function. In a neutron field, if the maximum energy of neutrons is about 10 Mev, then this approach is valid, because essentially no proton from n-C inelastic scatterings contributes to the observed proton recoil spectrum. But, if there are large fluxes of atmospheric neutrons with energies above 10 Mev, then inelastic n-C scatterings tend to contribute a significant amount of protons. From our measurements, there are relatively large neutron fluxes in the region 20 Mev to 100 Mev. Hence, we expect that protons from inelastic n-C scatterings contribute to the observed proton recoil spectrum. If protons from inelastic n-C scatterings are not considered in the response functions used for the neutron spectrum unfolding process, then response functions tend to have less protons than they should have. Consequently, the unfolded neutron spectrum tends to have larger magnitude.

In the measurements of White et al. (1972) a large detector with a double scattering telescope was used. In the double scattering neutron telescope one depends upon the pure n-p elastic scattering in the first detector to get the angular information about incident neutrons. Suppose that the scattered neutron from the first detector is produced by the reaction $C^{12}(n,n3\alpha)$, but the pulse shape discrimination technique is not used in the first detector. The question then arises: Is there any way to tell that this 'scattered' neutron is not from n-p scattering? If the pulse shape discrimination were used in the first detector, then how can we

determine whether the scattered neutron is from the reaction

$C^{12}(n,np)B^{11}$ or n-p scattering? Kinimatical arguments were

used in the Heidbreder experiment (1970). This, however,

necessitates analyzing each event. If these protons are not

properly considered, it tends to underestimate the efficiency

of the neutron telescope (Appendix A); hence, overestimate

the neutron flux.

The neutron spectrum measured in this flight reveals

none of the structures predicted by Wilson et al. (1969).

This does not exclude the possibility of the existence of

these structures. From this measurement, and other previous

measurements with recoil proton detectors, the neutron spec-

trum between 1 Mev to 10 Mev is falling as a power law. Below

10 Mev, the protons from n-p scatterings distribute uniformly

from zero to the energy of incident neutrons. As a consequence,

the structures in the neutron spectrum are smoothed out in

the proton recoil spectrum. Furthermore, the technique we

used in the neutron spectrum unfolding can only yield the

gross curve of the neutron spectrum; the fine structures are

difficult to deduce.

Since 1958, after the discovery of Van Allen belts,

many neutron measurements have been carried out. But, for

most, the energy range was limited to less than 10 Mev. From

these measurements in the energy region 1 Mev to 10 Mev the

cosmic ray albedo neutron has been found to be insufficient

to explain the flux of protons trapped in the radiation belts

in the same energy range. At neutron energies above 10 Mev

Hess and Killeen (1966) evaluated the strengths of the cosmic
ray albedo neutron decay and the solar proton albedo neutron
decay mechanisms. They used the calculated neutron energy
spectrum, produced by solar protons, of Lingenfelter et al.
(1964), and found that the solar proton albedo neutron decay
is not a major source for the trapped protons. For the cosmic
ray albedo neutron decay mechanism, the flux was assumed to
be 3×10^{-5} neutrons/sec-cm^2-Mev at a neutron energy of 50 Mev;
taken from the neutron spectrum of Lingenfelter (1963b).
The results revealed that in order to explain the trapped
protons by this mechanism the neutron source strength should
be increased by at least a factor of 20. Dragt et al. (1966)
used the neutron spectrum from the calculations of Lingenfelter
(1963b) and concluded that the trapped protons with energies
greater than 20 Mev could be explained by the cosmic ray
albedo neutron decay injection only if the ratio of the albedo
neutron fluxes to the known mean atmospheric densities
encountered by the trapped protons were a factor of 50 greater.

Recent measurements of White et al. (1972), Klumpar
et al. (1973), and Kanbach et al. (1974) in the energy
region 20 Mev to 250 Mev have reopened the source strength
question because they show that the neutron energy spectrum
predicted by Lingenfelter (1963b) is inadequate for neutron
energies above 10 Mev. Furthermore, the agreement between
the measurements and the Monte Carlo calculations of Armstrong
et al. (1973) and of Merker (1972) using the known cosmic ray
spectrum is good. Claflin et al. (1973) have shown that the

mechanism of cosmic ray albedo neutron decay can supply the protons with energies above 30 Mev in the inner radiation belt, if the neutron fluxes measured by White et al. (1972) are used. But, for $L \geq 1.7$, the neutron fluxes from the measurements of White et al. (1972) tend to give the number of trapped protons a factor of 5-11 too high in the energy range 40 Mev to 100 Mev (White, 1973). Our results support the cosmic ray albedo neutron decay theory and provide new information on the neutron source strength needed for the detailed evaluation of the cosmic ray neutron albedo decay theory.

BIBLIOGRAPHY

Albernhe, F. and R. Talon, Determination du Spectre et du Flux de Neutrons Atmospheriques Rapides en periode de Soleil Calme et a une Latitude Geomagnetique de 46° Nord,   Ann. Geophys. 25, 99 (1969).

Albert, R. D., F. Gilbert, and W. N. Hess, Measurements of Charged Particles and Neutrons on Discovered Flights, J. Geophys. Res., 67, 3537 (1962)

Allen W. D., Neutron Detection, William Clowes and Sons Limited, London and Beccles, (1960)

Armstrong, T. W., K. C. Chandler, and J. Barish, Calculations of Neutron Flux Spectra Induced In the Earth's Atmosphere by Galactic Cosmic Rays, J. Geophys. Res. 78, 2715 (1973)

Baird, G. A. and B. G. Wilson, Solar Minimum Measurements of Fast Neutrons at High Altitude, Can. J. Phys. 44, 2131 (1966)

Bame S. J., J. P. Conner, F. B. Brumley, and R. L. Hostetler, Neutron Flux and Energy Spectrum above the Atmosphere J. Geophys. Res. 68, 1221 (1963)

Beckurts, K. H. and K. Wirtz, Neutron Physics, Springer-Verlag, New York Inc. (1964) Chapter 5

Biermann, L., O. Haxel, and A. Schluter, Neutrale Ultrastrah- lung von der Sonne, Z. Naturforschr. 6A, 47 (1951)

Boella G., G. D. Antoni, C. Dilworth, M. Panetti, L. Scarsi and D. S. Intriligator,   J. Geophys. Res. 70, 1019

Claflin, E., and R. S. White, The Source of Inner Belt Protons,   J. Geophys. Res. 78, 4675 (1973)

Dragt, A. J., M. M. Austin, and R. S. White, Cosmic Ray and Solar Proton Albedo Neutron Decay Injection, J. Geophys. Res. 71, 1293 (1966)

Evans, R. D., The Atomic Nucleus, McGraw-Hill Book Company, (1955) page 604

Forrest, D. J., A Search for High Energy Solar Neutrons, Ph. D Thesis University of New Hampshire, (1969)

Freden, S. C., and R. S. White, Trapped Proton and Cosmic Ray Albedo Neutron Fluxes, J. Geophys. Res. 67, 25 (1962)

Gabriel, T. A., R. T. Santoro and R. G. Alsmiller, Jr.,
        An Approximate High-Energy Alpha-Particle-Nucleus-
        Collision Model,   Nucl. Sci. Eng., 44, 104 (1971)

Gooding, T. J., and H. G. Pugh, The Response of Plastic
        Scintillators to High-Energy Particles,
        Nucl. Instr. and Meth. 7, 189 (1960)

Gross, E., The Absolute Yeild of Low-Energy Neutrons from
        190-Mev Proton Bombardment of Gold, Silver, Nickel,
        Aluminum, and Carbon, Lawrence Radiation Lab.
        (Berkeley, Calif.), Rept. UCRL-3330, Feb. 29, 1956

Haymes, R. C., Fast Neutrons in the Earth's Atmosphere,
        J. Geophys. Res. 69, 841 (1964)

Heidbreder, E., K. Pinkau, C. Reppin, V. Schönfelder
        Measurement of the Distribution in Energy and
        Angle of High-Energy Albedo Neutrons and Determina-
        tion of an Upper Limit for the Solar Neutron Flux,
        J. Geophys. Res. 75, 6347 (1970)

Hess, W. N., H. W. Patterson, R. Wallace, and E. L. Chupp,
        Cosmic-Ray Neutron Energy Spectrum, Phys. Rev. 116,
        445 (1959)

Hess, W. N., E. H. Canfield, and R. E. Lingenfelter,
        Cosmic-Ray Neutron Demography, J. Geophys. Res.
        66, 665 (1961)

Hess, W. N., and J. Killeen, Spatial Distribution of Protons
        from Neutron Decay Trapped by the Geomagnetic Field,
        J. Geophys. Res. 71, 2799 (1966)

Holt, S. S., R. B. Mendell and S. A. Korff, Fast Neutron
        Latitude Variations in the Atmosphere at Solar
        Minimum, J. Geophys. Res. 71, 5109, (1966)

Hubbell, Photon Cross Sections, Attenuation Coefficients,
        and Energy Absorption Coefficients from 10 Kev to
        100 Gev,   NSRDS-NBS 29 August 1969

Jenkins, R. W., S. O. Ifedili, J. A. Lockwood and H. Razdan
        The Energy Dependence of the Cosmic Ray Neutron
        Leakage Flux in the Range 0.01 - 10 Mev,
        J. Geophys. Res. 76, 7470 (1971)

Johns, H. E., C. V. Cormack, S. A. Denesuk and G. F. Whitmore
        Initial Distribution of Compton Electrons,
        Can. J. Phys. 30, 556 (1952)

Kanbach, G., C. Reppin, and V. Schönfelder, Support for CRAND
        Theory from Measurements of Earth Albedo Neutrons

Between 70 and 250 Mev,   J. Geophys. Res. 79, 5159 (1974)

Klumpar, D. M. The Flux and Energy Spectrum of Fast Neutrons and Gamma Rays at Balloon Altitudes, Ph. D Thesis, University of New Hampshire (1972)

Klumpar, D. M., J. A. Lockwood, R. N. St. Onge, and L. A. Friling, Energy Spectrum and Flux of 3- to 20 Mev Neutrons and 1 to 10 Mev Gamma Rays in the Atmosphere J. Geophys. Res. 78, 7959 (1973)

Kurz, R. J., A 709/7090 Fortran II Program to Compute the Neutron Detection Efficiency of Plastic Scintillator for Neutron Energies from 1 to 300 Mev, Lawence Radiation Laboratory, UCRL-11339, March, 1964

Kuchnir, F. T. and F. J. Lynch, Time Dependence of Scintillations and the Effect on Pulse-Shape Discrimination, IEEE Transactions on Nuclear Science NS-15, 107 (1968)

Landau, L., On the Energy Loss of Fast Particles by Ionization, J. Phys. VIII, 201 (1944)

Lingenfelter, R.E., Production of Carbon 14 by Cosmic-Ray Neutrons, Rev. Geophys. 1, 35 (1963a)

Lingenfelter, R. E., The Cosmic Ray Neutron Leakage Flux, J. Geophys. Res. 68, 5633 (1963b)

Lingenfelter, R. E., and E. J. Flamm, Neutron Leakage Flux from Interactions of Solar Protons in the Atmosphere J. Geophys. Res. 69, 2199 (1964)

Lockwood, J. A., Neutron Measurement in Space, Space Sci. Rev. 14, 663 (1973)

Lord, J. J., The Altitude and Latitude Variation in the Rate of Occurrence of Nuclear Disintegrations Produced in the Stratosphere by Cosmic Rays, Phys. Rev. 81, 901 (1951)

Lynch, F. J., New Liquid Scintillators with Higher Speed and Efficiency, IEEE Trans. on Nucl. Sci. NS-15, 102 (1968)

Marion, J. B. and J. L. Fowler, Fast Neutron Physics, Part II John Wiley & Sons, Inc. New York-London (1963)

Mathews and Walker, Mathematical Method of Physics, W. A. Benjamin, Inc. New York, (1965)

Mendell, R. B., and S. A. Korff, Fast-Neutron Detector with
     Discrimination Against Background Radiation,
     Rev. Sci. Instr., 34, 1356 (1963)

Merker, M., Energetic Neutrons Leaking from the Top of the
     Atmosphere, Phys. Rev. Letters, 29, 1531 (1972)

Merker, M., E. S. Light, H. J. Verschell, R. B. Mendell, and
     S. A. Korff, Time Dependent Worldwide Distribution
     of Atmospheric Neutrons and of Their Products,
     J. Geophys. Res. 78, 2727 (1973)

Miyake, S., K. Hinotani, I. Katsumata, and T. Kaneko,
     Cosmic Ray Nuclear Interactions in Nitrogen Gas,
     J. Phys. Soc. Japan, 12, 845 (1957)

Newkirk, L. L., Calculation of Low-Energy Neutron Flux in
     the Atmosphere by the S_n Method,
     J. Geophys. Res. , 68, 1825 (1963)

Owen, R. B., Pulse Shape Discrimination Identifies Particle
     Types, Nucleonics 17, 92 (September, 1959)

Phillips, H. B., and R. K. Swank, Measurements of Scintillation
     Life times, Rev. Sci. Instr. 24, 611 (1953)

Pinkau, K., Die Messung Solares und Atmosphärischer Neutronen
     Z. Naturforsch. 21A, 2100 (1966)

Preszler, A. M., G. M. Simnett, and R. S. White, Angular
     distribution and Altitude Dependence of Atmospheric
Neutrons From 10 to 100 Mev J. Geophys. Res., 79, 17 (1974)

Price, W. J., Nuclear Radiation Detection,
     McGraw-Hill Book Company Inc. (1971)

Riddle, R. A. J., G. H. Harrison, and P. G. Roos, Direct
     Measurement of Neutron Detector Efficiencies,
     Nucl. Instr. and Meth. 121, 445 (1974)

Singer, S. F., Radiation Belt and Trapped Cosmic Ray Albedo,
     Phys. Rev. Lett. 1, 171 (1958a)

Singer, S. F., Trapped Albedo Theory of the Radiation Belt,
     Phys. Rev. Lett. 1, 181 (1958b)

St. Onge, R. N., The Energy Spectrum and Flux of Fast Neutrons
     in the Atmosphere, Ph. D. Thesis, University of New
     Hampshire, D-cember 1968

St. Onge, R. N., and J. A. Lockwood, A Simple High Resolution
     Pulse Shape Discriminator, Nuc. Instr. and Meth. 69,
     25 (1969a)

St. Onge, R. N., and J. A. Lockwood, A Total Enclosing Active
        Charged Particle Shield, Nuc. Instr. and Meth.
        69, 347 (1969b)

Stanton, N. R., A Monte Carlo Program for Calculating
        Neutron Detection Efficiencies in Plastic Scintil-
        lator, COO-1545 92 (1971)

White, R. S., S. Moon, A. M. Preszler, and G. M. Simnett,
        Earth Albedo and Solar Neutrons, University of
        California, Riverside, Research Report IGPP-UCR-
        72-16, May 18, 1972

White, R. S., High-Energy Proton Radiation Belt, Rev. of
        Geophys. and Space Phys. 11, 595 (1973)

Wilson, J. W., J. J. Lambiotte, and T. Foelsche, Structure
        in the Fast Neutron Spectra of Atmospheric Neutrons,
        J. Geophys. Res. 74, 6494 (1969)

Wright, G. T., Scintillation Decay Times of Organic Crystals,
        Phys. Soc. Proc. 69B, 358 (1956)

APPENDIX A

DOUBLE SCATTERING TECHNIQUE FOR DIRECTIONAL DETECTORS

For a single omnidirectional detector we do not
have information about the angular distribution of gamma
rays and neutrons. To test the cosmic ray neutron albedo
decay theory we need to know the magnitude of the neutron
leakage current rather than leakage flux. In order to
convert the leakage flux into leakage current the angular
distribution of the neutrons on the top of the atmosphere
has to be known. For cosmic gamma rays, it is essential
to have the directional information, so the cosmic gamma
ray sources can be identified.

In the following sections we discuss the telescope
system consists of two detectors and a time of flight system
incorporated between them. If a neutron or a gamma ray
has a scattering in the first detector and a second
scattering in the second detector then we are able to
measure the energy and the direction of the incoming
particle.

A.1 Compton Telescope for the Measurements of Directional

Fluxes and Energy Spectra of Gamma Rays

In the Compton scattering process (Fig. A-1) if the
energy of the electron $E_{e'}$ and the energy of the scattered
γ-ray $E_{\gamma'}$ are measured, we can calculate the energy of the in-
cident γ-ray E_γ by $E_\gamma = E_{e'} + E_{\gamma'}$. Morever, since

$$\theta' = \cos^{-1}(1 - \frac{E_\gamma / E_{\gamma'} - 1}{E_\gamma / m_0 c^2}), \qquad \text{(Hubbell, 1969)}$$

we can also determine from E_γ and $E_{\gamma'}$ the angle between the
incident γ-ray and the scattered γ-ray. But, in the coordinate
system with the z-axis along the reverse direction of the scat-
tered γ-ray, the azimuthal angle of the incident γ-ray is in-
determinate if we do not determine the azimuthal angle of recoil
electron. So the incident γ-ray will be on a cone with half
angle θ'.

Assuming that the distribution of γ-rays at balloon
altitudes is symmetrical with respect to the zenith, we may put
two detectors, one above the other, with the central line of
the two detectors pointing toward zenith. The first detector
will be used to determine the energy of the recoil electron and
the second detector to measure the scattered γ-ray. In this
scheme we assume that all the energy of the scattered γ-ray is
deposited in the second detector, which is valid only if the
scattered γ-ray stops in the second detector and the secondary
electrons or positrons produced by this γ-ray do not

escape the detector. This assumption is a reasonable approximation because the differential cross section of Compton scattering is:

$$\frac{d\sigma}{dE_e} = \frac{\pi \gamma_0^2}{\kappa E_\gamma}\{1+[1-\frac{2f'}{1+2\kappa-2\kappa f'}]^2+\frac{\kappa^2(\frac{2f'}{1+2\kappa-2\kappa f'})^2}{1+\kappa\frac{2f'}{1+2\kappa-2\kappa f'}} \} \quad cm^2/Mev$$

<div align="right">(Johns, 1952)</div>

where, $f'=\dfrac{E_e}{E_{emax}}$, E_{emax} is the maximum energy of the electron.

$$\kappa = \frac{E_\gamma}{m_0 c^2}$$

$\gamma_0 =$ radius of the electron

and there is a sharp peak at E_{emax}. (Fig.A-1, Fig. A-2 and Fig.A-3). Thus, in Compton scattering the probability for the recoil electron energy to have about the energy of the γ-ray is very high.

A 1.1 Efficiency Of The Compton Telescope

To calculate the efficiency of the Compton telescope we must take into account the following factors:

A)   Upper Detector

1.   Attenuation of γ-ray flux by the charged particle shield (ACD);

2.   The probability for a Compton scattering to occur with the scattered γ-ray going into the solid angle ΛΩ subtended by the second detector;

3.   The recoil electron energy is above the threshold energy of the detector.

B) Lower Detector

    4. Attenuation of the scattered γ-ray by the ACD;

    5. The probability of γ-ray to produce electrons (and positrons) with the total energy of recoil electrons above the threshold energy of the detector.

In this calculation we do not include the self gating effect.

    Based on these considerations, we have the relation:

$$\epsilon(E_\gamma,\theta)=F_1 \cdot F_2 \cdot F_3 \cdot F_4 \cdot F_5$$

where $\epsilon(E_\gamma,\theta)$, the efficiency of the system, is a function of the angle and energy of the incident γ-ray. F_1, F_2, F_3, F_4 and F_5 are defined as follows:

    F_1: attenuation of ACD

$$F_1 = \exp\left[-\frac{d_1}{\lambda_{p_1}(E_\gamma)} \cdots \frac{d_1}{\lambda_{c_1}(E_\gamma)}\right]$$

    F_2: Probability that a Compton scattering occurs in the first detector with the scattered γ-ray going into the solid angle subtended by the second detector.

$$F_2 = \frac{\frac{1}{\lambda_c(E_\gamma)}}{\frac{1}{\lambda_p(E_\gamma)}+\frac{1}{\lambda_c(E_\gamma)}}\left[1-e^{-\left(\frac{1}{\lambda_p(E_\gamma)}+\frac{1}{\lambda_c(E_\gamma)}\right)}\right]\frac{\frac{d\sigma(E_\gamma,\theta)}{d\Omega}}{N_e\lambda_c(E_\gamma)}\Delta\Omega$$

    F_3: A step function which requires that the recoil electron in the first detector be greater than the threshold.

    $F_3 = H(E_{e_1}-E_{th_1})$

    F_4: Attenuation by the ACD for scattered γ-ray which passes from the first to the second detector.

$$F_4 = \exp\left[-\frac{d_1+d_2}{\lambda_{p_1}(E_{\gamma'})} - \frac{d_1+d_2}{\lambda_{c_1}(E_{\gamma'})}\right]$$

F_5: The probability for the scattered γ-ray to produce an observable event in the second detector.

$$F_5 = \left\{1-\exp\left[-\frac{1}{\lambda_p(E_{\gamma'})}^2 - \frac{1}{\lambda_c(E_{\gamma'})}^2\right]\right\}\left[\frac{\frac{1}{\lambda_c(E_{\gamma'})}}{\frac{1}{\lambda_p(E_{\gamma'})}+\frac{1}{\lambda_c(E_{\gamma'})}}\right. \cdot$$

$$\left. \cdot P(E_{e_2}>E_{th_2}) + \frac{1/\lambda_p(E_{\gamma'})}{1/\lambda_p(E_{\gamma'})+1/\lambda_c(E_{\gamma'})}H(E_{\gamma'}-2m_0c^2-E_{th_2})\right]$$

where,

d_1 : Thickness of anticharged particle dome for first detector

d_2 : Thickness of anticharged particle dome for second detector

l_1 : Effective length of first detector

l_2 : Effective length of second detector

E_{th_1} : Threshold energy of the first detector

E_{th_2} : Threshold energy of the second detector

$H(E-E')$: Step function $H(E-E')=1$ $E \geq E'$

                                                    $=0$ $E<E'$

E_{e_1} : Energy of recoil electron in the first detector

E_{e_2} : Energy of recoil electron in the second detector

E_γ : Energy of the incident γ-ray

$E_{\gamma'}$: Energy of the scattered γ-ray which goes into second detector

θ : Incident angle of γ-ray with respect to the central line connecting the centers of two detectors

$P(E_{e_2}>E_{th_2})$: Probability that $E_{e_2}>E_{th_2}$

$\Delta\Omega$: Solid angle subtended by the second detector

$\dfrac{d\sigma(E_\gamma,\theta)}{d\Omega} = \dfrac{d\sigma_c^{KN}}{d\Omega}$: Differential cross section of Compton scattering

λ_{p_1}: Mean free path of pair production of γ-ray in the ACD

λ_{c_1}: Mean free path of Compton scattering of γ-ray in the ACD

λ_p: Mean free path of pair production of γ-ray in the detector

λ_c: Mean free path of Compton scattering of γ-ray in the detector

$\lambda_{p_1}, \lambda_{c_1}, \lambda_p$ and λ_c are derived in the following (Hubbell, 1969).

$$\sigma_c^{KN} = 2\Pi\gamma_0^2 \left\{ \frac{1+\kappa}{\kappa^2}\left[\frac{2(1+\kappa)}{1+2\kappa} - \frac{\ln(1+2\kappa)}{\kappa}\right] + \frac{\ln(1+2\kappa)}{2\kappa} - \frac{1+3\kappa}{(1+2\kappa)^2}\right\} cm^2/electron$$

$$\frac{d\sigma_c^{KN}}{d\Omega} = \frac{\gamma_0^2}{2}\{1+\kappa(1-\cos\theta)\}^{-2} \cdot \left[1+\cos^2\theta + \frac{\kappa^2(1-\cos\theta)^2}{1+\kappa(1-\cos\theta)}\right] \quad \frac{cm^2/electron}{steradian}$$

$$K_n^{BH} = \frac{Z^2\gamma_0^2}{137}\left\{\frac{28}{9}\ln(2\kappa) - \frac{218}{27} + \left(\frac{2}{\kappa}\right)^2\left[6\ln(2\kappa) - \frac{7}{2} + \frac{2}{3}\ln^3(2\kappa) - \ln^2(2\kappa)\right.\right.$$

$$\left.-\frac{\Pi^2}{3}\ln(2\kappa) + 2\xi(3) + \frac{\Pi^2}{6}\right] - \left(\frac{2}{\kappa}\right)^4\left[\frac{3}{16}\ln(2\kappa) + \frac{1}{8}\right]$$

$$\left.-\left(\frac{2}{\kappa}\right)^6\left[\frac{29}{9\times256}\ln(2\kappa) - \frac{77}{27\times512} + \cdots\right]\right\} \quad for \ E_\gamma \geq 2Mev$$

$$= \frac{Z^2\gamma_0^2}{137}\frac{2\Pi}{3}\left(\frac{\kappa-2}{\kappa}\right)^3\left[1 + \frac{\rho}{2} + \frac{23}{40}\rho^2 + \frac{11}{60}\rho^3 + \frac{29}{960}\rho^4 + \cdots\right] \quad for \ E_\gamma \leq 2Mev$$

where, $\kappa = \dfrac{E_\gamma}{m_0 c^2}$

$$\xi(3) = \sum_{n=1}^{\infty}\frac{1}{n^3} = 1.2020569$$

$$\rho = \frac{2\kappa-4}{2+\kappa+2\sqrt{2}\ \kappa}$$

σ_c^{KN}: total cross section of Compton scattering from

the Klein-Nishina formula

K_n^{BH} : cross section of pair production (Born,unscreened)

Z : atomic number

The cross section of pair production due to both nuclei and electrons is

$$K_T^{BH} = Z(Z+\eta) \left(\frac{K_n^{BH}}{Z^2}\right)$$

where,

$$\eta = \frac{3+\frac{Z}{137}}{9} \ln\left(\frac{\kappa}{2}\right) - 0.00635 \ln^3\left(\frac{\kappa}{2}\right)$$

For the NE213 detector,

$$\frac{1}{\lambda_p} = n_H K_T^{BH}(\text{hydrogen}) + n_C K_T^{BH}(\text{carbon})$$

$$= 1.213 \, n_C K_T^{BH}(\text{hydrogen}) + n_C K_T^{BH}(\text{carbon})$$

if we let $K_n^{BH} = Z^2 M$, then,

$$\frac{1}{\lambda_p} = 1.213 \times 1 \times \left(1+\frac{3+\frac{1}{137}}{9} \ln\frac{\kappa}{2} - 0.00635 \ln^3\frac{\kappa}{2}\right) M \, n_C +$$

$$+ \quad 6 \times \left(6+\frac{3+\frac{6}{137}}{9} \ln\frac{\kappa}{2} - 0.00635 \ln^3\frac{\kappa}{2}\right) M \, n_C$$

$$= \left(2.434 \ln\frac{\kappa}{2} - 0.045 \ln^3\frac{\kappa}{2} + 37.21\right) M \, n_C$$

Similarly, for NE102,

$$\frac{1}{\lambda_{p_1}} = \left(2.397 \ln\frac{\kappa}{2} - 0.045 \ln^3\frac{\kappa}{2} + 37.21\right) M \, n_C.$$

The mean free path of Compton scattering is calculated by

$$\frac{1}{\lambda_c} = n_e \, \sigma_c^{KN} \quad \text{for NE213 and} \quad \frac{1}{\lambda_{c_1}} = n_{e'} \, \sigma_c^{KN} \quad \text{for NE102}$$

where,

$n_H = 4.76 \times 10^{22}$ hydrogen/cc (hydrogen density of NE213)

$n_C = 3.93 \times 10^{22}$ carbon/cc (carbon density of NE213)

$n_{H'} = 5.04 \times 10^{22}$ hydrogen/cc (hydrogen density of NE102)

$n_{C'} = 4.57 \times 10^{22}$ carbon/cc (carbon density of NE102)

$n_e = 2.83 \times 10^{23}$ electron/cc (electron density of NE213)

$n_{e'} = 3.28 \times 10^{23}$ electron/cc (electron density of NE102)

The efficiency turns out to be a strong function of the energy and the incident angle of the γ-rays (Fig.A-5). There are two cutoff angles. The minimum cutoff angle is due to the threshold energy of the first detector. Too small an incident angle will produce an electron with an energy below the threshold energy in the first detector. The maximum cutoff angle is due to the threshold of the second detector which arises because for large incident angles the scattered γ-rays have small energies. If the energy of the scattered γ-ray is too small to trigger the detector, it is simply missed. Since the efficiency at large incident angles is always much smaller than at small angles, the threshold of first detector must be kept low to increase the efficiency of the system. However, the counting rate increases rapidly with the lowered threshold and hence the number of random coincidence may become a significant factor. From the efficiency curves, we observe that the efficiency decreases very rapidly with increasing zenith angle. At small incident angles the recoil electron has too small an energy for the escape factor in the first detector to be significant. Furthermore, the efficiency

decreases rapidly with increasing energy. For our system

the effective energy range is about 2 Mev - 20 Mev, but the

escape effect is only important at highest energies in this

range. For the 5 inch detector the maximum energy deposit

for an electron is about 30 Mev, hence the self-gating from

escaping electrons or positrons is important only for electrons

above 30 Mev.

A.1.2 Intrinsic Uncertainty Of Compton Telescope

From the pulse height information in each detector

we determine E_{e_1} and E_{e_2} (Fig.A-1) and then calculate the energy

and the angle of the incident γ-ray from

$$E_\gamma = E_{\gamma'} + E_{e_1} = E_{e_2} + E_{e_1} \quad (A-1-1)$$

$$\theta = \cos^{-1}(1- \frac{E_\gamma/E_{\gamma'} - 1}{E_\gamma/m_0 c^2}) = \cos^{-1}(1- \frac{\frac{E_{e_1}+E_{e_2}}{E_{e_2}} - 1}{\frac{E_{e_1}+E_{e_2}}{m_0 c^2}}) \quad (A-1-2)$$

This treatment does not consider the uncertainty in the electorn

energy determination. It also neglects the fact that E_{e_2}

can be produced by all γ-rays with energy greater than about

$E_{e_2} + \frac{m_0 c^2}{2}$. In Fig. A-6 and Fig. A-7, every

line corresponds to a particular γ-ray whose true incident

angle and energy are indicated by the beginning point at left

hand side. When we make a particular measurement, every point

along the line is a possible result. Suppose the energy un-

certainties in E_{e_1} and E_{e_2} are $\pm\Delta E_{e_1}$ and $\pm\Delta E_{e_2}$ respectively.

We are then able to determine the four angle-energy points

(A,B,C, and D) as shown in Fig.A-8. Let us define the region

confined by the four angle-energy points to be the experi-
mental error region (EER). Any solid line passes through the EER
will be a candidate for the real energy and angle of the incident
γ-ray. These lines will constitute a band. Let us define
this band to be the accepted zone, as shown in Fig.A-8 by
dashed lines.

It is shown in Fig.A-2,A-3,and A-4 that an electron spec-
trum of Compton scattering has a sharp peak toward the maximum
recoil electron energy. From this property we can find the
relative probability of every energy-angle point in Fig.A-9.

As we have learned every point inside the
accepted zone is a possible answer but from the property
shown in Fig.A-9, we find that the probability for these
possible values is increasing very rapidly toward the value
we calculate from equations (A-1-1) and (A-1-2). To evaluate
this kind of intrinsic ambiguity we may use the following con-
vention. Since the largest uncertainty arises from the de-
termination of E_{e_2}, it is reasonable to say that in most
cases, E_{e_2} is produced by one of these γ-rays with energy
between E_{γ_1} and E_{γ_2}, where E_{γ_1} is the energy of γ-ray which
produces an electron having maximum energy E_{e_2}. E_{γ_2} is the
γ-ray which produces an electron with 50% probability to
have energy above E_{e_2}. By this convention, we are able to
determine the uncertainty of angle and energy which includes
EER and the intrinsic ambiguity.

For example: if we measure $E_{e_1} = 1$ Mev $\pm$ 0.2 Mev

$$E_{e_2} = 3 \text{ Mev} \pm 0.3 \text{ Mev}$$

then, what is the energy and the angle of the incident γ-ray?
The EER will be determined by the following four points,

	E_{e_1} Mev	E_{e_2} Mev	E_γ Mev	θ o
A.	1.2	3.3	4.5	16.5
B.	1.2	2.7	3.9	19.7
C.	0.8	3.3	4.1	14.1
D.	0.8	2.7	3.5	16.9

The angles and energies of E_{γ_2} corresponding to points A, B, C and D are:

	E_{e_1} Mev	E_{e_2} Mev	E_{γ_2} Mev	θ o
A'.	1.2	3.3	5.9	12.2
B'.	1.2	2.7	5.1	14.2
C'.	0.8	3.3	5.5	10.3
D'.	0.8	2.7	4.7	12.0

These eight points are shown in Fig.A-8 and the uncertainty in angle and energy is the area surrounded by A'C'D'CDBAB'A'. From the calculation of E_{γ_1} we also get a set of four points. These four points are inside the area we just described, so that we do not have to show them because the upper and the lower bounds of the uncertainty are already determined.

THE COMPUTER PROGRAM TO CALCULATE THE EFFICIENCY OF THE

COMPTON TELESCOPE

This program gives the relation among the energy of γ-ray, incident angle and the efficiency of the Compton telescope. The program is written in BASIC language for IBM 360 Call OS system.

06

A.2   Neutron Telescope

In omnidirectional detectors we do not measure the
direction of either the recoil proton or scattered neutron,
so that we do not know the direction of the incident neutron.
In order to determine the direction of the incident neutron
we can use two detectors spatially separated to measure the energy
of recoil proton, and the energy and direction of the scat-
tered neutron. From the kinematic relations both the energy
and direction of incident neutron can be obtained.

Suppose that one neutron detector is placed above the
other (Fig. A-1), and a neutron enters the first detector col-
liding with a proton so that the scattered neutron enters the
second detector where it scatters a second time. If we measure
the energy of the proton, $E_{p'}$, in the first detector and time
the flight of the scattered neutron n' between two detectors,
we can determine the direction of incidence of the incoming
neutron as well as the energy. We note that the time of flight
is related to the energy of scattered neutron n' by

$$E_{n'} = \frac{1}{2} M_n \left(\frac{S}{T}\right)^2$$ in the non-relativistic limit, where S is the

distance between two detectors, T is the time of flight.
The energy of the incident neutron is

$$E_n = E_{p'} + E_{n'}$$
$$= E_{p'} + \frac{1}{2} M_n \left(\frac{S}{T}\right)^2$$

Since,

$$E_{p'} = E_n \sin^2\theta$$

$$E_{n'} = E_n \cos^2\theta$$

so, $\theta = \tan^{-1} \sqrt{E_{p'}/E_{n'}}$

A.2.1 Efficiency Of The Neutron Telescope

The procedure to determine the efficiency of the neutron telescope is the same for neutrons as for γ-rays in the double Compton telescope mode. For a neutron beam with energy E_n and an incident angle θ, the efficiency of the system is

$$\varepsilon(E_n, \theta) = G_1 \cdot G_2 \cdot G_3 \cdot G_4 \cdot G_5$$

The six factors are defined as follows:

G_1 is the attenuation of the incident neutron flux by the ACD.

$$G_1 = \exp\left[- \frac{d_1}{\lambda_{H_1}(E_n)} - \frac{d_1}{\lambda_{C_1}(E_n)} \right]$$

G_2 is the probability for a neutron-proton scattering to occur in the first detector with the scattered neutron going into the solid angle subtended by the second detector.

$$G_2 = \frac{\frac{1}{\lambda_H(E_n)}}{\frac{1}{\lambda_H(E_n)} + \frac{1}{\lambda_C(E_n)}} \left\{ 1 - \exp\left[\frac{1}{\lambda_H(E_n)} - \frac{1}{\lambda_C(E_n)} \right] \right\} \cdot$$

$$\cdot \frac{\frac{d\sigma(E_n, \theta')}{d\Omega}}{\frac{1}{n_H \lambda_H(E_n)}} \Delta\Omega$$

G_3 is a step function which requires that the recoil proton in the first detector be greater than the threshold energy.

$$G_3 = H(E_{p_1} - E_{pth_1})$$

G_4 is the attenuation by the charged particle shields

when the scattered neutron passes from the first detector to
the second detector.

$$G_4 = \exp\ [-\frac{d_1 + d_2}{\lambda_{H_1}(E_n\prime)} - \frac{d_1 + d_2}{\lambda_{C_1}(E_n\prime)}]$$

G_5 is the probability for the scattered neutron $n\prime$ to
produce an observable event in the second detector.

$$G_5 = \{1 - \exp\ [- \frac{1}{\lambda_H^2(E_n\prime)} - \frac{1}{\lambda_C^2(E_n\prime)}\ ]\}\ \frac{1}{\frac{1}{\lambda_H(E_n\prime)} + \frac{1}{\lambda_C(E_n\prime)}}\ \cdot$$

$$\cdot\ [\ g_1\ \frac{1}{\lambda_H(E_n\prime)} + \sum_i g_i\ \frac{1}{\lambda_i(E_n\prime)}\ ]$$

The factor G_5 is very complicated and involved. Above 13.6
Mev protons can be produced through reactions $C^{12}(n,p)B^{12}$,
$C^{12}(n,np)B^{11}$ $\cdots$,etc. Furthermore the threshold energy of the
second detector E_{pth_2} is not set at zero. In order to evaluate
G_5 accurately, it is necessary to know the proton energy
distributions in these reactions. Otherwise, we are not
certain what fraction of the protons is below the threshold.
Also, in the second detector we do not restrict the observa-
tion of events which are only identified as protons. We may
include those events in which alpha particles and deuterons
are produced by the scattered neutron from the first detector.
If include this then G_5 will be modified to be

$$G_5 = \{1 - \exp\ [- \frac{1}{\lambda_H^2(E_n\prime)} - \frac{1}{C^2(E_n\prime)}\ ]\ \}\ \frac{1}{\frac{1}{\lambda_H(E_n\prime)} + \frac{1}{\lambda_C(E_n\prime)}}$$

$$\cdot\ [\ g_1\ \frac{1}{\lambda_H(E_n\prime)} + \sum_i g_i\ \frac{1}{\lambda_i(E_n\prime)} + \sum_j h_j\ \frac{1}{\lambda_j(E_n\prime)}\ ]$$

where,

d_1 : Thickness of ACD for first detector

d_2 : Thickness of ACD for second detector

l_1 : Effective length of first detector

l_2 : Effective length of second detector

$\lambda_H (E_n) = \dfrac{1}{n_H \sigma_H (E_n)}$: The mean free path of neutron-proton scattering in the detector for a neutron with energy E_n

$\lambda_C (E_n) = \dfrac{1}{n_C \sigma_C (E_n)}$: The mean free path of neutron-carbon scattering in the detector for a neutron with energy E_n

$\lambda_{H_1} (E_n) = \dfrac{1}{n_{H'} \sigma_H (E_n)}$: The mean free path of neutron-proton scattering in ACD for a neutron with energy E_n

$\lambda_{C_1} (E_n) = \dfrac{1}{n_{C'} \sigma_C (E_n)}$: The mean free path of neutron-carbon scattering in ACD for a neutron with energy E_n

$\Delta\Omega$: Solid angle subtended by the second detector

σ_H: The total cross section of neutron-proton scattering for a neutron with energy E_n

σ_C: The total cross section of neutron-carbon scattering for a neutron with energy E_n

n_H: The hydrogen density of detectors

n_C: The carbon density of detectors

$n_{H'}$: The hydrogen density of ACD

$n_{C'}$: The carbon density of ACD

$H(E_{p_1} - E_{pth_1})$: A step function

$\quad = 1 \qquad E_{p_1} \geq E_{pth_1}$

$\quad = 0 \qquad E_{p_1} < E_{pth_1}$

$$\frac{d\sigma\,(E_n,\theta')}{d\Omega}$$: The differential cross section of neutron-proton

scattering with incident neutron having energy E_n

and the scattering angle θ' in Lab. system

E_{p_1} : Energy of the recoil proton in the first detector

E_{pth_1} : The threshold energy of the first detector

E_{pth_2} : The threshold energy of the second detector

g_1 : The probability that in neutron-proton scattering

the recoil proton produces an observable event in

the second detector

g_i : The probability that in i_{th} type neutron-carbon inter-

action a proton is produced with energy $\geq E_{pth_2}$

λ_i : The mean free path of i_{th} type neutron-carbon inter-

action in which a proton is produced

h_j : The probability that in j_{th} type neutron-carbon inter-

action a charged particle or particles instead of a

proton are produced with energy losses that can

trigger the second detector

λ_j : The mean free path of j_{th} type neutron-carbon inter-

action in which charged particles rather than proton

are produced

For neutrons with energies below 15 Mev the neutron-

proton scattering dominates so G_5 may be approximated to be

$$G_5 \doteq \{1-\exp[-\frac{1}{\lambda_H(E_n')}-\frac{1}{\lambda_C(E_n')}]\}\frac{1}{\frac{1}{\lambda_H(E_n')}+\frac{1}{\lambda_C(E_n')}}[g_1\frac{1}{\lambda_H(E_n')}]$$

Now g_1 may be calculated in the following way.

The proton energy distribution can be described as

$$\frac{dN_p}{dE_p} = K \frac{1 + b \cos^2\theta}{1 + \frac{b}{3}}$$

where, $b = 2 (E_n/90)^2$

θ is the neutron scattering angle in the CM system

K is a constant [ChapterVII,(7-2)]

The scattering angle corresponding to E_{pth_2} is

$$\theta_1 = 2 \sin^{-1} \sqrt{E_{pth_2}/E_n}$$

and the scattering angle corresponding to $E_p = E_n$ is π.

The number of protons with energies between E_{pth_2} and E_n is

$$N_{\Delta E} = \int_{E_{pth_2}}^{E_n} \frac{dN_p}{dE_p} dE_p$$

$$= \int_{E_{pth_2}}^{E_n} \frac{dN_p}{dE_p} d(E_n \sin^2\frac{\theta}{2})$$

$$= \int_{\theta_1}^{\pi} K \frac{1 + b \cos^2\theta}{1 + \frac{b}{3}} E_n \sin\theta \, d\frac{\theta}{2}$$

The total number of protons with energies between 0 and E_n is

$$N_{total} = \int_0^{\pi} K \frac{1 + b \cos^2\theta}{1 + \frac{b}{3}} E_n \sin\theta \, d\frac{\theta}{2}$$

so that $g_1 = \frac{N_{\Delta E}}{N_{total}}$

$$= \frac{\int_{\theta_1}^{\pi} (1 + b \cos^2\theta) \sin\theta \, d\theta}{\int_0^{\pi} (1 + b \cos^2\theta) \sin\theta \, d\theta}$$

$$= \frac{(\cos\theta_1 + 1) + \frac{b}{3}(\cos^3\theta_1 + 1)}{2 + \frac{2}{3} b}$$

Using this approximation, the efficiency from this calculation of the neutron double scattering telescope is shown in Fig.A-10. The program to calculate the relations among energy of the neutron, incident angle and the efficiency of the system is in the following page.It is very interesting to observe in Fig. A-10 that the efficiency curves show the same kind of characteristics as for the gamma ray Compton telescope. There are two cutoff angles. The lower cutoff angle is due to the threshold of the first detector and the higher cutoff angle is due to the threshold of the second detector. The efficiency peaks at small angles for low neutron energies and peaks toward the larger angles at higher neutron energies. This occurs because the detection efficiency for the second detector is related to the energy of the scattered neutron. For a high energy incident neutron at a small incident angle θ' according to $E_{n'} = E_n \cos^2 \theta'$, the scattered neutron has almost the same energy as the incident neutron. The probability of detection in the second detector is relatively small compared with detecting a lower energy scattered neutron produced by same high energy neutron incident at a large angle in the first detector.

THE COMPUTER PROGRAM TO CALCULATE THE EFFICIENCY OF THE

NEUTRON TELESCOPE

This program gives the relation among the

neutron energy, incident angle and the efficiency of the neutron

telescope. The program is written in BASIC language for IBM

360 Call OS system.

```
320 DIM E(50),S(50)
330 REM THIS IS TO CALCULATE THE EFFICIENCY OF NEUTRON TELESCOPE
340 REM NE213 DENSITY OF HYDROGEN N5, CARBON N6
350 REM NE102 DENSITY OF HYDROGEN N3, CARBON, N4
360 N5=4.76E-2
370 N6=3.93E-2
380 N3=5.04E-2
390 N4=4.57E-2
400 REM THICKNESS OD THE AC DOME D1 IN CM
410 D1=1.588
420 REM LENGTH OD 2" L1, 5" L2
430 L1=4.648
440 L2=12.268
450 REM THE THRESHOLD OF 2" H1, 5" H2
460 H1=1.65
470 H2=4.42
480 REM TO READ IN THE CROSS SECTION OF N-C IN PAIR OF EN,SIGMA
490 FOR I=2 TO 23
500 READ E(I),S(I)
510 NEXT I
520 DATA .1,4.5,1,2.6,1.26,2.3,1.59,2.03,2,1.73,
525 DATA 2.51,1.56,3.16,1.9,3.98,2
530 DATA 5.01,1.25,6.31,1.05,7.94,1.09,10,1.15,12.6,1.28
535 DATA 15.9,1.43,20,1.45
540 DATA 25.1,1.4,31.6,1.23,39.8,1.05,50.1,.88,63.1,.72
545 DATA 79.4,.58,100,.47
550 PRINT "WHAT IS THE ENERGY OF THE NEUTRON?"
560 INPUT E1
565 B9=2*(E1/90)↑2
570 REM TO CALCULATE THE CROSS SECTION OF N-P, T1
580 C=E1
590 GO SUB 1010
600 REM TO CALCULATE THE CROSS SECTION OF N-C, T2
610 GO SUB 1070
620 REM TO CALCULATE THE ATTENUATION EFFECT OF THE DOME
```

```
630 G1=EXP(-D1*(N3*T1+N4*T2))
640 REM TO CALCULATE THE EFFICIENCY OF THE 1ST DETCTOR, G2
650 REM THE RATIO OF DIFFERENTIAL CROSS SECTION TO TOTAL CROSS
660 REM SECTION IN N-P IS F1
665 PRINT "NEUTRON ENERGY","ZENITH ANGLE","EFFICIENCY"
666 PRINT "MEV","DEGREE","PER CENT"
670 FOR A1=0 TO 90
680 A=A1*3.1416/180
690 REM THE ENERGY OF PROTON IS E3, NEUTRON E2
700 E2=E1*(COS(A))↑2
710 E3=E1-E2
720 IF E3<H1 THEN 940
730 IF E2<H2 THEN 940
740 F1=(1/4/3.1416)*((1+B9*(COS(2*A))↑2)/(1+B9/3))*4*COS(A)
750 REM THE SOLID ANGLE SUBTEND BY 2ND DETECTOR  IS ..076
760 G2=N5*T1/(N5*T1+N6*T2)*(1-EXP(-L1*(N5*T1+N6*T2)))*F1*.076
770 REM ATTENUATION OF THE SCATTERED NEUTRON BY AC DOME
780 REM TO GET THE NEW CROSS SECTION OF N-P AND N-C
790 C=E2
800 GO SUB 1010
810 GO SUB 1070
820 G4=EXP(-2*D1*(N3*T1+N4*T2))
830 REM TO CALCULATE THE PROB. FOR THE SCATTERED NEUTRON TO HAVE
840 REM AN EVENT OR IN OTHER WORDS IN N-P SCATTERING P HAS ENERGY
850 REM GREATER THAN THRESHOLD
860 A2=2*ASN(H2/E2)
870 F2=(COS(A2)+1+B1/3*((COS(A2))↑3+1))/(2+2/3*B1)
880 G5=(1-EXP(-L2*(N5*T1+N6*T2)))*F2*N5*T1/(N5*T1+N6*T2)
890 G6=G1*G2*G4*G5*100
900 PRINT E1,A1,G6
940 NEXT A1
1000 GO TO 550
1010 REM TO CALCULATE TOTAL CROSS SECTION OF N-P
1020 B1=2*(C/90)↑2
1030 C1=3*3.1416*(1.206*C+(-1.86+.09415*C+.0001306*C↑2)↑2)↑(-1)
1040 J1=3.1416*(1.206*C+(.4223+.13*C)↑2)↑(-1)
1050 T1=J1+C1
1060 RETURN
1070 I=2
1080 IF C<E(I) THEN 1150
1090 IF C>E(23) THEN 1150
1100 IF C>E(I) THEN 1130
1110 T2=S(I-1)+(C-E(I-1))/(E(I)-E(I-1))*(S(I)-S(I-1))
1120 GO TO 1170
1130 I=I+1
1140 GO TO 1100
1150 T2=0
1160 PRINT "CROSS SECTION OF N-C IS ZERO, CHECK!"
1170 RETURN
1180 END
```

APPENDIX B1

THE MONTE CARLO CALCULATION OF THE RESPONSE FUNCTIONS FOR

NE213 AS A GAMMA RAY DETECTOR

In our detectors pulse shape discrimination is
incorporated so that electrons produced by gamma rays are
separated from protons and alpha particles produced by neutrons.
Thus, from the flight matrix (Fig. 5-2, Fig. 5-3), the elec-
tron energy loss spectrum can be extracted. Since this elec-
tron energy loss sepctrum is related to the incident gamma
ray spectrum, it can be used to unfold the incident gamma ray
spectrum. To unfold the gamma ray spectrum we have to know
the response function of the detector. In the following
calculation we use the Monte Carlo technique to treat the
transport problem of gamma rays in the detector NE213. The
calculation includes the multiple scattering effect of a
gamma ray, the escape effect and self-gating effect of elec-
trons and positrons. Also the energy loss by the ionization
of the electron or the positron has been treated by the Landau
fluctuations.

B1.   THE MONTE CARLO CALCULATION FOR DETERMINING
GAMMA RAY RESPONSE FUNCTIONS

In this calculation we consider only Compton scatter-
ing and pair production because the energy range in which
we are interested is greater than 1 Mev. At 1 Mev the mean

free path λ for the photoelectric effect is about 10^6 cm whereas λ is 16.7 cm for Compton scattering. Obviously for our calculations the photoelectric effect is negligible.

We trace the gamma ray by the following steps:

1. For a gamma ray with energy E_γ we choose the incident direction and the position at which the gamma ray enters the detector. There are two choices:

a) We can specify the direction and position, or;

b) We can simulate random incidence by determining whether the gamma ray entered the detector from the top surface or the side. We do this by comparing $A1/A_T$ with Z, a random number between 0 and 1; if $Z>A1/A_T$ then the gamma ray entered from the side, otherwise it entered through the top surface (A1 and A2 are defined in Fig.B1 ; $A_T=A1+A2$).

a. Top Surface Case

The azimuthal angle of position vector $\vec{\gamma}$ is determined by $\phi=2\cdot3.1416\cdot Z$. The x, y and z coordinates are determined by: $x_0=R'\cos\phi$, $y_0=R'\sin\phi$, $z_0=0$, where $R'=R\sqrt{Z}$ and R: radius of the detector (Appendix D1). The direction cosines are then,

$\cos\theta_x = 1-2\cdot Z$

$\cos\theta_y = \pm\sqrt{Z[1-\cos^2\theta_x]}$

$\cos\theta_z = \sqrt{1-\cos^2\theta_y-\cos^2\theta_x}$

θ_x, θ_y and θ_z are the angles between the incident gamma ray and coordinates x, y and z respectively. The sign of $\cos\theta_y$ is determined by picking Z and comparing it with 0.5. If $Z>0.5$

††† In a step when a random number Z is needed a new random number is supplied.

then we take "+", otherwise "−".

b.   Side Surface Case

The positions are: $x_0 = R$, $y_0 = 0$, $z_0 = L \cdot Z$ where L is the length of the detector.

The direction cosines for the range of angles given by

$$90^\circ \leq \theta_x \leq 180^\circ$$
$$0^\circ \leq \theta_y \leq 180^\circ$$
$$0^\circ \leq \theta_z \leq 180^\circ$$

are

$$\cos\theta_y = \cos(\Pi \cdot Z)$$
$$\cos\theta_z = \sqrt{Z \cdot (1 - \cos^2\theta_y)}$$
$$\cos\theta_x = -\sqrt{1 - \cos^2\theta_y - \cos^2\theta_z}$$

We make $\cos\theta_z \geq 0$ because for symmetry $\cos\theta_z$ corresponds to $\cos(\Pi - \theta_z)$.

2.   To locate the event:

We calculate the mean free path λ and pick Z, then we assign $d = -\lambda \ln(Z)$ as the distance between the point when γ-ray entered and the place where the event occurs. The derivation of this relation is in Appendix B2.

3.   Does the event occur inside or outside the detector? The position of the event will be

$$x = d \cdot \cos\theta_x + x_0$$
$$y = d \cdot \cos\theta_y + y_0$$
$$z = d \cdot \cos\theta_z + z_0$$

If the conditions $|x| \leq R$, $|y| \leq R$ and $|z| \leq R$ are satisfied simultaneously, then this event occurred inside the detector. If not, this event is lost, and we go back to step (1) to pick a new γ-ray.

4. Was the resulting electron in the event produced by Compton scattering or pair production? If $(1/\lambda_p)/$ $(1/\lambda_p + 1/\lambda_{\bar{p}}) > Z$ then we have Compton scattering, otherwise the electron resulted from pair production.

5. If Compton scattering occurred, then we determine the direction and energy of the scattered γ-ray as follows: First, the energy and direction of the recoil electron are determined. Thus the energy deposited is found. The possibility of escape is included. We find the energy of the recoil electron from the probability distribution of the recoil electron: (Johns, 1952)

$$\frac{dS(E_e)}{dE_e} = \frac{\Pi \gamma_0^2}{\kappa E_\gamma} \left\{ 1 + \left[1 - \frac{2f'}{1 + 2\kappa - 2\kappa f'} \right]^2 + \frac{\kappa^2 \left[\frac{2f'}{1 + 2\kappa - 2\kappa f'} \right]^2}{1 + \kappa \frac{2f'}{1 + 2\kappa - 2\kappa f'}} \right\} \qquad E_e \leq E_{emax}$$

$$= 0 \qquad E_e > E_{emax}$$

and the normalized integrated probability:

$$S(E_e) = \frac{\int_0^{E_e} \frac{dS}{dE_e} dE_e}{\sigma_c^{KN}} = 2\Pi \gamma_0^2 \frac{1}{\sigma_c^{KN}} \left[b \cdot \left(\frac{bE_e}{2m_0 c^2} - \ell' \right) + \frac{\ell'}{2} + \frac{E_e}{m_0 c^2} \cdot \frac{f - \frac{\kappa E_e}{2m_0 c^2}}{2\kappa^4} \right]$$

If we pick Z and let $Z = S(E_e)$, then by solving this equation we are able to determine E_e (Appendix B2)

From
$$\cos \theta_\gamma = 1 - \left(\frac{E_\gamma}{E_\gamma - E_e} - 1 \right)/\kappa$$

$$\cos \theta_e = \sqrt{\frac{E_e (1+\kappa)^2}{E_e \kappa^2 + 2m_0 c^2 \kappa^2}}$$

we can calculate the angles of scattered γ-ray and the recoil

electron with respect to the incident γ-ray,

where,

m_0 = Rest mass of electron

c = Velocity of light

γ_0 = Radius of electron in cm^2

κ = E_γ/m_0c^2

b = $(1 + \kappa)/\kappa^2$

f = $\kappa/(\kappa-E_e/m_0c^2)$

f' = E_e / E_{emax}, E_{emax} is the maximum energy of Compton electron

ℓ' = $\ln(f)/\kappa$

a = $1 + 2\kappa$

$\sigma_c^{KN}= 2\Pi\gamma_0^2\{b[\frac{2(1+\kappa)}{a} - \frac{\ln(a)}{\kappa}] + \frac{\ln(a)}{2\kappa} - \frac{1+3\kappa}{a^2}\}$, total cross

section of Compton scattering (Hubbell, 1969)

In the coordinate system where the z axis is along the direction
of the incident γ-ray, we can assign the azimuthal angle of
electron ϕ_e to be $2\Pi\cdot Z$. In order to conserve momentum, the
incident γ-ray, scattered γ-ray and the recoil electron must
be in a plane, so $\phi_{\gamma'}=\phi_e+\Pi$, where $\phi_{\gamma'}$ is the azimuthal angle
of scattered γ-ray. If the recoil electron is energtic enough
to escape, then the energy deposited by the electron will be
less than the energy of the recoil electron. This escape
effect is handled in the following way.

Let t be the distance between the origin of the
Compton scattering and the boundary at which the electron
escapes when energetic enough. To determine t, we use the
following procedure. We consider two categories of escaping

electrons. The first electron is upward moving after scattering; the second is a downward moving escape electron.

(1) For the upward moving escape ($\cos\theta_z \leq 0$) the electron can escape through the top surface or the side. For escape through the top surface (Fig. B-2a):

$$\ell_t = \frac{0 - z}{\cos\theta_z} \quad ***$$

In the case of escape through sides (Fig. B-2b):

$$x_s = x + \ell_s \cos\theta_x$$

$$y_s = y + \ell_s \cos\theta_y$$

where x_s and y_s are coordinates of the point on the sides from which the electron escapes.

But, on the wall

$$R^2 = x_s{}^2 + y_s{}^2,$$

$$= \ell_s{}^2(\cos^2\theta_x + \cos^2\theta_y) + \ell_s(2x\cdot\cos\theta_x + 2y\cdot\cos\theta_y) + x^2 + y^2$$

$$K_1 \ell_s{}^2 + K_2 \ell_s + K_3 = 0$$

where,

$$K_1 = \cos^2\theta_x + \cos^2\theta_y$$

$$K_2 = 2x\cdot\cos\theta_x + 2y\cdot\cos\theta_y$$

$$K_3 = x^2 + y^2 - R^2$$

$$\ell_s = \frac{-K_2 + \sqrt{K_2{}^2 - 4K_1\cdot K_3}}{2K_1} \quad \text{(A)}$$

*** When $\cos\theta_z = 0$ we let $\ell_t = 10^7$, instead of calculating ℓ_t by this equation.

We have discarded the negative root of ℓ_s because it is not allowed.

We compare ℓ_t and ℓ_s and choose the smaller one as t.

(2) For downward moving escape electrons ($\cos\theta_z > 0$), we have escape through the bottom or the sides (Fig. B-2c,b). For escape through the bottom,

$$\ell_b = \frac{L - z}{\cos\theta_z}$$

In the case of escape through sides

ℓ_s is calculated by (A)

We compare ℓ_b and ℓ_s and choose the smaller one as t.

If t is approximated to be the effective thickness of the detector for the electron then the energy deposited by the ionization in the detector (NE213) is calculated by Landau fluctuations (Appendix B2)

$$dE_i = \left(\frac{7.28 \cdot 10^{-2} t}{1 - A^2} \right) \cdot [\lambda' + \ln(t) - 2 \cdot \ln(A) + A^2 + 15.293]$$

where,

$$A = \left(\frac{m_0 c^2}{m_0 c^2 + E_e} \right)$$

and λ' is a parameter of Landau probability curve, which is a universal function. The technique developed to choose λ' by the Monte Carlo technique is discussed in Appendix B2.

The energy loss by the Bremsstrahlung is also calculated but the secondary photons from Bremsstrahlung are not traced so no energy is deposited by Bremsstrahlung in our treatment. To calculate the energy loss dE_b in the process of Bremsstrahlung we divide electrons into two categories (Evans, 1955).

(1) $E_e \leq 38$ Mev

$$dE_b = 3.39 \cdot 10^{-3} [(E_e + 0.51) \cdot (-1/3 + \ln(2/A)] \cdot t$$

(2) $E_e > 38$ Mev

$$dE_b = 1.59 \cdot 10^{-2} (E_e + 0.51) \cdot t$$

If $dE_i + dE_b \geq E_e$, then the electron stops in the detector and the energy deposited is dE_i only.

If the electron is energetic enough, it is possible to escape from the detector and gate the detector off. Consequently, we miss this event. To take care of this self-gating effect we calculate the energy of the electron after it escaped from the detector and subtract the energy loss when it passes through the aluminum can of thickness 0.16 cm which surrounds the detector. The energy left is assumed to be the energy deposited in the ACD; this is not true if the electrons do not stop in the ACD, but what really matters is the energy deoposited in the ACD is greater or less than the threshold of the ACD, hence, the assumption introduces no error.

The energy loss dE_{Al} in the aluminum can is calculated by the following method. The energy-range relation is (Price, 1971)

$$R_g = 412 \, E_e^{1.265-0.0945 \, \ln(E_e)} \quad mg/cm^2 \quad o.01Mev \leq E_e < 3Mev$$

$$R_g = 530 \, E_e - 106 \quad\quad\quad mg/cm^2 \quad\quad 3Mev \leq E_e \leq 14Mev$$

We also assume that the second relation is valid for energies above 14 Mev.

$$dE_{Al} = \left(\frac{E_e - dE_i - dE_b}{R_g} \right) \times 2700 \times 0.16 \, Mev,$$

where the density of the aluminum is taken to be 2.7 g/cc. The energy deposit dE_{ACD} in the ACD is

$$dE_{ACD} = E_e - dE_i - dE_b - dE_{Al}.$$

The scattered γ-ray in Compton scattering is traced from step 2.

6. If the γ-ray interaction is by pair production, then we determine the energy, direction and energy deposited by the electron and also these same three quantities for the positron. The total energy deposited will be the sum of the energy deposited by the electron and the positron. The electron energy distribution is flat between 0 and $E_\gamma - 2 \, m_0 c^2$. We pick Z and let $E_e = Z \times (E_\gamma - 2 \, m_0 c^2)$ so the energy of the positron is $E_e+ = E_\gamma - 2 \, m_0 c^2 - E_e$. In the case that $E_\gamma >> m_0 c^2$, the angle between the electron and the incident γ-ray is $\frac{m_0 c^2}{E_\gamma}$. We assume that this relation is valid for both the positron and electron in the low energy range. In the coordinate system where the

z axis is along the direction of the incident γ-ray, we take the azimuthal angle of the electron as $\phi_e = 2\Pi \times Z$ and $\phi_{e^+} = \Pi + \phi_e$ for the positron. After the energies and directions of the electron and positron have been determined, we use the method in (5) to determine the energy deposit of this event.

7. For each incident γ-ray, we add the energy deposited by Compton scattering(s) and (or) by pair production. This total energy deposit is proportional to the light output of this event.

8. For each incident γ-ray, we also accumulate the energy deposit in the ACD for each electron (and positron). If the total energy deposit in the ACD is greater than the threshold of the ACD, 1 Mev, then we consider this event is a self-gating event.

9. We then convert the energy into pulse height for our pulse-height-analyzer (PHA) using the total light output in 7. Each calculated γ-ray interaction will then produce an event in a particular channel of our 128-channel PHA if the electron energy is in the energy range covered by the PHA.

10. Using this technique, we can simulate 10,000 γ-rays for each energy, and obtain a pulse height distribution. We call this pulse height distribution the response function for this energy.

From step 1 to step 10 the program is complete but in some cases we like to simulate the actual resolution of the detector because the fore-mentioned procedure yields the response function based on perfect resolution. To simulate the resolution we use the following approach.

Let the energy deposited by an electron to produce an unit light pulse in the detector be L_0 Mev, this L_0 is used as the resolution parameter. If we observe an event which has a light pulse with amplitude L Mev then this light pulse is composed of L/L_0 unit light pulses. But the real energy deposited may not be equal to $L/L_0 \cdot L_0$ because the photon is quantized so if the energy deposited is greater than $L/L_0 \cdot L_0$ but less than $L/L_0 \cdot L_0 + L_0$, there are still L/L_0 unit light pulses. So we may take the average and say that the energy deposited corresponds to $L/L_0 + 0.5$ light pulses. The statistical uncertainty for N pulses is $\sqrt{N}$ so we take the standard deviation to be $\sqrt{L/L_0 + 0.5} \cdot L_0$ for a light pulse with amplitude L Mev. A subroutine, which picks 12 random numbers and adds -6, has been tested to be good enough to simulate a Gaussian distribution with standard deviation equal to 1. From this subroutine we obtain a value G which corresponds to a certain point on the Gaussian curve with standard deviation 1, then $G \cdot \sqrt{L/L_0 + 0.5} \cdot L_0$ is taken to be the deviation from L. In this way the energy deposited of every event is calculated by $E = E_d + G \cdot \sqrt{E_d/L_0 + 0.5} \cdot L_0$. This method is used by Stanton (1971); E_d is the energy deposited and E is the energy observed. In our opinion the resolution effect can be treated

by a simpler method. Suppose the energy deposited is E_d, then there will be $Int(E_d/L_0)$ unit light pulses, where $Int(\ )$ means to take the integer of the value inside the brackets. The standard deviation is $\sqrt{Int(E_d/L_0)}$ so the deviation from E_d is $\sqrt{Int(E_d/L_0)} \cdot L_0 \cdot G$.

These two methods yield similar results because in our case usually the term E_d/L_0 is much larger than 0.5.

So, if the resolution effect is considered, after we obtain the energy deposited in step 7, it is necessary for us to go through the procedure just described before the calculation proceeds to step 9.

APPENDIX B2

PRINCIPLE OF MONTE CARLO METHOD

Suppose we have a distribution $F(x)$ with $x_1 \leq x \leq x_2$ and we want to pick x randomly but weighted by $F(x)$. What should we do?

We may transform $F(x)$ from x plane to t plane, in t plane $0 \leq t \leq 1$, such that in t plane every value of t is equally probable, in other words, $F(t)=1$. In doing so we have to satisfy the relation

$$\frac{F(t)dt}{\int_0^1 F(t)dt} = \frac{F(x)\,dx}{\int_{x_1}^{x_2} F(x)\,dx}$$

Since we make $F(t)=1$ then the relation becomes

$$dt = \frac{F(x)\,dx}{\int_{x_1}^{x_2} F(x)\,dx}$$, and if we integrate both sides,

$$\int_0^Z dt = \frac{\int_{x_1}^{x} F(x)\,dx}{\int_{x_1}^{x_2} F(x)\,dx} \quad => \quad Z = \frac{\int_{x_1}^{x} F(x)\,dx}{\int_{x_1}^{x_2} F(x)\,dx}$$

So, if we pick Z with $0 \leq Z \leq 1$ we always can use above equation to find the corresponding x which is weighted by $F(x)$.

Example 1: For a γ-ray with mean free path λ in the detector, what is the distance it travels before an event

occurs?

The probability that a γ-ray can travel a distance ℓ and have an interaction between ℓ and ℓ+dℓ is

$-\frac{1}{\lambda}\exp(-\ell/\lambda)\,d\ell$. So, in this case the distribution function is $F(\ell)=-\frac{1}{\lambda}\exp(-\ell/\lambda)$.

$$Z'=\frac{\int_0^\ell \frac{-1}{\lambda}\exp(-\ell'/\lambda)\,d\ell'}{\int_0^\infty \frac{-1}{\lambda}\exp(-\ell'/\lambda)\,d\ell'}$$

$$=1-\exp(-\ell/\lambda)$$

$$\ell=-\lambda\,\ln(1-Z')$$

Since Z´ is a random number between 0 and 1, 1-Z´ will be a random number between 0 and 1, too. Let Z=1-Z´,

$$\ell=-\lambda\,\ln Z$$

Example 2: In xy plane the distribution in azimuthal angle is uniform. How to simulate the angular distribution?

Since the distribution is uniform, $F(\phi)=1$ and

$$Z=\frac{\int_0^\phi d\phi}{\int_0^{2\pi} d\phi}=\frac{\phi}{2\pi}\qquad so,\quad \phi=2\Pi\times Z$$

Example 3: In Compton scattering, how do we determine the energy of the recoil electron?

The electron distribution is $\frac{dS(E_e)}{dE_e}$ (Appendix B1)

$$Z=\frac{\int_0^{E_e}\frac{dS(E_e)}{dE_e}\,dE_e}{\int_0^{E_{emax}}\frac{dS(E_e)}{dE_e}\,dE_e}$$, where E_{emax} is the maximum

electron energy in the Compton scattering.

Let $F = Z - \dfrac{A(1-\cos\theta) + B\left(\dfrac{\theta}{2} - \dfrac{1}{4}\sin 2\theta\right)}{A + B\dfrac{\Pi}{4}}$

$\dfrac{dF}{d\theta} = -\dfrac{A\sin\theta + B\left(\dfrac{1}{2} - \dfrac{1}{2}\cos 2\theta\right)}{A + B\dfrac{\Pi}{4}}$

First, if we let θ be an arbitrary angle between 0 and $\dfrac{\Pi}{2}$, and $|F| > \varepsilon$, then put $\theta = \theta - \dfrac{F}{\dfrac{dF}{d\theta}}$ and use this θ to calculate F again. Repeat this procedure until $|F| < \varepsilon$. Thus, we find θ, the zenith angle of the neutron. But since the upper and the lower hemisphere are symmetrical with respect to $\dfrac{\Pi}{2}$, an equally probable answer is $\Pi - \theta$. We may pick Z' and let the zenith angle equal θ, if $Z' > 0.5$, otherwise the zenith angle equal $\Pi - \theta$.

Example 5: What is the energy loss by ionization of an electron with energy E_e passing through NE213 of thickness ℓ?

The probability distribution of Landau fluctuations is $f(\ell, dE_i) = \dfrac{1}{k} F(\lambda)$, (Landau, 1944), where k is a constant with respect to a certain energy of the incident electron and the type and thickness of the detector.

$Z = \dfrac{\int_{\lambda_1}^{\lambda} F(\lambda)\, d\lambda}{\int_{\lambda_1}^{\lambda_2} F(\lambda)\, d\lambda}$

where λ_1 and λ_2 are the lower and upper limits of the probability distribution parameter λ. Because λ from -2 to

14 includes most of probability destribution we let $\lambda_1 = -2$ and $\lambda_2 = 14$. Since $F(\lambda)$ is known to be difficult to integrate, we divide $F(\lambda)$ into 17 groups, i.e., $\lambda = -2$ to $\lambda = -1$, $\lambda = -1$ to $\lambda = 0$....$\lambda = 13$ to $\lambda = 14$. The probability in each group is

0.088, 0.198, 0.220, 0.132, 0.077,

0.066, 0.044, 0.033, 0.033, 0.022,

0.022, 0.011, 0.011, 0.011, 0.011,

0.011, 0.011, and we have normalized the probability from $\lambda = -2$ to $\lambda = 14$ to be 1.

To determine λ, we pick a random number Z and calculate Z-0.088, where 0.088 is the probability for λ to be in the first group. If it is greater than zero, then we know λ is not in the first group. Next we calculate Z-0.088-0.198 and see if it is greater than zero. If so, we subtract the probability of the next group. We keep doing thid until we find negative value or zero. At this step we know λ belongs to which group, say, group 10, and the value of λ is between 7 and 8, so we pick a new random number Z' and let $\lambda = 7 + Z'$, in this step we assume that the probability for λ to be any value between 7 to 8 is the same.

After λ is found, the energy loss by ionization in NE213 with thickness ℓ is calculated by

$$dE_i = \left(\frac{7.28 \times 10^{-2} \ell}{1 + A^2} \right) (\lambda + \ln\ell - 2 \ln A + A^2 + 15.293)$$

where $A = \dfrac{m_0 c^2}{m_0 c^2 + E_e}$

$$Z = \frac{S(E_e)}{\sigma_c^{KN}} \qquad (B-1)$$

So, we have to solve for E_e from equation (B-1) after we pick a random number Z. Let $F = Z - S(E_e)/\sigma_c^{KN} \cdots$ (B-2), then we have to find E_e such that F=0. The Newton's iteration method may be used to solve this equation. Let us assume that $E_e = k$, where k is an arbitrary number and put $E_e = k$ into (B-2) to see if $|F| < \varepsilon$ where ε is a small number assigned by us. If $|F| > \varepsilon$ then let $E_e = E_e - \dfrac{F}{\dfrac{dF}{dE_e}}$ and substitude this E_e into (B-2)

We repeat this refinement until we get the E_e that will make $|F| < \varepsilon$. This value of E_e is the energy of the recoil electron.

Example 4: If the neutron distribution at balloon altitude is $\dfrac{dF}{d\Omega} = A + B |\sin\theta|$, how do we use the Monte Carlo method to simulate this kind of distribution? θ here is the zenith angle.

$$Z = \frac{\int_0^{2\pi} \int_0^{\theta} (A+B\sin\theta)\sin\theta \, d\phi \, d\theta}{\int_0^{2\pi} \int_0^{\frac{\pi}{2}} (A+B\sin\theta)\sin\theta \, d\phi \, d\theta}$$

At this moment, we let θ range from 0 to $\frac{\pi}{2}$ because the upper hemisphere is symmetrical with respect to the lower hemisphere,

$$Z = \frac{A(1-\cos\theta) + B(\frac{\theta}{2} - \frac{1}{4}\sin 2\theta)}{A + B\frac{\pi}{4}}$$

Again we use Newton's iteration method to solve for θ.

Example 6: If neutrons are randomly incident on the
top of the detector with radius R, how to determine the
distance between the center of the detector and the place
where a neutron entered?

The probability for a neutron to fall within a
distance $\gamma \leftrightarrow \gamma + d\gamma$ from the center of the top surface is
proportional to the area of the band surrounded by γ and
$\gamma + d\gamma$,

$$\Delta P(\gamma) \propto \int_0^{2\pi} d\phi \int_0^{R'} \gamma \, d\gamma$$

$$Z = \frac{\int_0^{2\pi} d\phi \int_0^{R'} \gamma \, d\gamma}{\int_0^{2\pi} d\phi \int_0^{R} \gamma \, d\gamma} = \frac{R'^2}{R^2}$$

$$R' = R \sqrt{Z}$$

APPENDIX C

CONTAMINATION OF LOCAL NEUTRONS AND EXTERNAL PROTONS

The detector system was surrounded by a gondola made of aluminum with a diameter of 71.1 cm, length 274.3 cm and thickness 0.16 cm. At the bottom of the gondola there were PHA assemblies (2.3 kg), electronics (9.1 kg) and batteries (50 kg). Under the gondola there were a supporter (1.5 kg), crush pad, hopper and ballast (145.6 kg, total). The NCAR instruments (294.8 kg) were split into two packages and attached on the two sides of bottom frame of the gondola. The total mass of the payload amounted to 503 kg.

During the experiment, the position of the detectors was changed three times. By observing the spectrum and intensity changes in the different positions due to the different distances from the local production sources, the effect of local production could be determined. For the 5 inch detector there were two major local production sources: the 2 inch detector with its ACD and the larger mass in the lower part of the gondola. An estimate of the relative strength of two effects was made in the following way. Since the local production is related to the mass, M, of the source and the solid angle, Ω, which the source subtended at the detector, the contribution would be proportional to M x Ω.

Taking the bottom area of the gondola as the local production source area (3973 cm^2), the solid angle subtended

by the 5 inch detector was 0.062, 0.073 and 0.087 for the three positions. Thus, $A \times \Omega$ was 31, 37 and 44 kg-ster. for the detector locations of 252, 233 and 214 cm respectively from the bottom of the gondola.

The mass of the 2 inch detector was 0.035 kg and its ACD was 2.75 kg giving a total mass of 2.79 kg. The area of the 2 inch detector and its ACD seen by the 5 inch detector was about 349 cm^2. The distance between two detectors was 50, 28 and 50 cm so the solid angle was 0.14, 0.45 and 0.14 ster. and $A \times \Omega$ was 0.4, 1.2 and 0.4 kg-ster. respectively.

Comparing the relative contributions of these two effects, it is clear that the significant local production would be from the material at the bottom of the gondola.

In Fig.C-1, proton recoil spectra corresponding to three positions are shown. Given the statistical fluctuations observed, there is no significant difference.

We have also estimated the local production rate of neutrons by the method of Boella et al (1965). The local neutron produced by a nucleonic flux, isotropic over a solid angle 2Π on a sphere of material of mass M is given by

$$n = 2\Pi \, \phi (M/\lambda) \, \nu \qquad neutrons/sec$$

where, ϕ : cosmic ray flux   particles/cm^2 -sec-ster.

λ : average interaction length

ν : average number of neutrons per interaction

M : mass   gram

From their calculation at solar minimum activity at 4.6 GV

geomagnetic cutoff, $n = 9 \times 10^{-3}$ for paraffin, 8×10^{-3} for aluminum and 14×10^{-3} neutrons/g-sec for nickel-cadmium. We approximately divide the local production sources into three parts and make these assumptions:

1. Batteries => 50 kg nickel-cadmium, 214 cm away from the detector (5 inch)

2. All instruments => 403 kg aluminum, 214 cm away from the detector (5 inch)

3. 2 inch detector system => 2.79 kg paraffin, 50 cm away from the detector (5 inch)

The contribution from 1.) is 1.2×10^{-3}; from 2.) is 5.6×10^{-3} and from 3.) is 0.8×10^{-3} neutrons/cm^2 -sec. The total local neutron production is then 7.6×10^{-3} neutrons/cm^2-sec. The measured neutron flux at atmospheric depths 4.2 g/cm^2 to 2.9 g/cm^2 is between 0.33 to 0.59 neutrons/cm^2 -sec so that the local production effect in the 5 inch detector is about 2%. Similarily we have estimated the neutron local production effect to be 3% for the 2 inch detector.

We conclude that the local production effect in the system did not make significant contribution to the proton spectra we observed.

For the 2 inch detector, the threshold energy of the
ACD was set above the energy deposited by the minimum
ionizing muons in the ACD. Therefore, the ACD did not veto
all external charged particles. We estimated the contamina-
tion of the proton recoil spectrum by the external real
protons in the following way. After the dead time corrections,
at float altitudes for a period of 17400 seconds, the number
of the external protons detected by the 5 inch detector was
864.3 protons/cm^2. The number of external protons detected
by the 2 inch detector was 832 protons/cm^2, but the number
above the threshold of the 5 inch detector was 804.1 protons/
cm^2. The proton leakage was (864.3-804.1)/864.3=7%. So, for
the 2 inch detector the number of the real protons which con-
taminated the proton recoil spectrum, induced by neutrons,
was $832 \times \dfrac{100\%}{(100\%-7\%)} \times 7\% = 62.6$ protons/cm^2. In the 2 inch detec-
tor, the total number of the recoil protons induced by neutrons
was 1441.5 protons/cm^2, so the contamination by the external
protons was about 4%. Compared with the uncertainty of the
deduced neutron spectrum, this 4% uncertainty is not signifi-
cant, so we made no correction on this effect.

FIGURE CAPTIONS

5-1 SCHEMATIC DRAWING OF THE DETECTION SYSTEM

5-2 THREE DIMENSIONAL DISPLAY OF THE FLIGHT DATA, OBTAINED
IN THE EARLIER PORTION OF THE FLIGHT (1033.77 g/cm^2-
4.22 g/cm^2) FOR A PERIOD OF 8625 SECONDS, OF THE 2
INCH DETECTOR
The z scale is a logarithmic scale. The band marked e
is the electron recoil band, P is the proton recoil
band, α is the alpha particle vand, and IFC is the in-
flight-calibrator.

5-3 THREE DIMENSIONAL DISPLAY OF THE FLIGHT DATA, OBTAINED
IN THE EARLIER PORTION OF THE FLIGHT (1033.77 g/cm^2-
4.22 g/cm^2) FOR A PERIOD OF 8625 SECONDS, OF THE 5
INCH DETECTOR
The band marked e is the electron recoil band, P is the
proton recoil band, and α is the alpha particle band.
The IFC band is out of scale. The z scale is a loga-
rithmic scale.

5-4 THREE DIMENSIONAL DISPLAY OF THE DATA OF THE 2 INCH
DETECTOR AT E_n=27.4 Mev (Run 28) FROM THE MSU CALIBRA-
TIONS
The band marked e is the electron band, P is the proton
band with protons from n-p scattering, pB is the proton
band with protons from the reaction $C^{12}(n,p)B^{12}$, and
α is the alpha particle band. The z scale is a loga-
rithmic scale

5-5 THREE DIMENSIONAL PLOT OF THE DATA OF THE 5 INCH
DETECTOR AT E_n=70.6 Mev (Run 12) FROM THE MSU CALIBRA-
TION
The band marked e is the electron band, P is the proton
band, and α is the alpha particle band.

7-1 THE RELATION BETWEEN THE PROTON ENERGY AND THE CHANNEL
NUMBER OF THE FLIGHT PULSE-HEIGHT PHA OF THE 5 INCH
DETECTOR

7-2 THE RELATION BETWEEN THE PROTON ENERGY AND THE CHANNEL
NUMBER OF THE FLIGHT PULSE HEIGHT PHA OF THE 2 INCH
DETECTOR

7-3 RESPONSE FUNCTIONS OF THE 5 INCH DETECTOR AT NEUTRON
ENERGIES 4.9 Mev AND 9.96 Mev FROM THE MSU CALIBRATIONS
The response functions have been normalized to 10,000
incident neutrons.

7-4 RESPONSE FUNCTIONS OF THE 5 INCH DETECTOR AT NEUTRON
ENERGIES 14.5 Mev, 19.9 Mev, 27.7 Mev, AND 39.4 Mev
FROM THE MSU CALIBRATIONS

7-15 THE 'Q' VALUE OF THE REACTION $C^{12}(n,p)B^{12}$
    The 'Q' value here is defined to be the energy difference
    between the incident neutron energy and the central
    energy of the Gaussian bump. There is a tendency that the
    'Q' value is not a constant. This suggests that the
    energy distribution of the protons is changing with the
    energy of the incident neutrons or the B^{12} nucleus is
    excited at high neutron energies.

7-16 THE THEORETICAL PROTON RECOIL SPECTRA FROM n-p SCATTERING
    FOR Run 10; WITH AND WITHOUT FINITE RESOLUTION EFFECT
    (a) The proton recoil spectrum from n-p scattering is calcu-
    lated under the following conditions. 1. The incident
    neutrons have energies from 71.6 Mev to 78 Mev, and the
    relative intensity is $Y(E_n)=1.1+(E_n-78)\times0.1$. 2. The
    resolution of the 5 inch detector is perfect.
    (b) The theoretical proton spectrum from n-p scattering is
    obtained under the same condition of (a), but the resolution
    parameter of the 5 inch detector is assumed to be 0.3 Mev
    such that the spectrum above 70 Mev matches the observed
    response function of 74.3 Mev.

7-17 THE THEORETICAL PROTON RECOIL SPECTRA FROM n-p SCATTERING
    OF THE 5 INCH DETECTOR AT E_n=74.3 Mev; WITH AND WITHOUT
    THE FINITE RESOLUTION EFFECT
    (a) perfect resolution
    (b) The resolution parameter is 1 Mev electron energy

9-1 THE PROTON RECOIL SPECTRUM OF 5 INCH DETECTOR FROM THE
    PALESTINE BALLOON FLIGHT ON JUNE 22, 1973
    To obtain the differential energy spectrum it is necessary
    to divide the value by the flight time 17400 seconds
    and the area of the 5 inch detector.

9-2 THE PROTON RECOIL SPECTRUM OF THE 2 INCH DETECTOR FROM
    THE PALESTINE BALLOON FLIGHT ON JUNE 22, 1973
    To obtain the differential energy spectrum it is necessary
    to divide the value by the flight time 17400 seconds and
    the area of the detector.

9-3 RELATIONS BETWEEN STRUCTURES ON THE RESPONSE FUNCTIONS
    OF THE 5 INCH DETECTOR FOR NEUTRONS WITH ENERGIES
    GREATER THAN 48.5 Mev
    All intensities of the structures are relative to the
    intensity of the plateau on the response function.
    (a) the ratio of the broad bump at the lower energy side of
    the response function to the plateau
    (b) the ratio of the Gaussian bump to the plateau
    (c) the ratio of the base between the Gaussian bump and the
    broad bump to the plateau

9-4 THE RELATION BETWEEN THE ENERGY OF INCIDENT NEUTRONS
    AND THE CENTRAL ENERGY OF THE BROAD BUMP AT LOW ENERGY

SIDE OF THE RESPONSE FUNCTION OF THE 5 INCH DETECTOR

conditions,
1. The separation of the two detectors is 50 cm.
2. The threshold of the first detector (2 inch detector) is 0.066 Mev electron energy.
3. The threshold of the second detector (5 inch detector) is 0.7 Mev electron energy.

A-6   THE RELATION AMONG THE TRUE ENERGY, THE INCIDENT ANGLE OF A GAMMA RAY, AND THE POSSIBLE MEASUREMENTS FROM THE COMPTON TELESCOPE
The threshold of the first detector is 0.066 Mev, and the second detector is 0.7 Mev.

A-7   THE RELATION AMONG THE TRUE ENERGY, THE INCIDENT ANGLE OF A GAMMA RAY, AND THE POSSIBLE MEASUREMENTS FROM A COMPTON TELESCOPE
The threshold energy of the first detector is 0.066 Mev

A-8   THE UNCERTAINTIES IN THE ENERGY AND THE INCIDENT ANGLE OF THE GAMMA RAYS MEASURED BY A COMPTON TELESCOPE
In a Compton telescope if the energy of the electron measured in the first detector is 1 Mev±0.2 Mev and the energy of the electron measured in the second detector is 3 Mev±0.3 Mev, the experimental error region (EER) is represented by the area surrounded by ABDC. A band confined by the dashed lines is the Accepted Zone, in which any point is a possible solution for the measurements. The corresponding points of A, B, C, and D are A´, B´, C´, and D´. These four points are determined by the assumption that the electron in the second detector is produced by the gamma ray which has a 50% probability to produce an electron with energy higher than the energy of the electron observed in the second detector. According to the convention we used in the Appendix A, the area surrounded by A´B´ABDCD´C´ represents the uncertainty of the measurements.

A-9   USING A COMPTON TELESCOPE TO MEASURE A GAMMA RAY WITH ENERGY 5 Mev AND THE INCIDENT ANGLE 10 DEGREE; THE POSSIBLE MEASUREMENTS AND THEIR RELATIVE PROBABILITIES

A-10 EFFICIENCY OF A NEUTRON TELESCOPE
The efficiency of a neutron telescope as a function of the neutron energy and the zenith angle
The magnitude of a radial vector represents the efficiency of the system. θ is the incident angle. In our case we put the system in the configuration such that the central line of the two detectors points toward the zenith. The efficiency is calculated under the following conditions,
1. The separation of the two detectors is 50 cm.
2. The threshold of the first detector (2 inch detector) is 1.65 Mev proton energy.
3. The threshold of the second detector (5 inch detec-

tor) is 4.42 Mev proton energy.

B-1   THE TOP AND THE SIDE VIEW OF THE CYLINDRICAL DETECTOR
      The radius of the detector is R and the length is L.
      A1 is the effective area of the top view.
      A2 is the effective area of the side view.

B-2   THE EFFECTIVE THICKNESS FOR A CHARGED PARTICLE
      If a charged particle is produced in the detector at
      the position (x,y,z), and it is energetic enough to
      escape from the detector, then in the case that the path
      length is straight the effective thickness of the de-
      tector with respect to the charged particle will be
      ℓ_t, if it escapes through top, ℓ_s, through side, and ℓ_b,
      through bottom.

B-3   COMPARISON OF GAMMA RAY RESPONSE FUNCTIONS FROM THE
      CALIBRATIONS AND THE MONTE CARLO CALCULATION
      The calibrated response function belongs to Co^{60} radio-
      isotope source calibration. This source has two gamma
      ray lines, 1.33 Mev and 1.17 Mev. The Monte Carlo
      calculation is carried out by the computer program
      developed in this laboratory (Appendix B1). In the
      calculation each incident gamma ray is assumed to be
      moving along the axis of th detector, and incident on
      the top of the 2 inch detector. In the calculation 50%
      of gamma rays have energy 1.33 Mev and the rest have
      energy 1.17 Mev. The resolution parameter is taken to
      be 0.013 Mev.

C-1   PROTON RECOIL SPECTRA OF THE 5 INCH DETECTOR AT THREE
      DIFFERENT POSITIONS DURING PALESTINE FLIGHT ON JUNE 22,
      1973
      In the down flux mode, the distance from the 5 inch de-
      tector to the 2 inch detector was 50 cm; to the bottom
      of the gondola was 214 cm. In the up flux mode the
      destance from the 5 inch detector to the 2 inch detector
      was 50 cm; to the bottom of the gondola was 252 cm. In
      the horizontal flux mode, the distance from the 5 inch
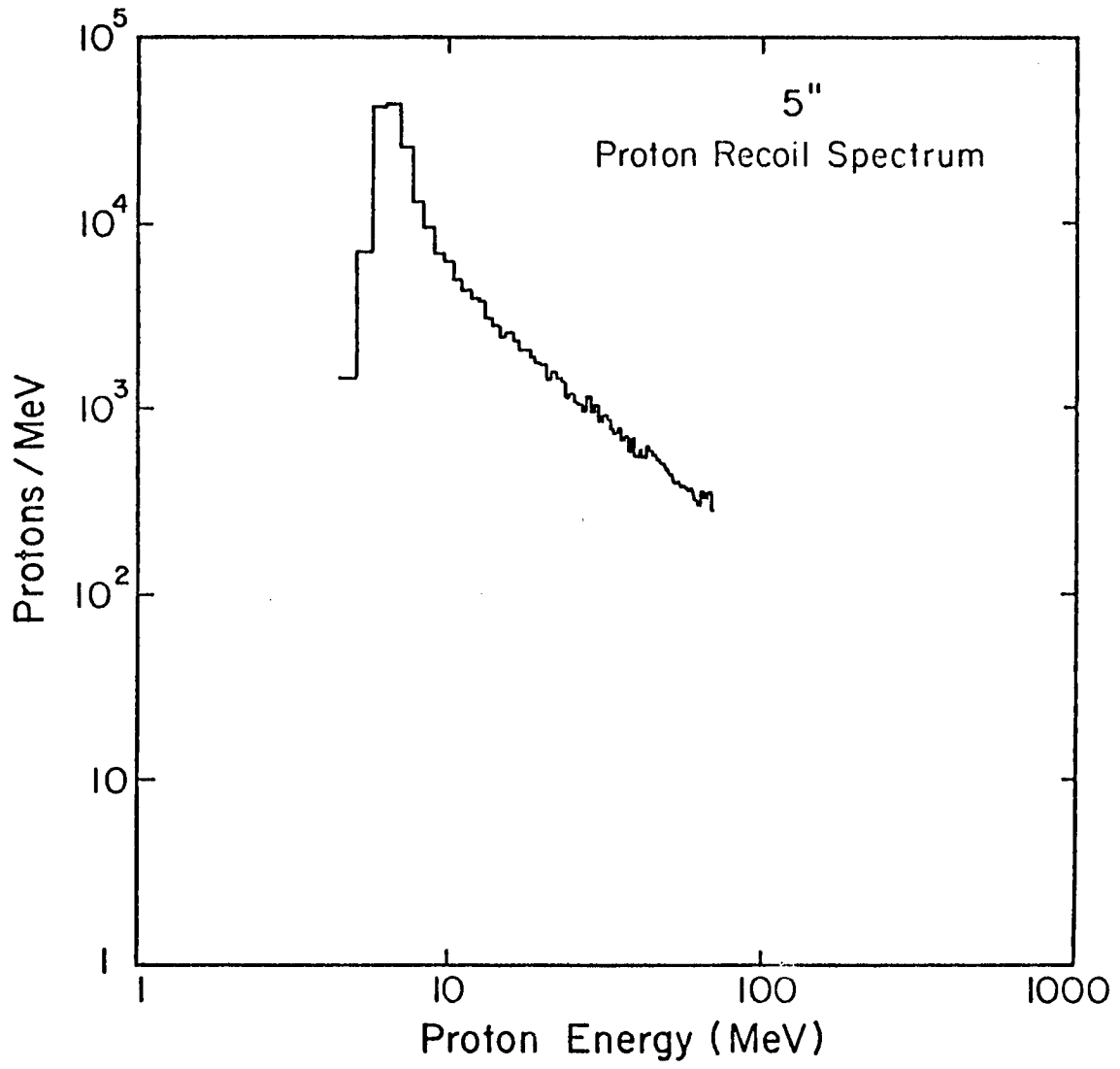   detector to the 2 inch detector was 28 cm; to the bottom
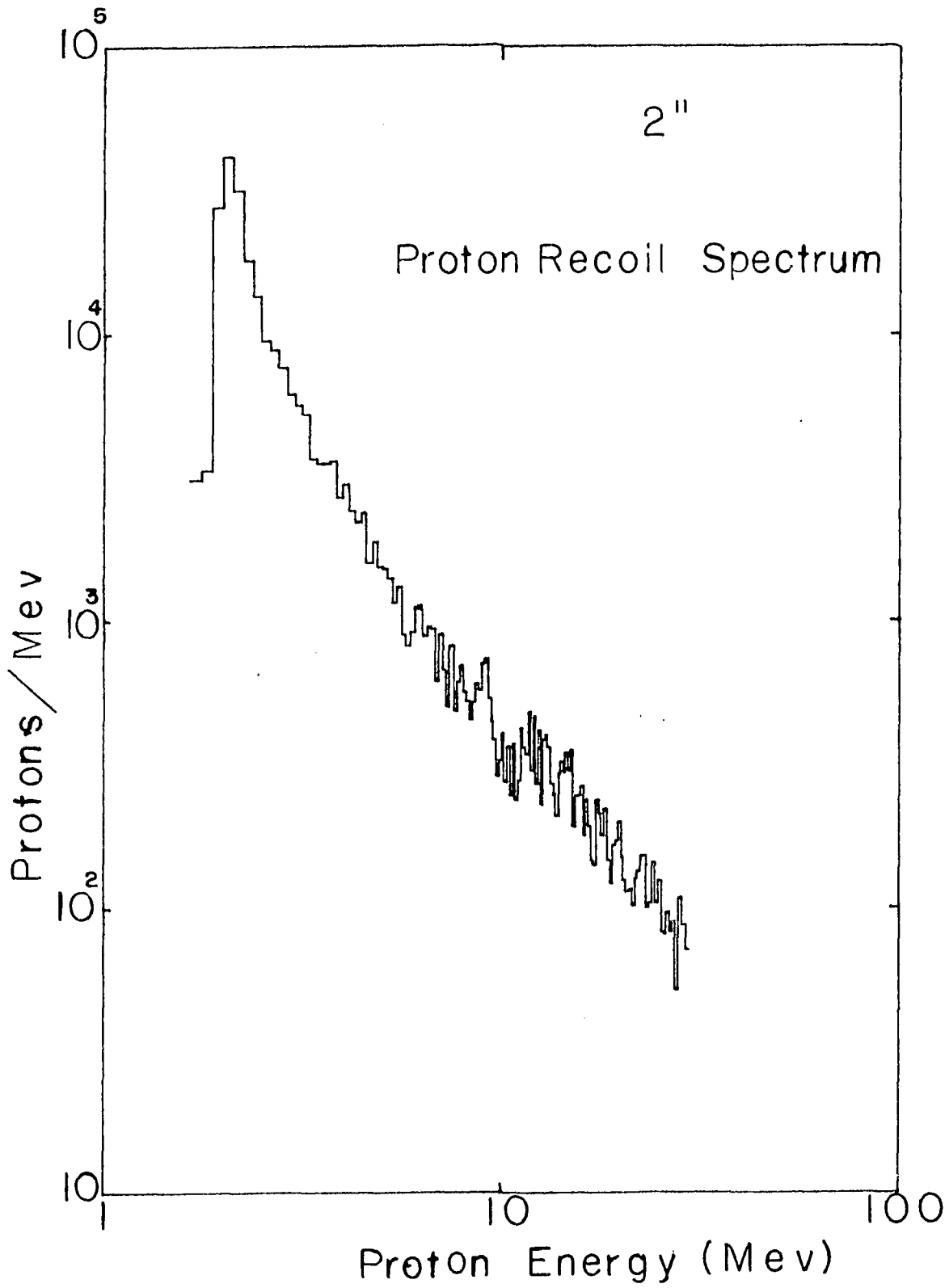   of the gondola was 233 cm.
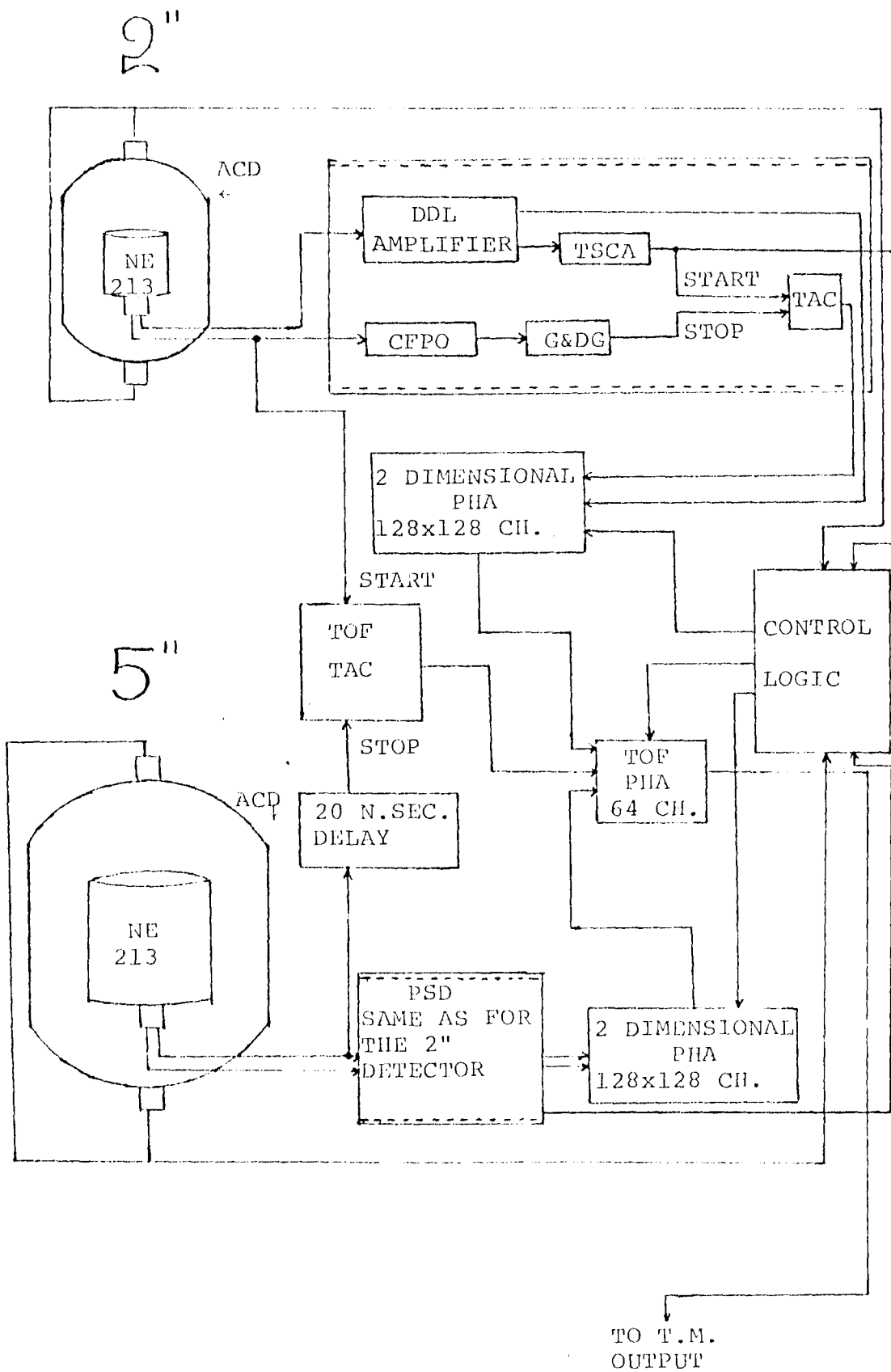
FIGURE 5-1
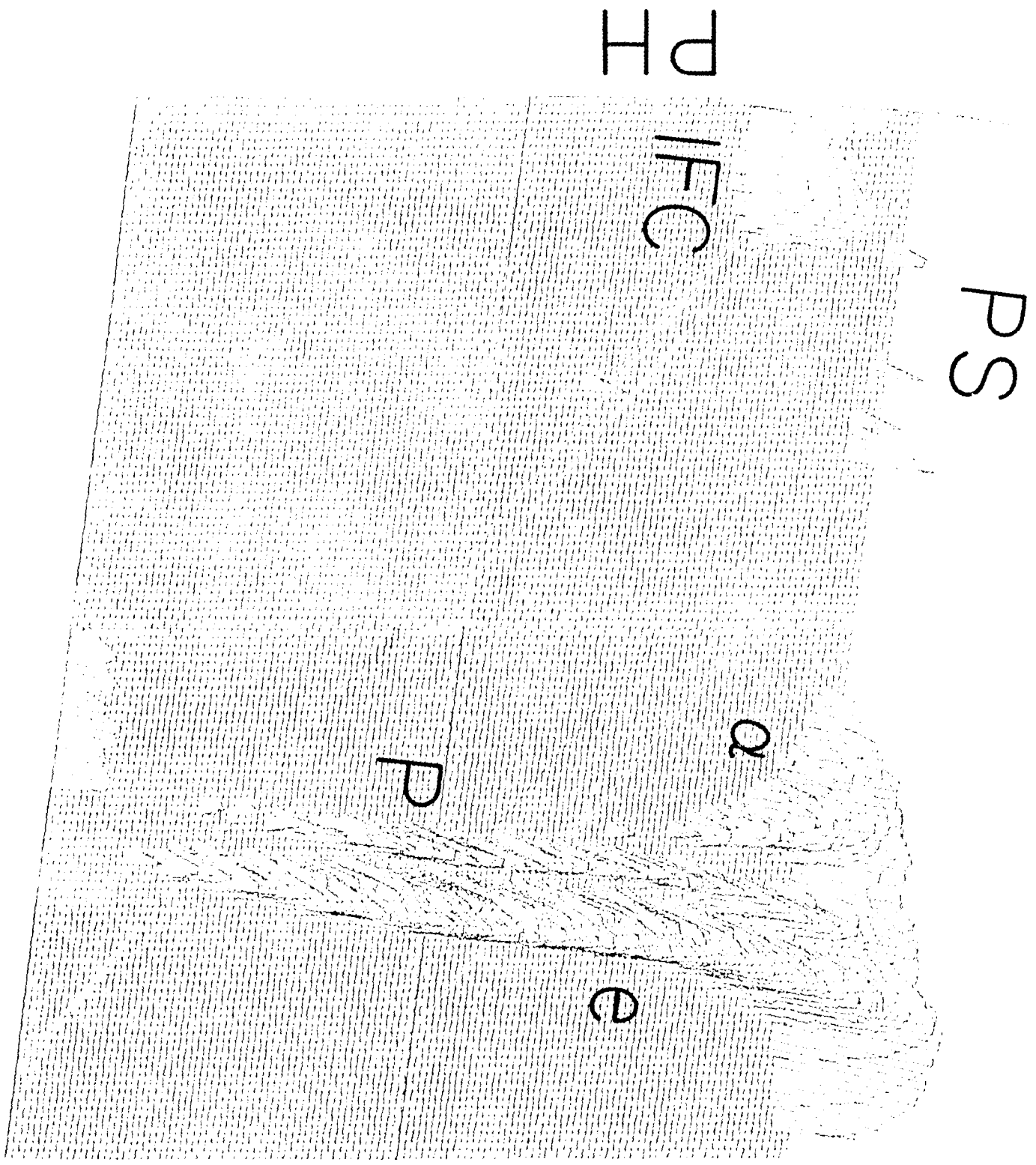
FIGURE 5-2
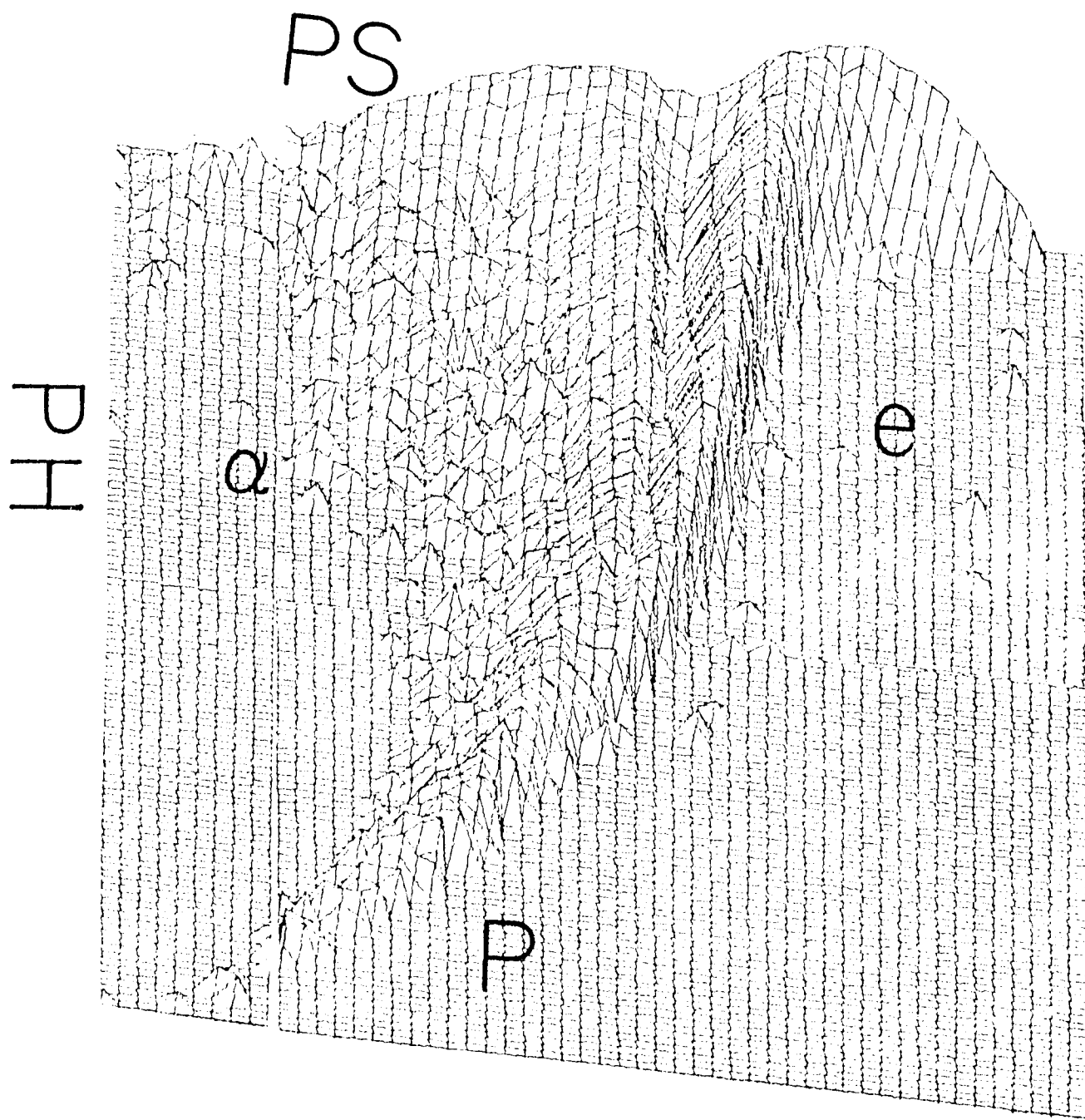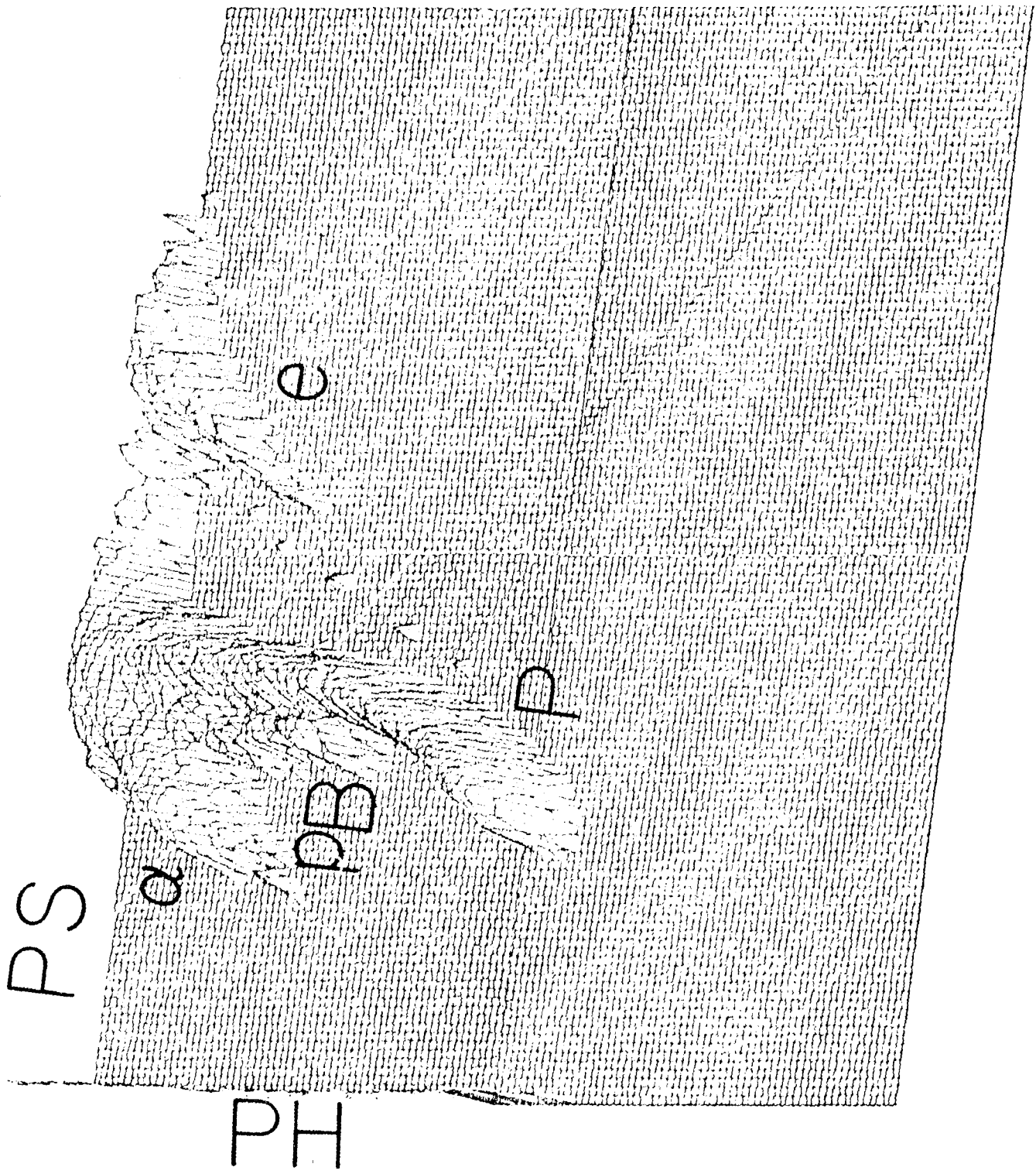
FIGURE 5-3

FIGURE 5-4

FIGURE 5-5

CHANNEL NUMBER

$E_p(Mev)$
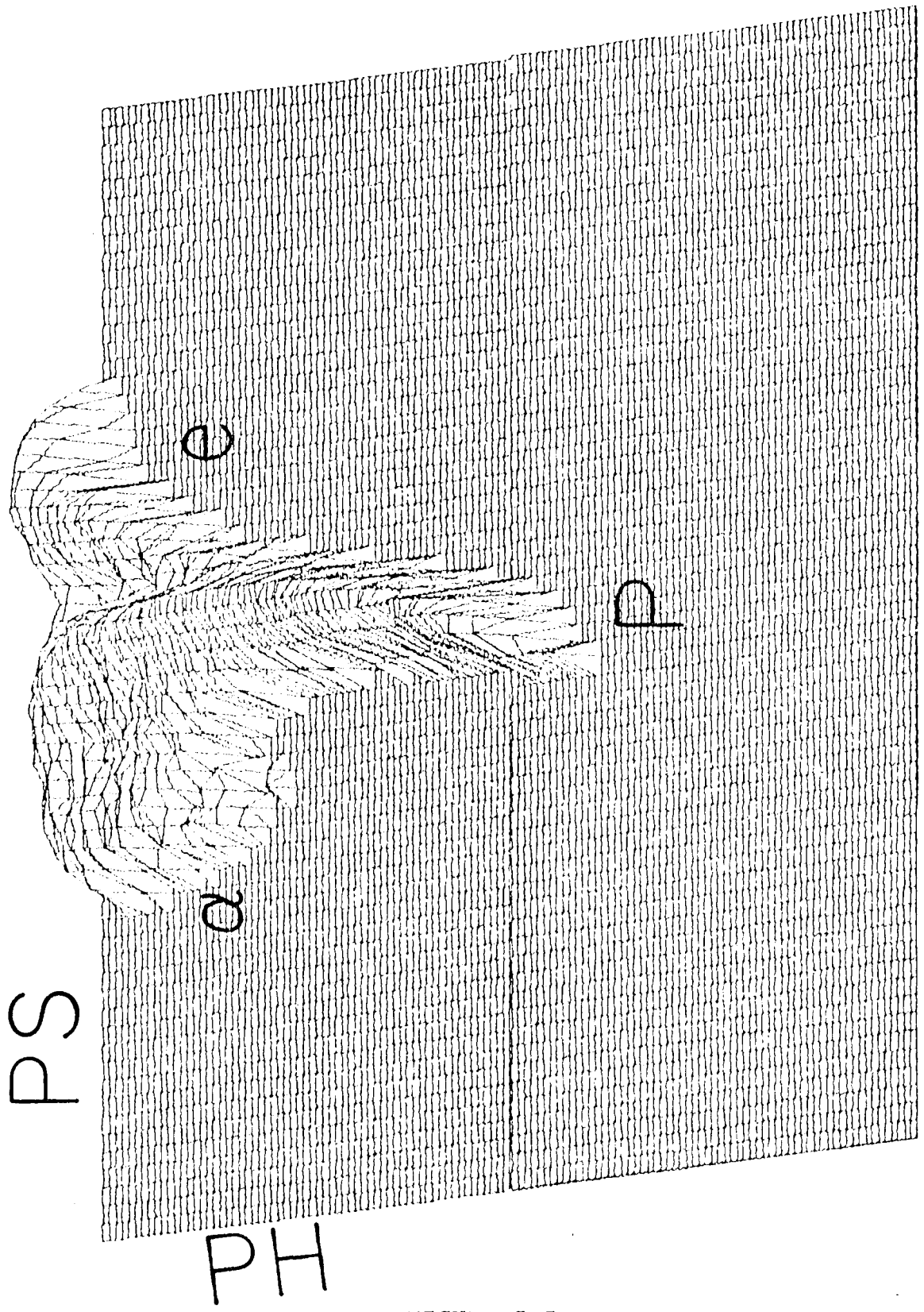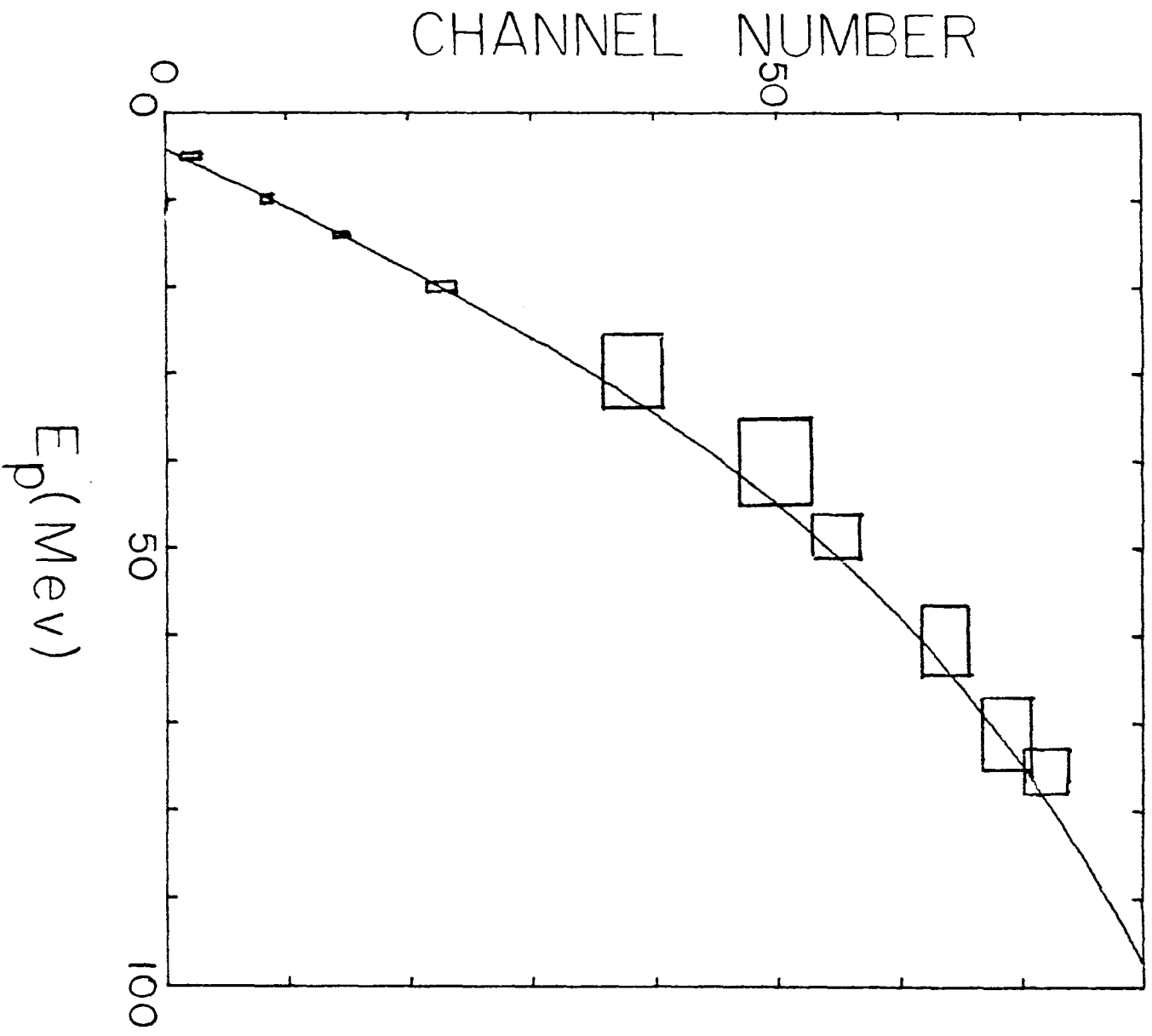
FIGURE 7-1

FIGURE 7-2

FIGURE 7-3

Run 20   14.5 MeV

Run 19   19.9 MeV

Run 18   27.7 MeV

Run 17   39.4 MeV

Protons / MeV

E_p MeV
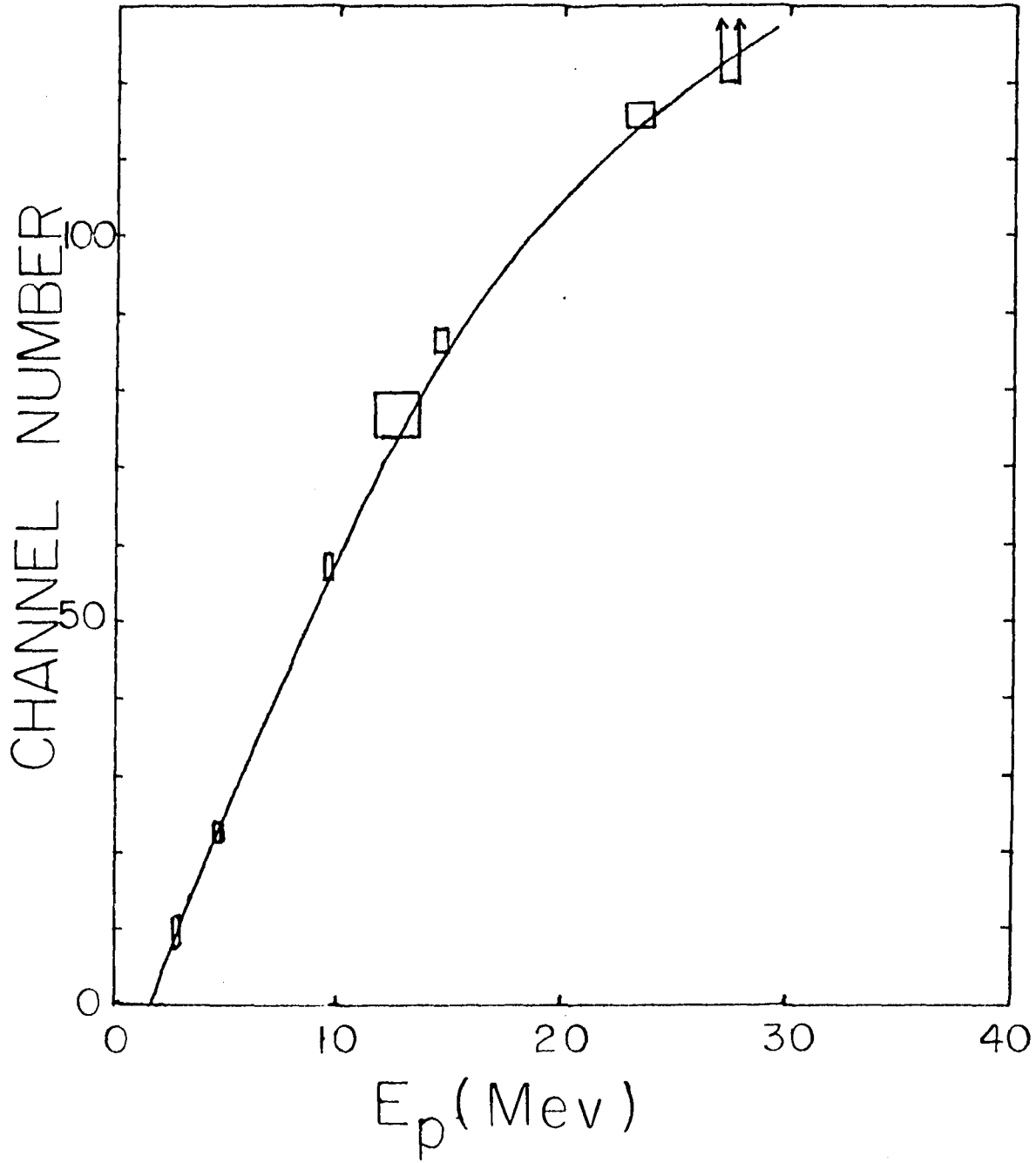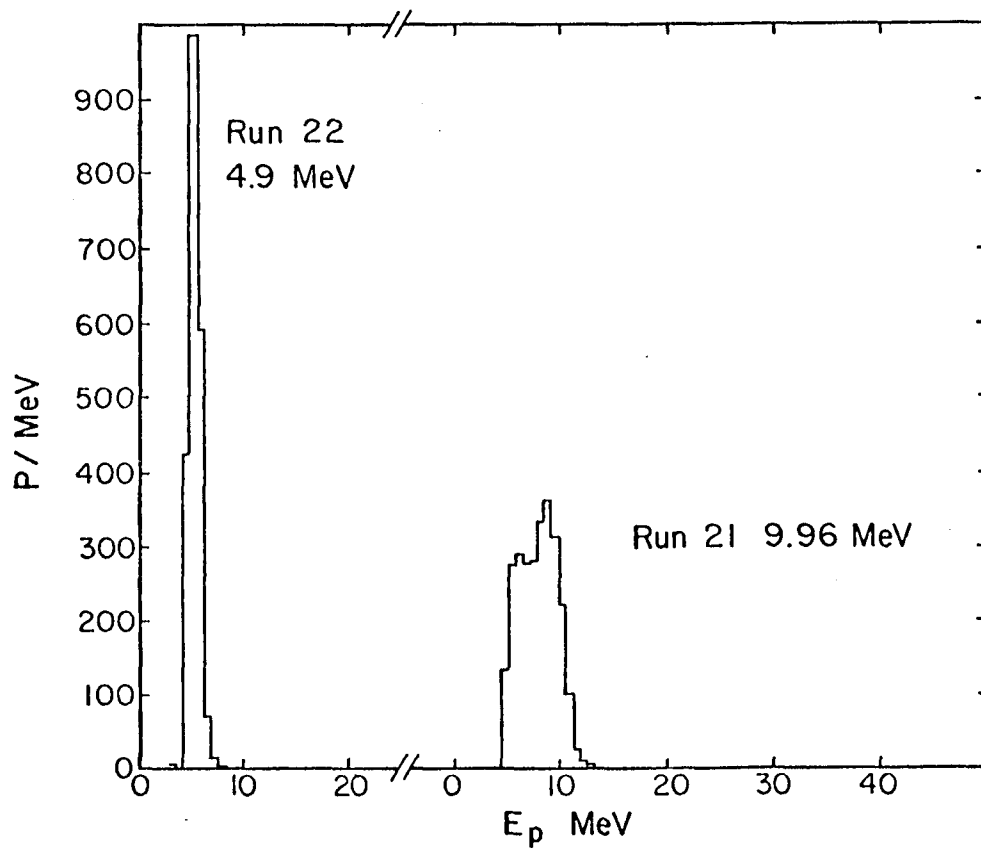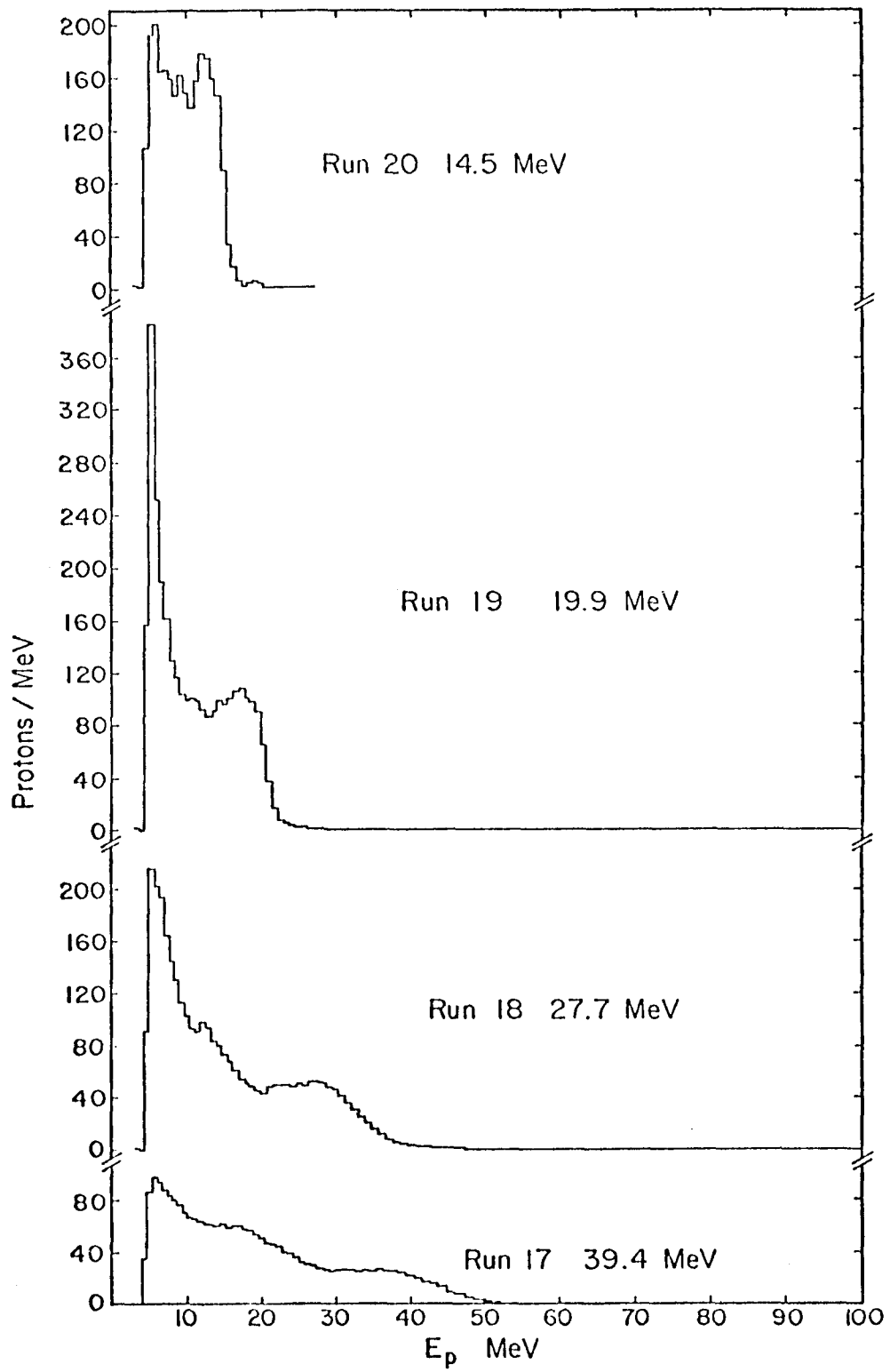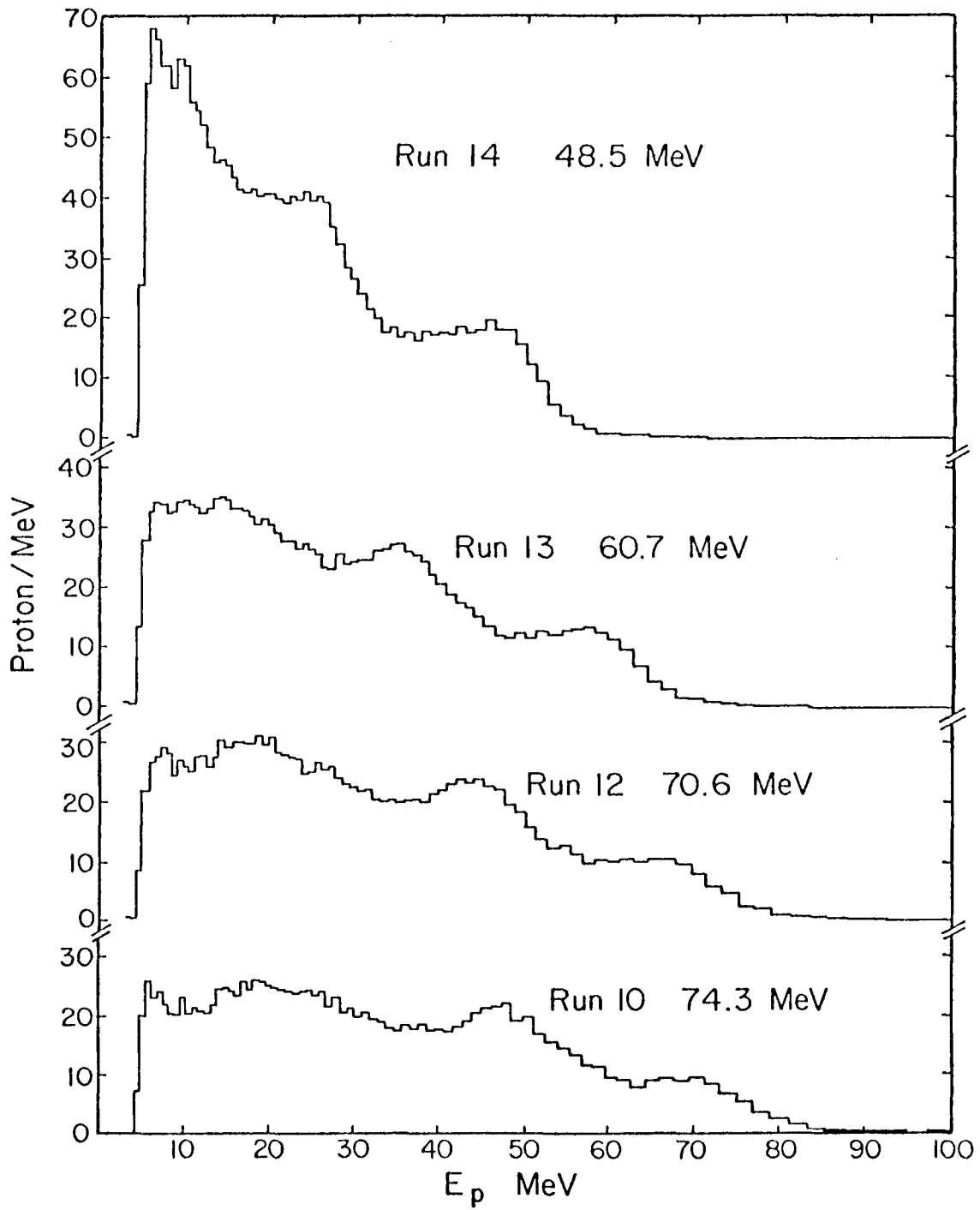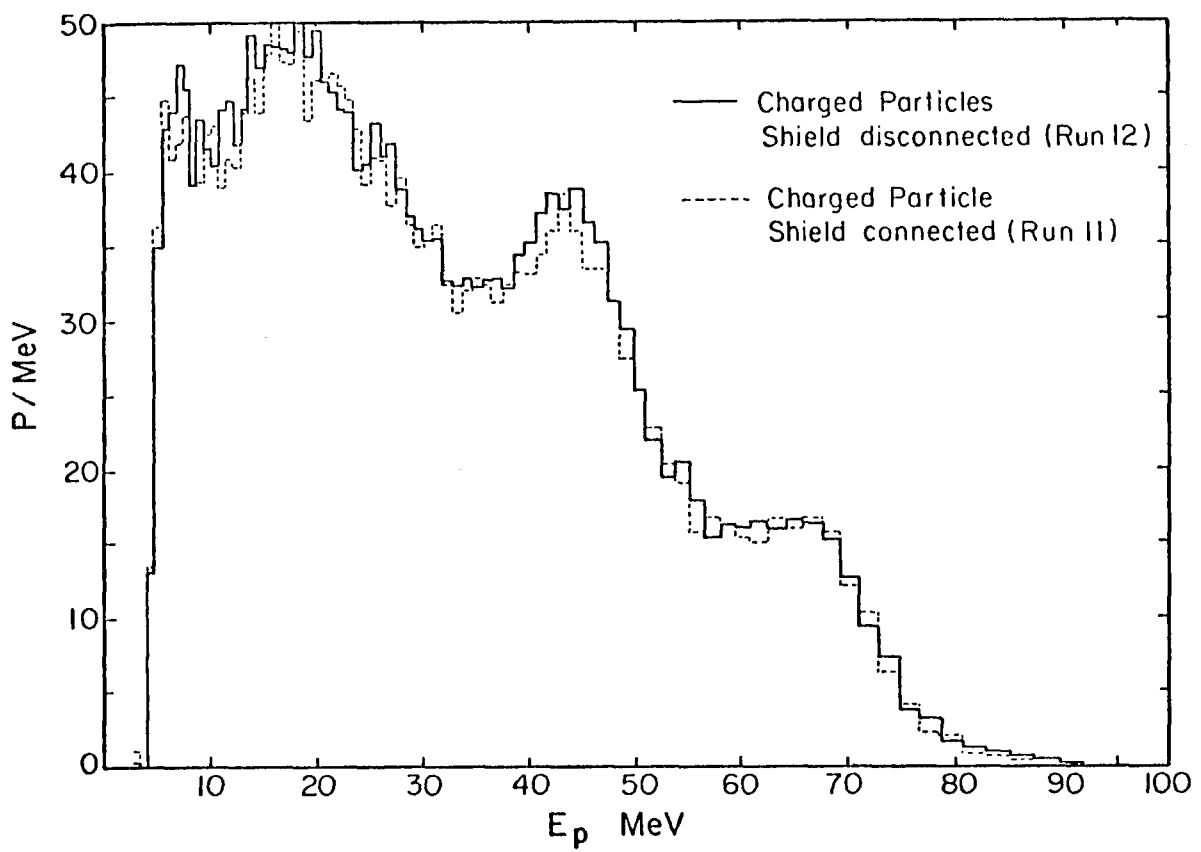
FIGURE 7-4

FIGURE 7-5

FIGURE 7-6
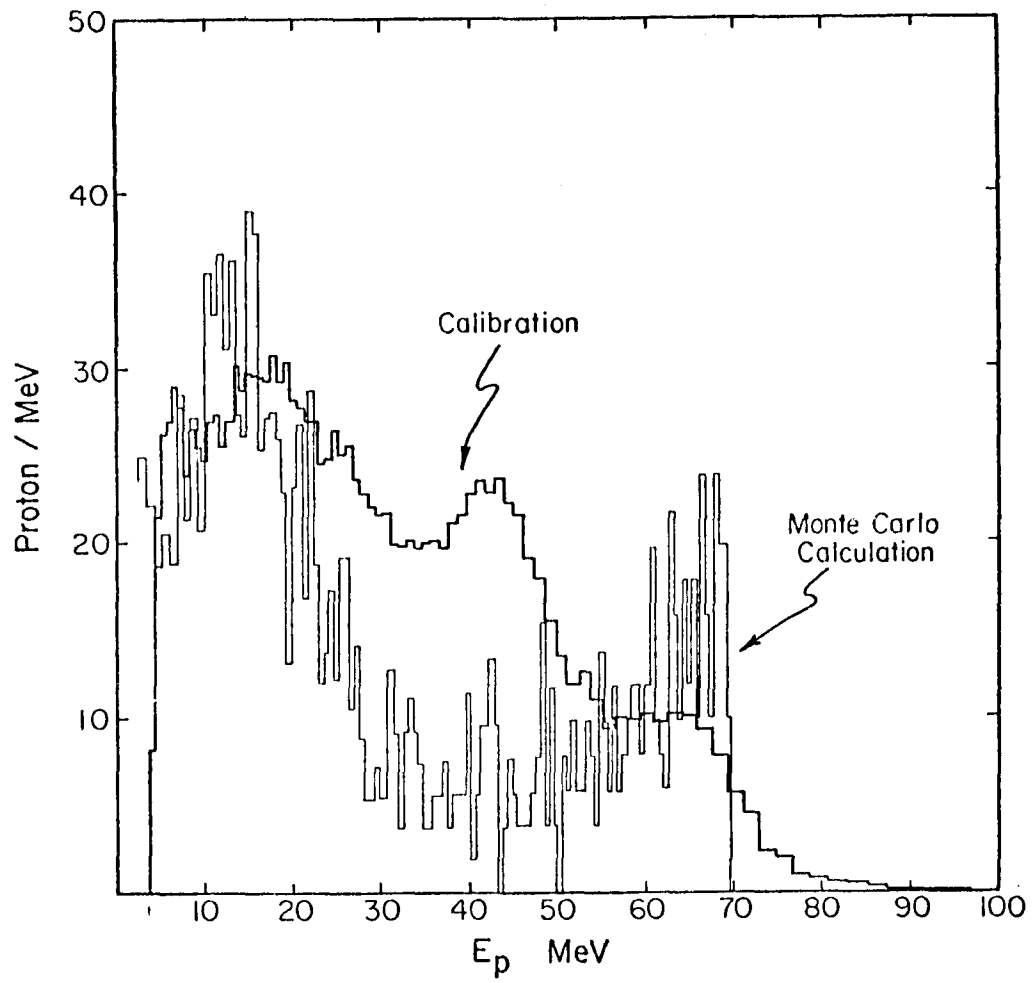
FIGURE 7-7
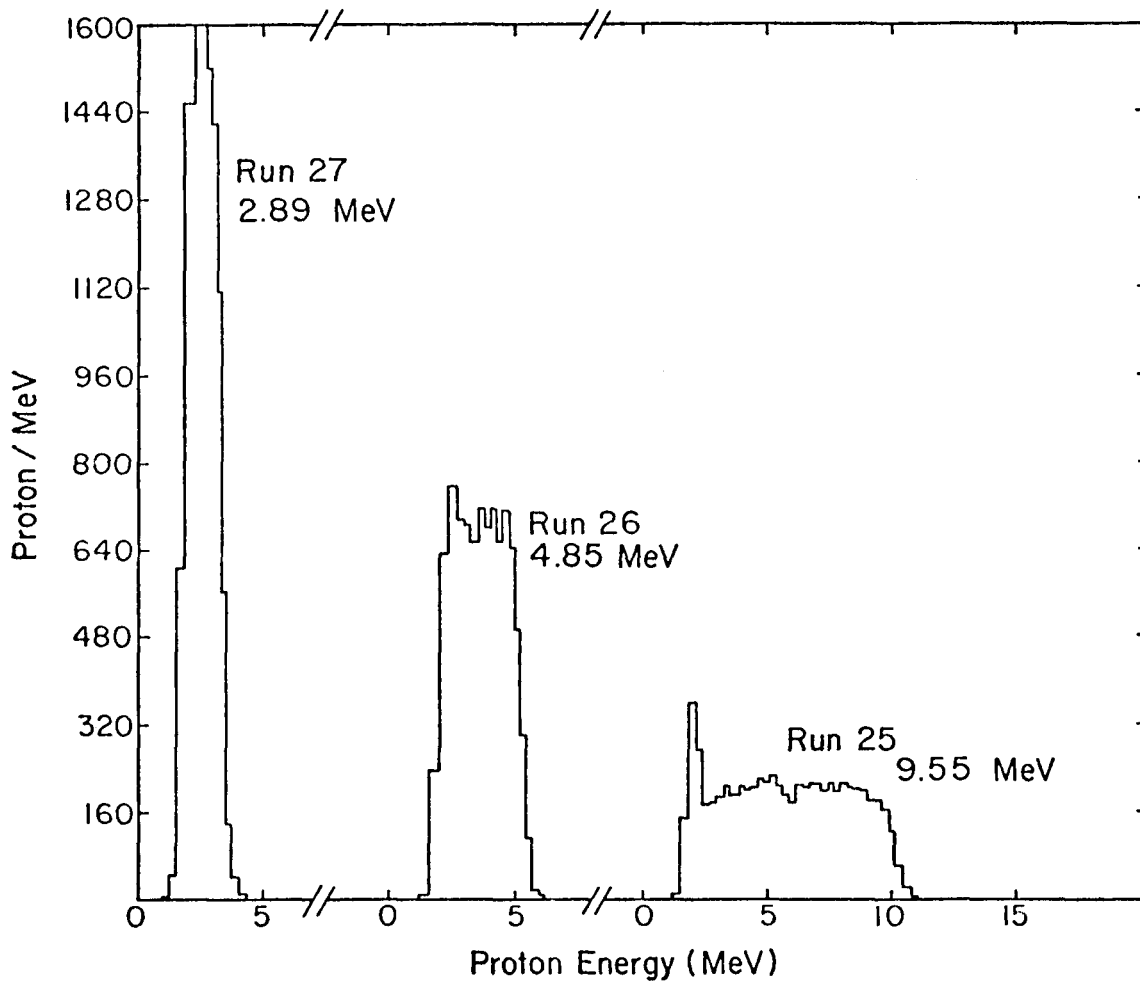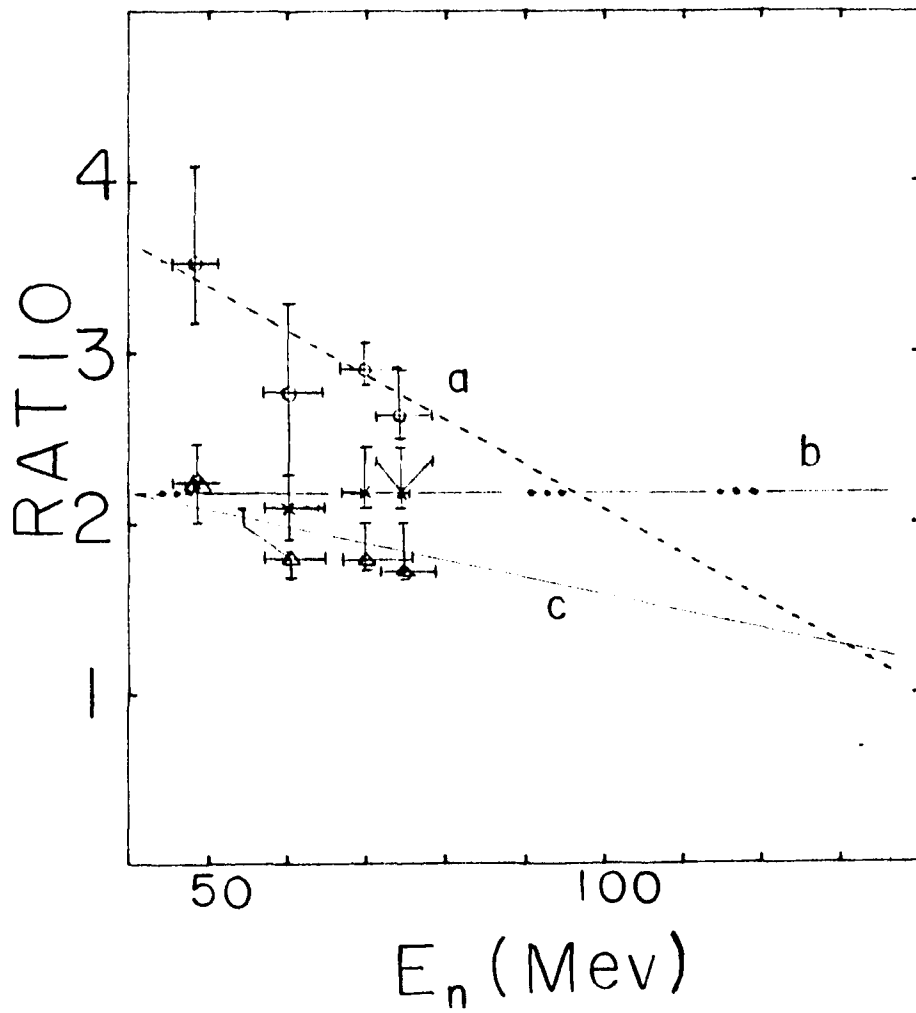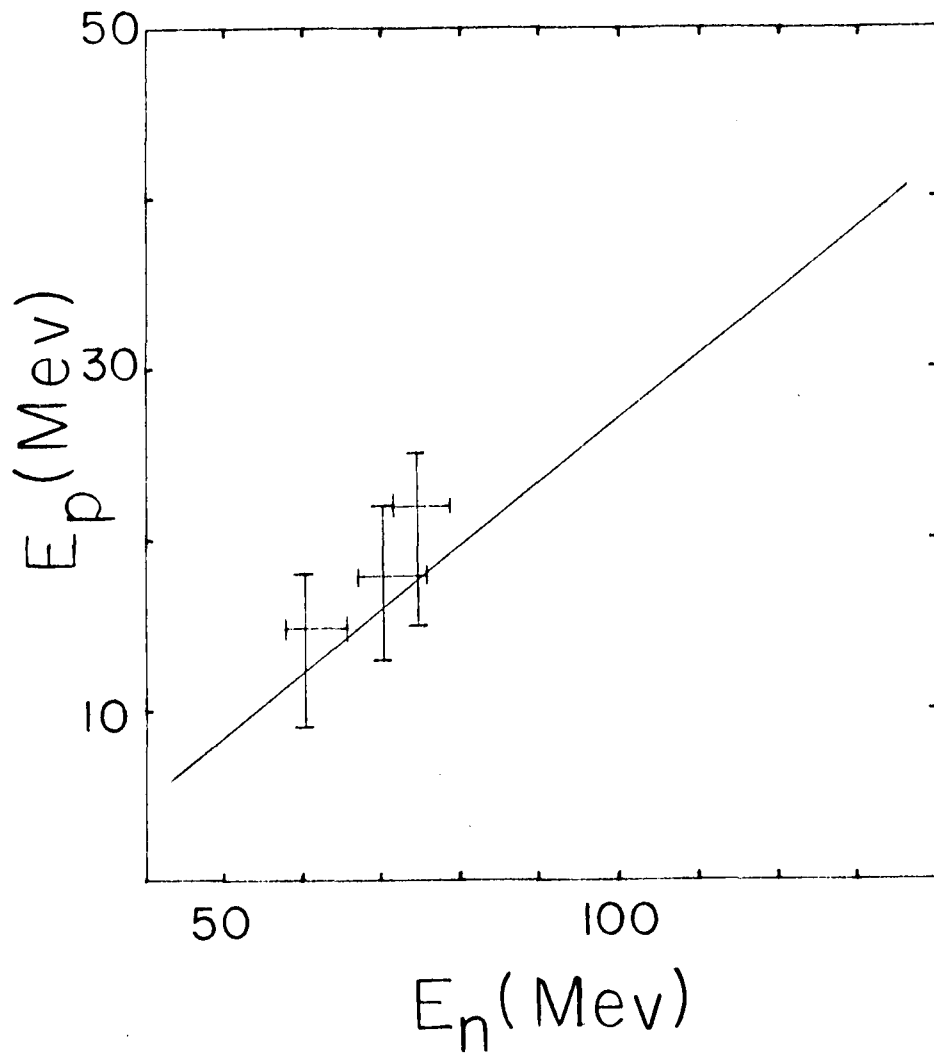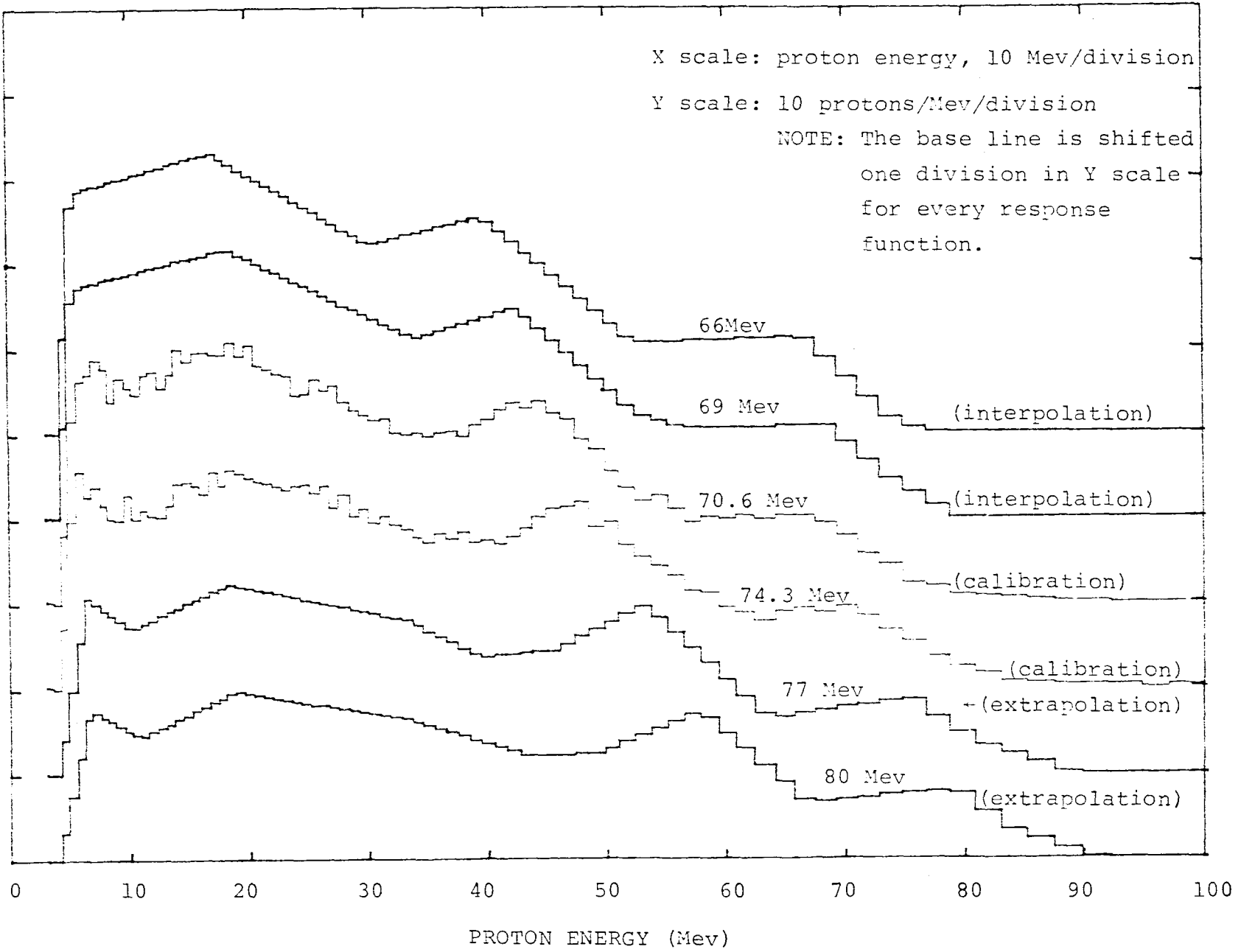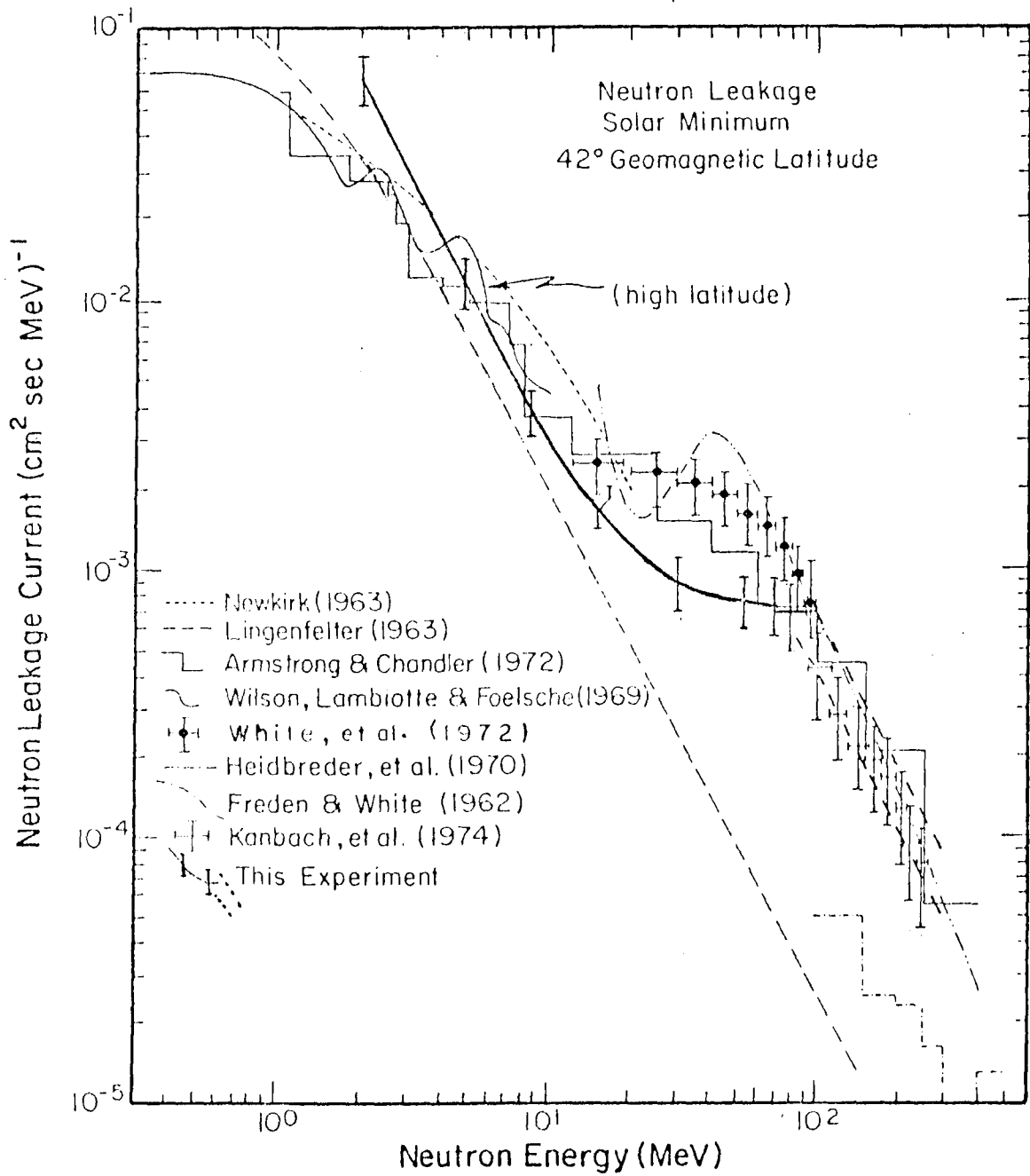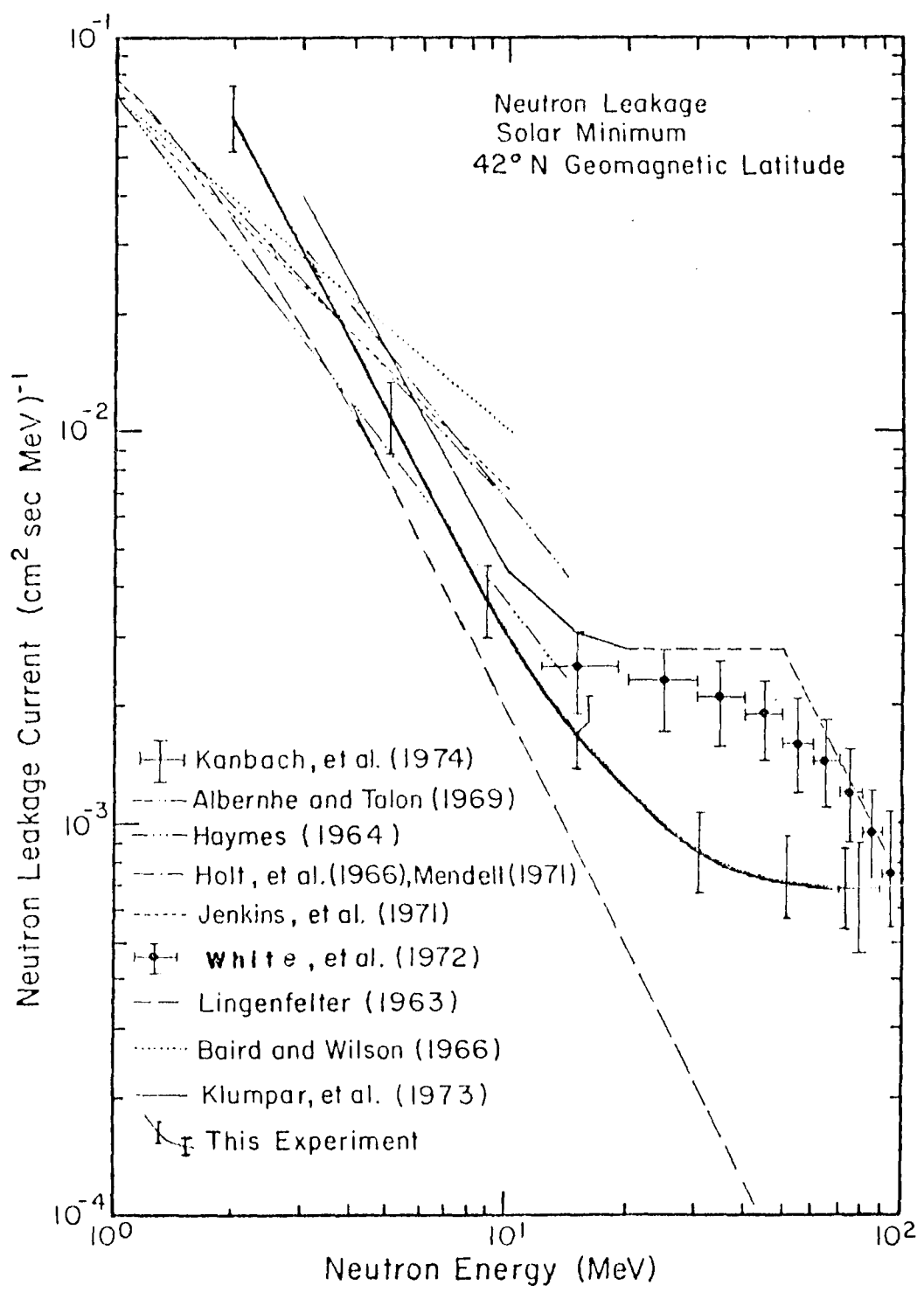
FIGURE 7-8
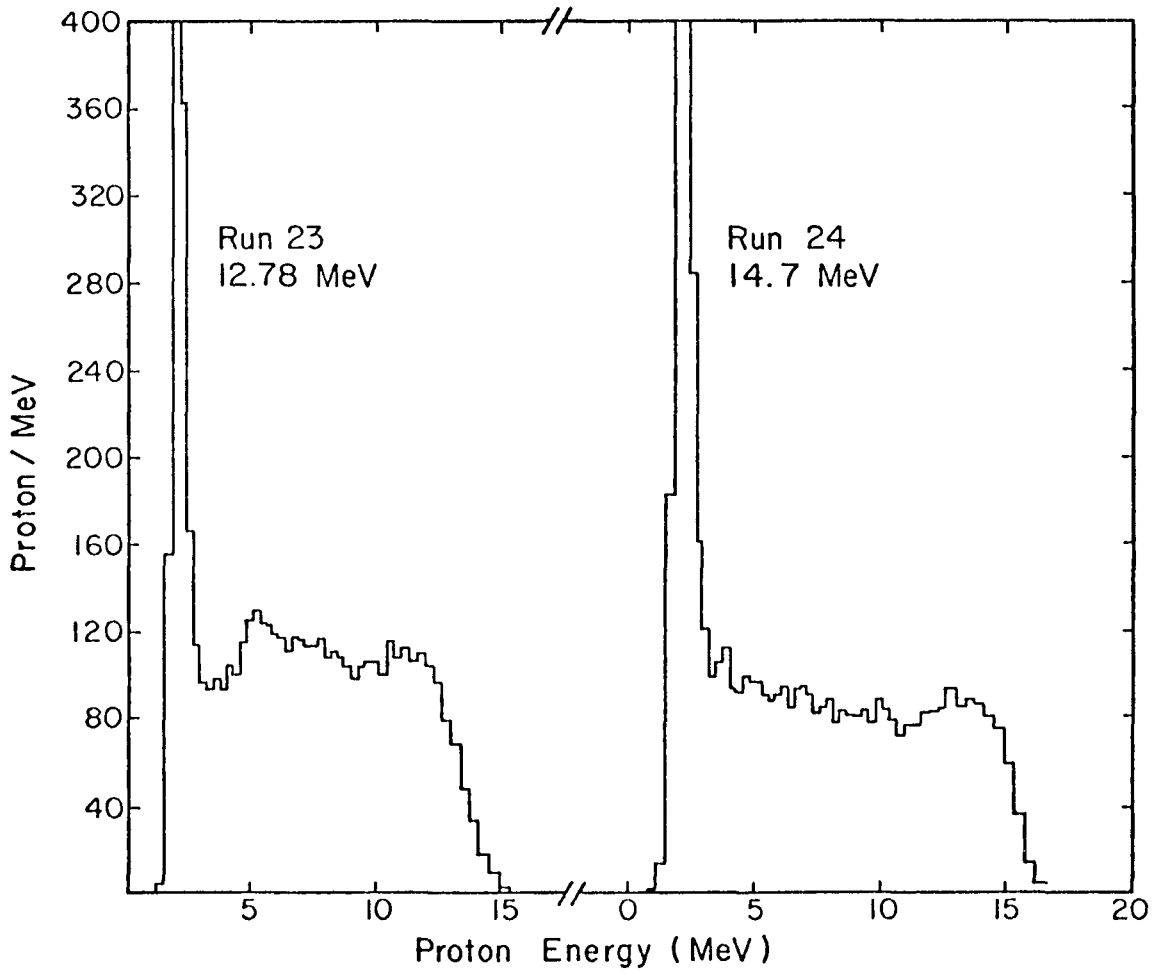
FIGURE 7-9
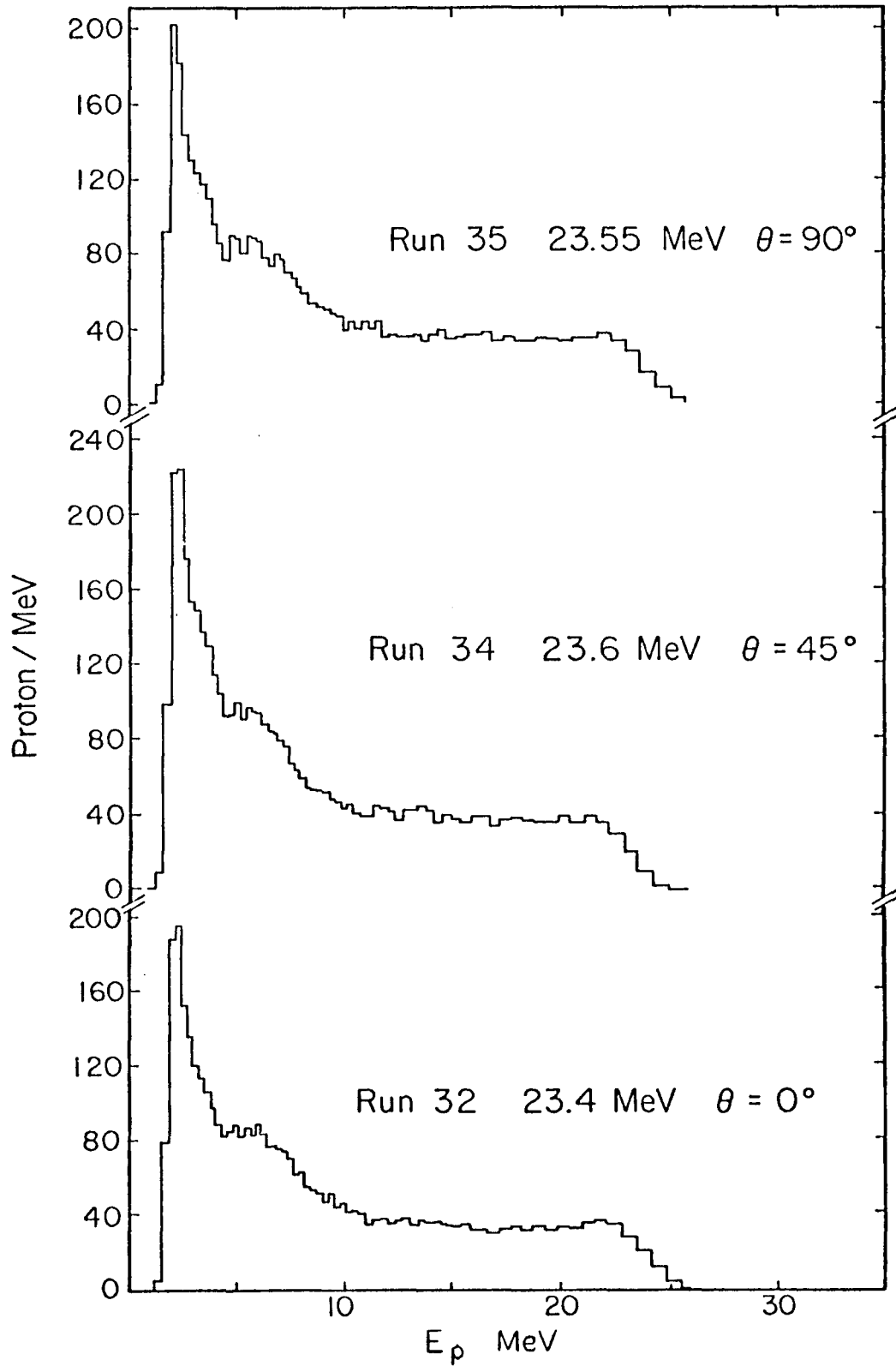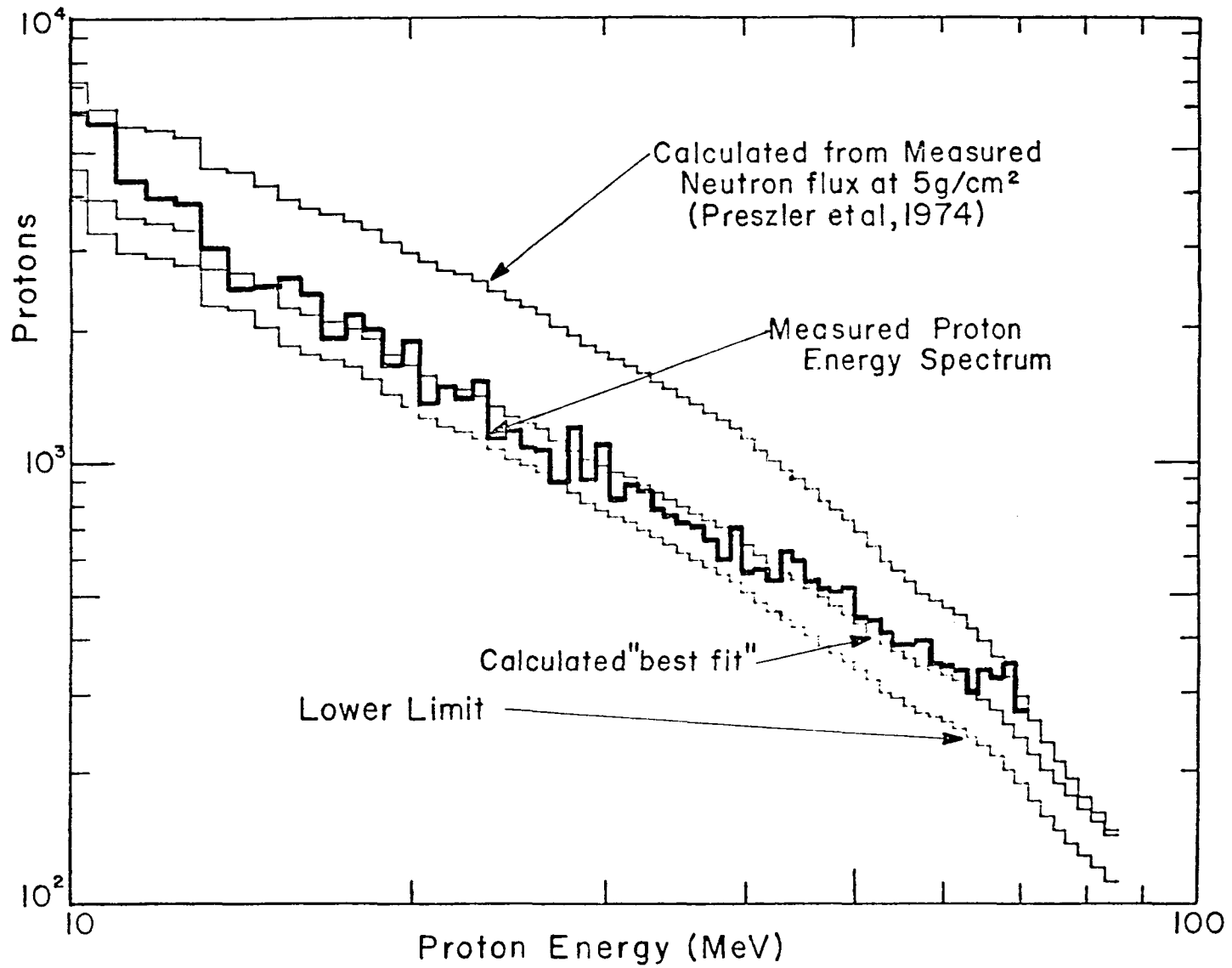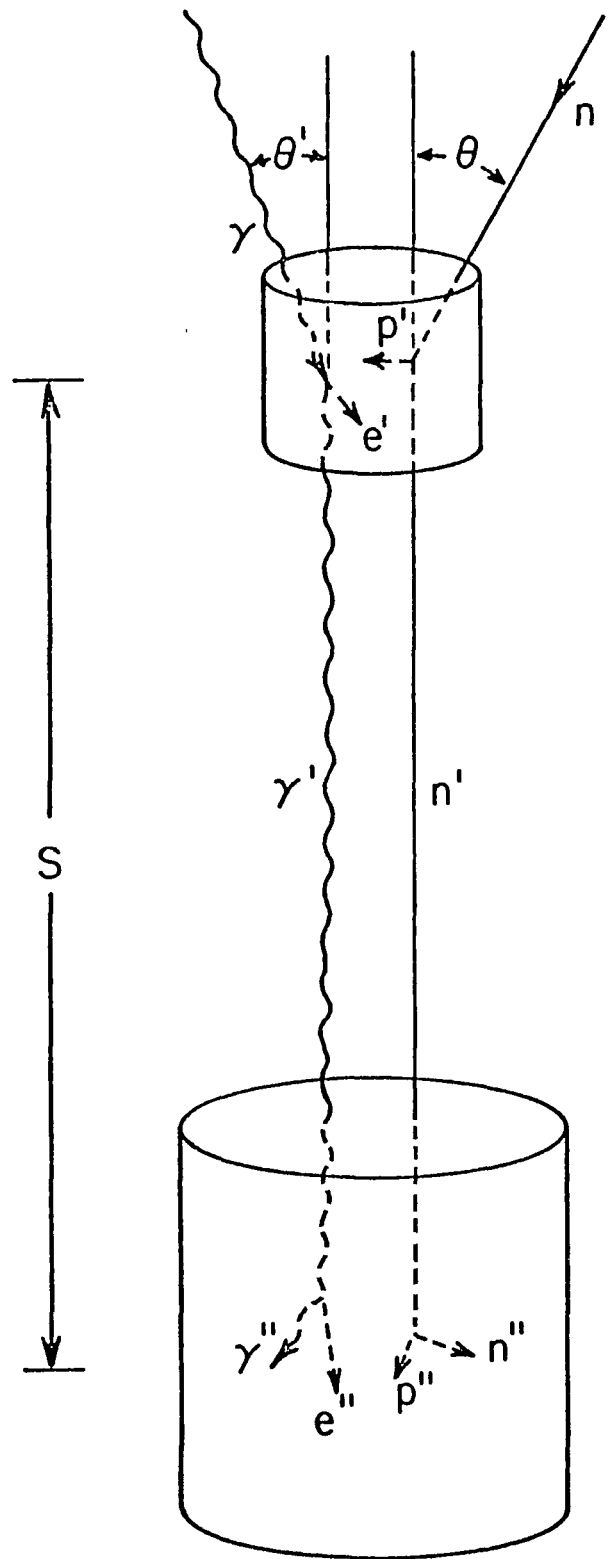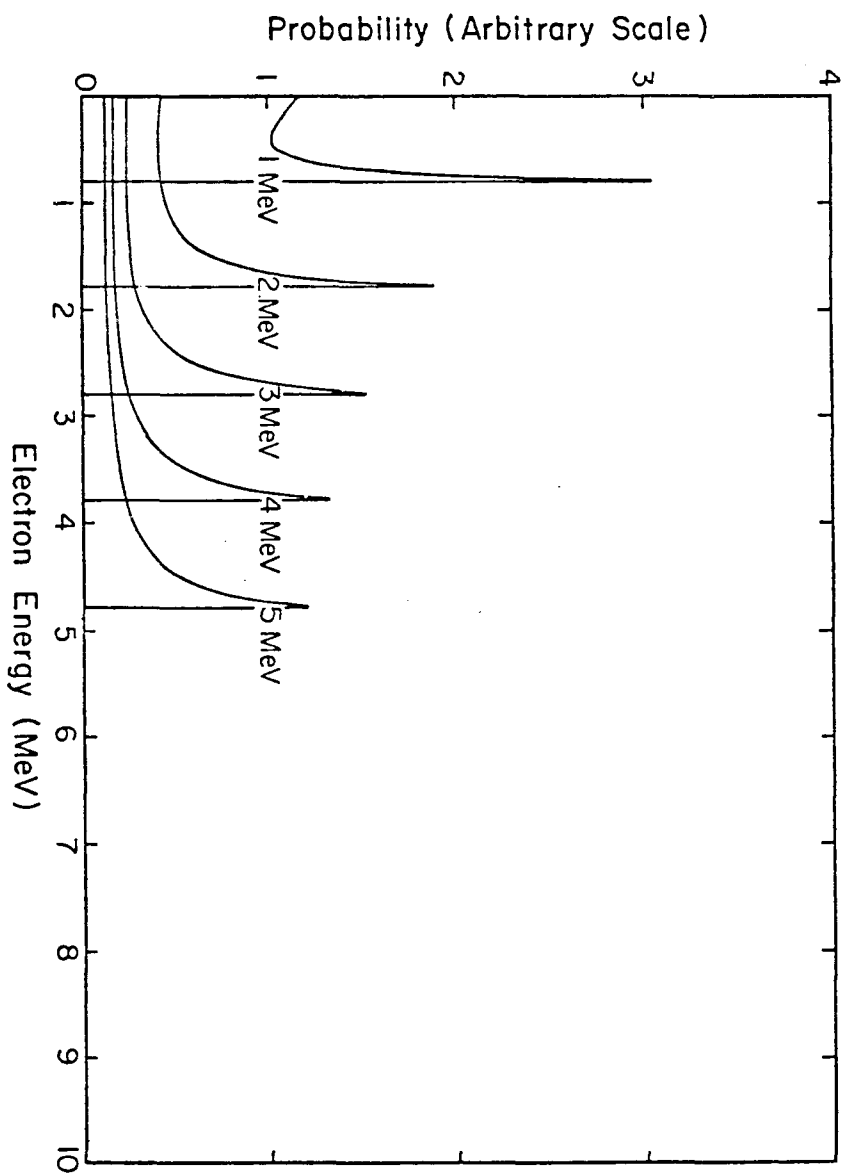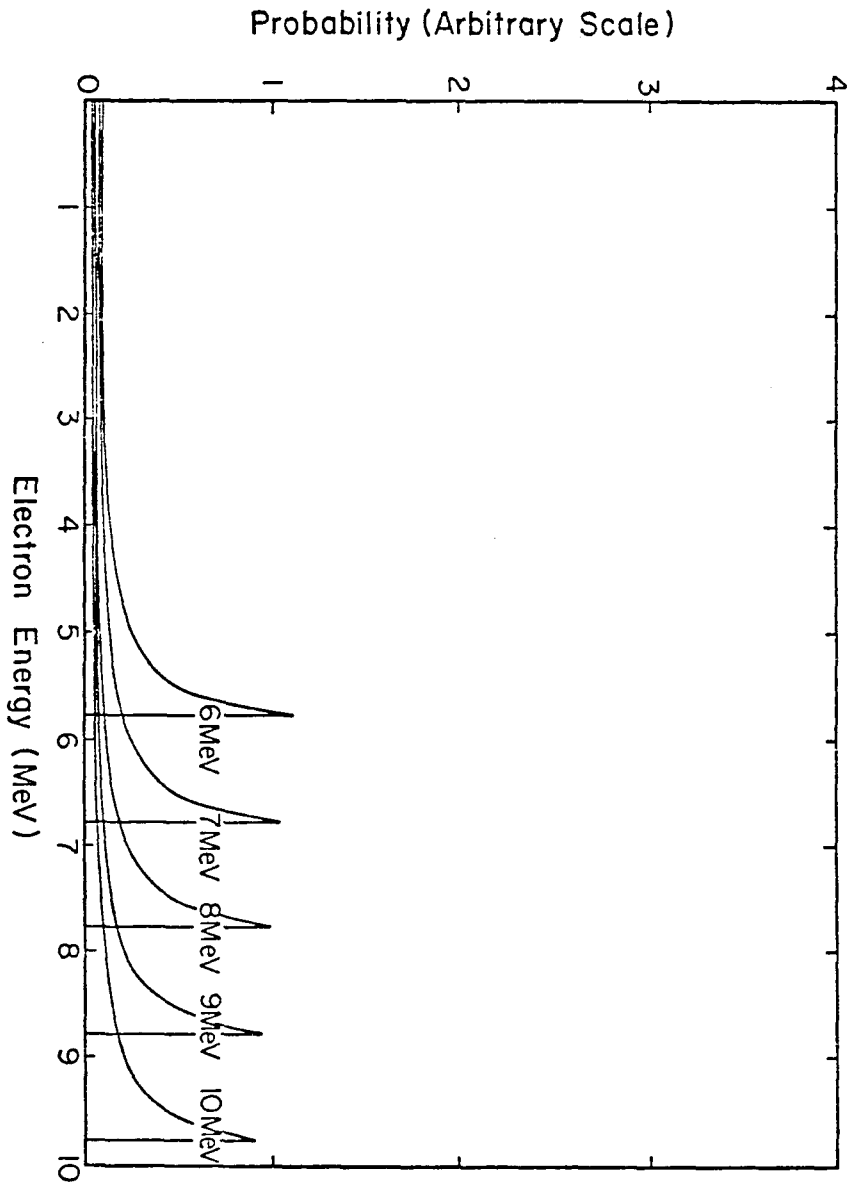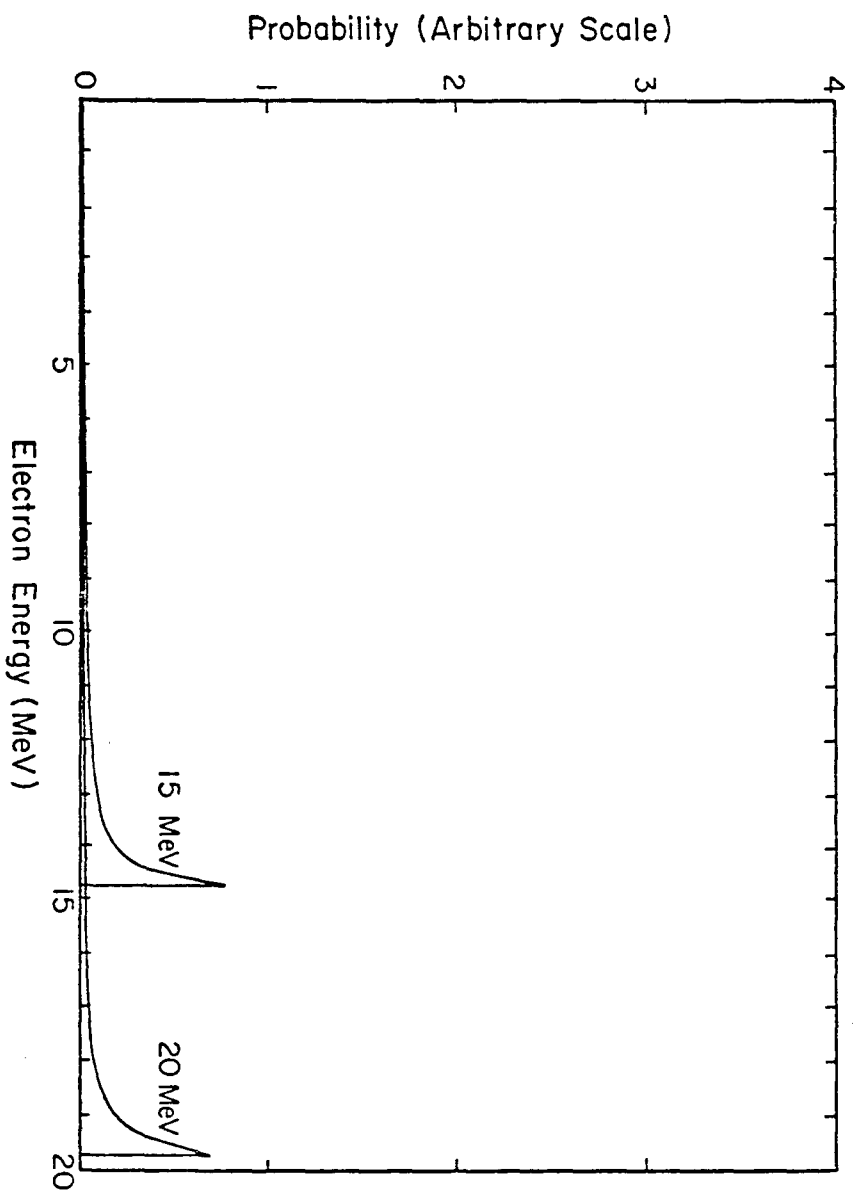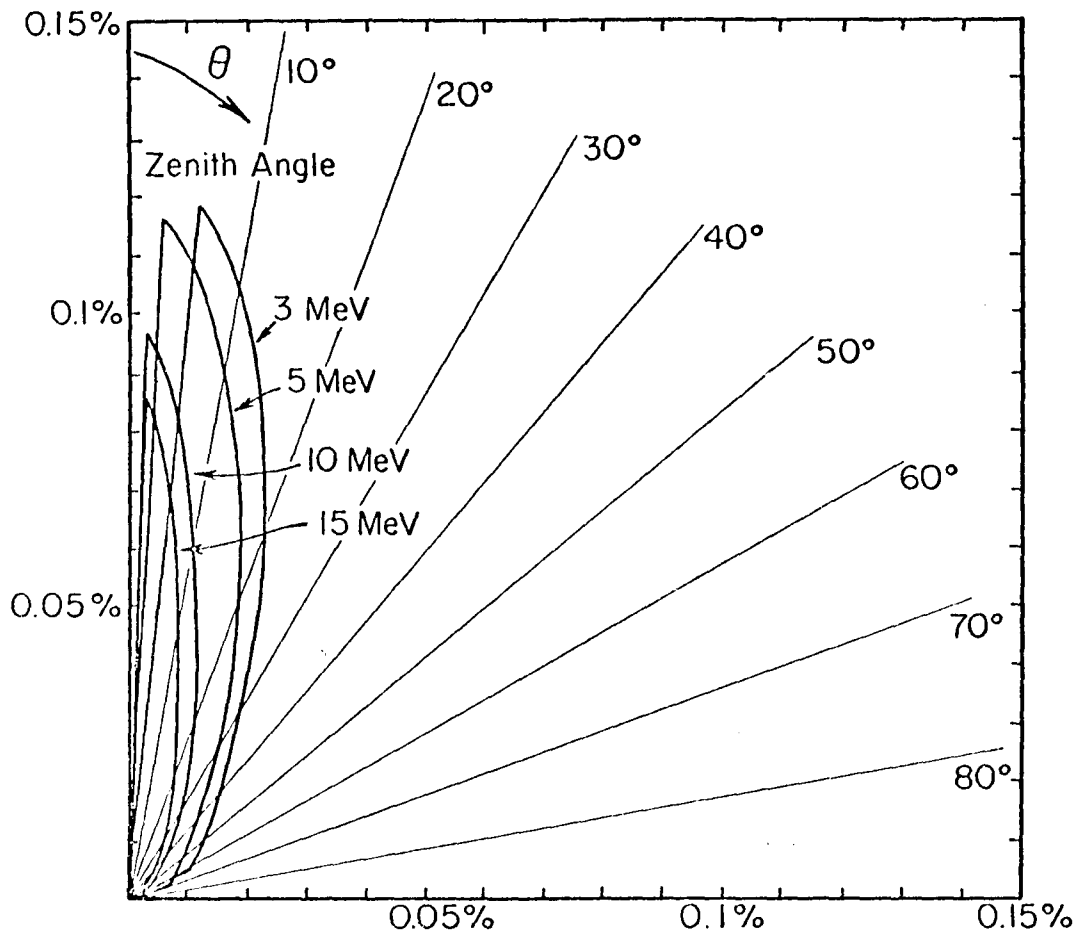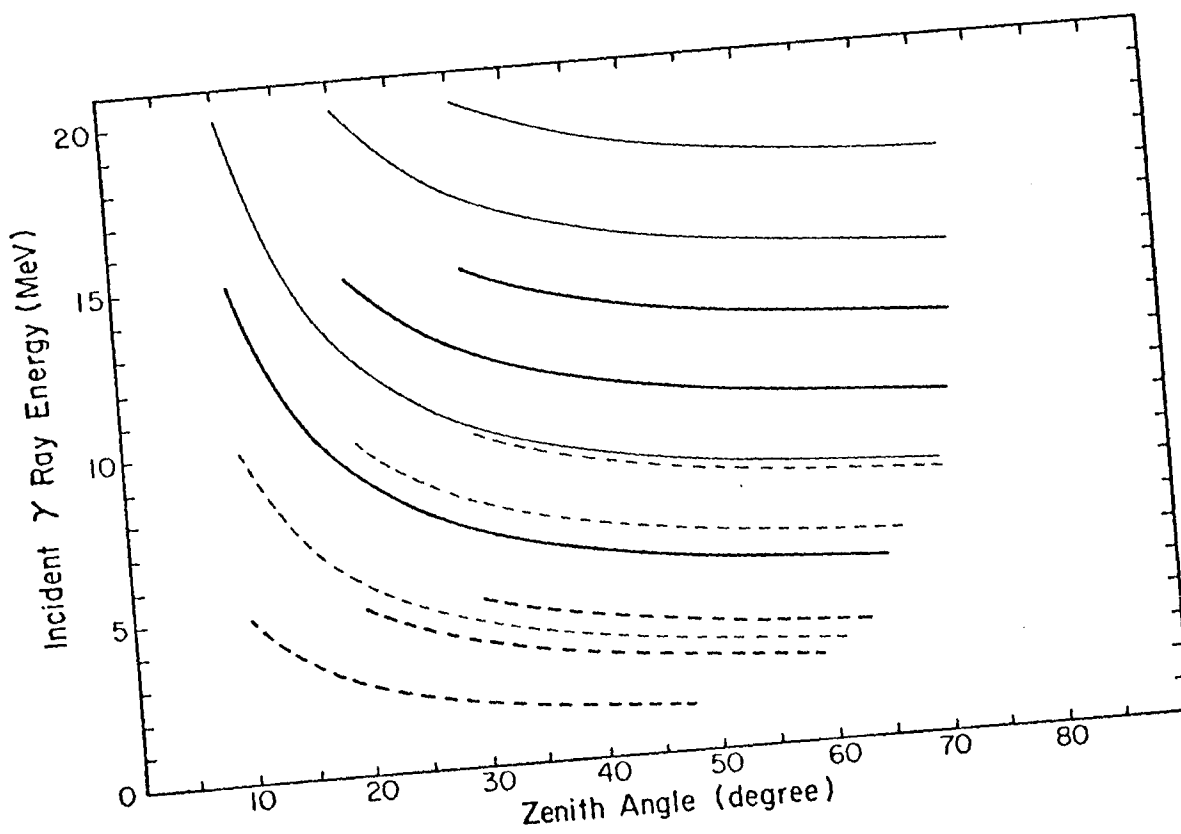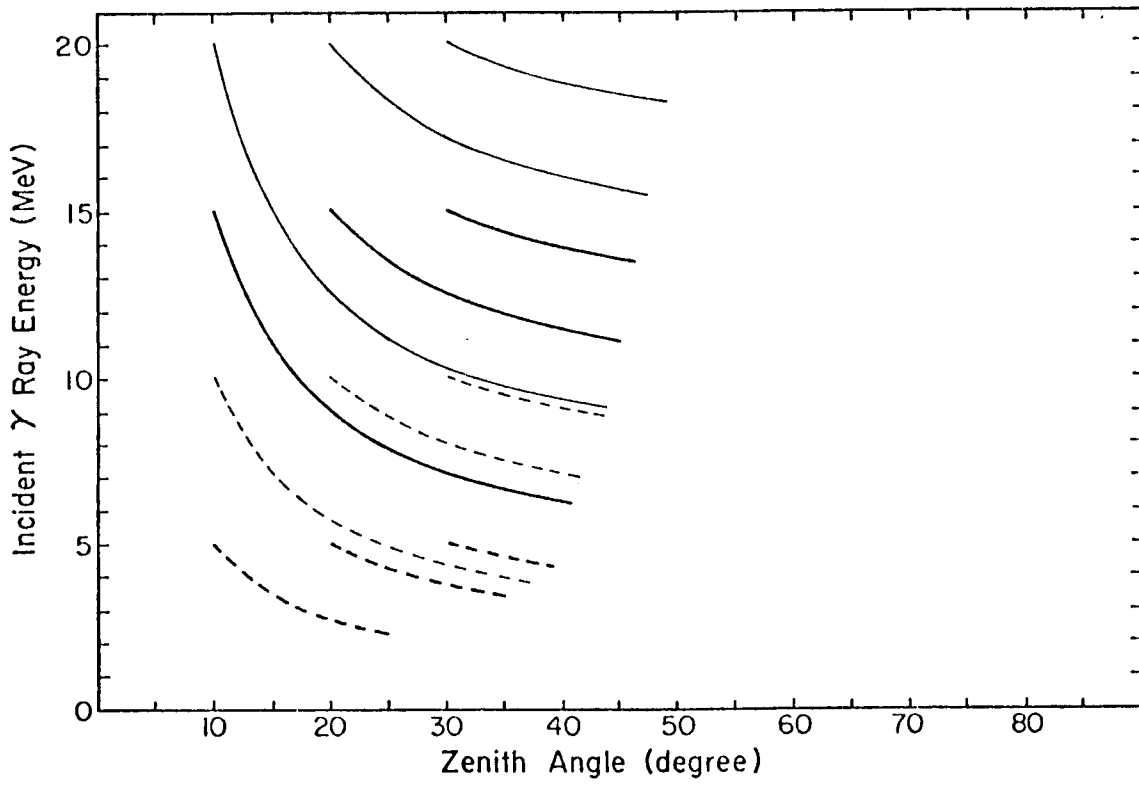
FIGURE 7-10
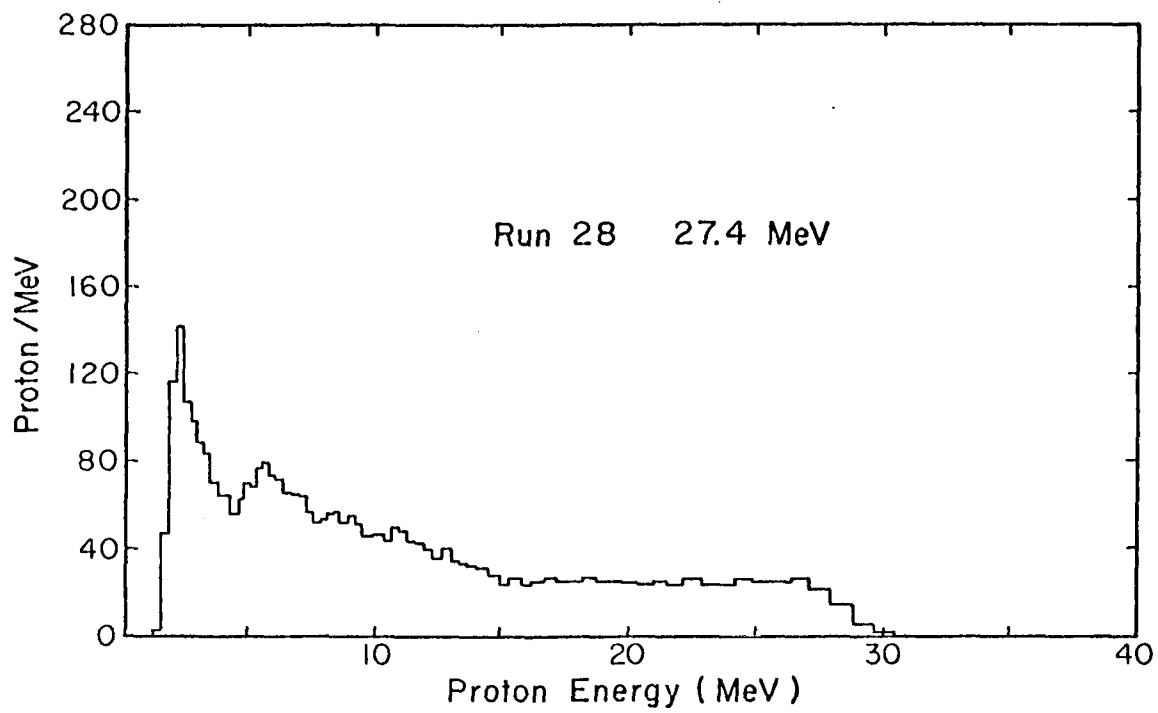
FIGURE 7-11
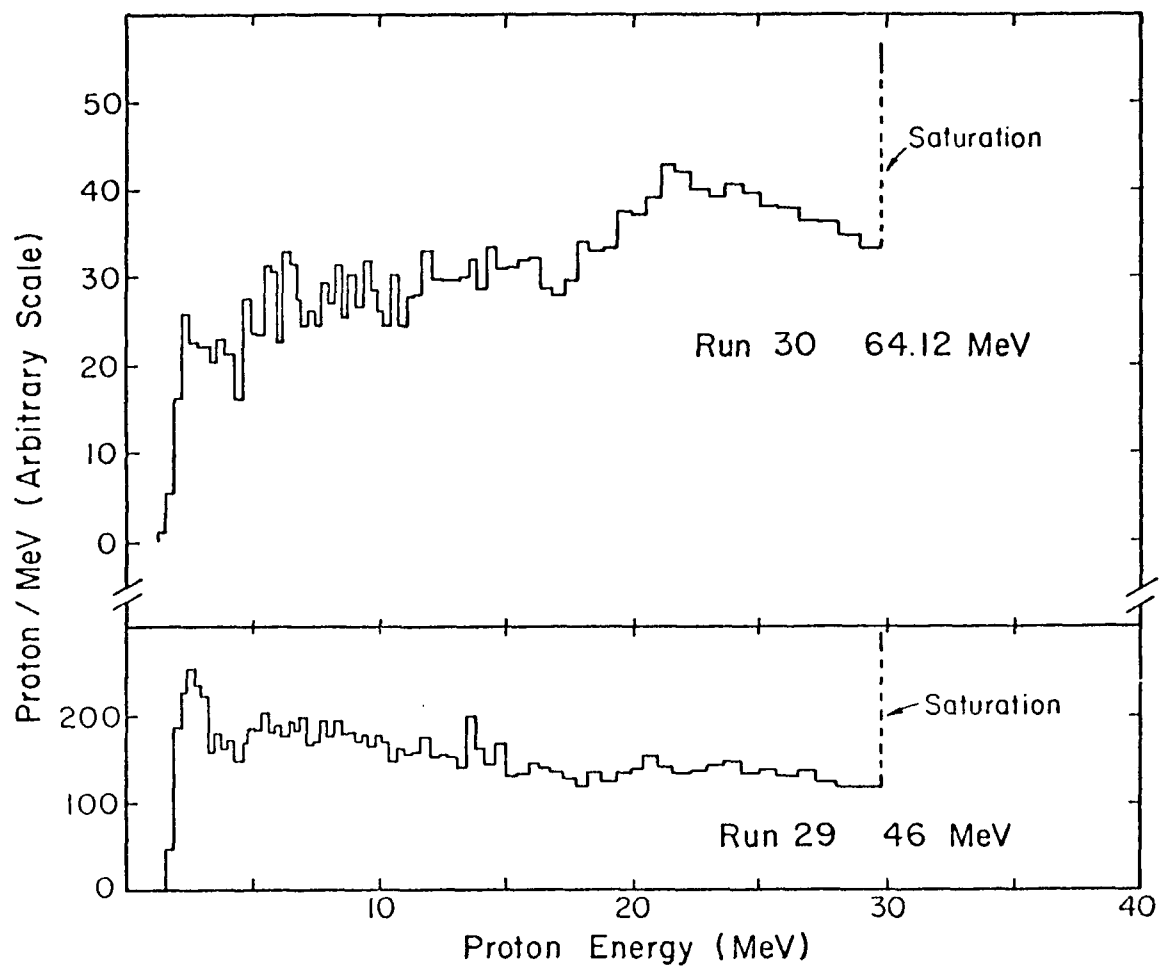
FIGURE 7-12
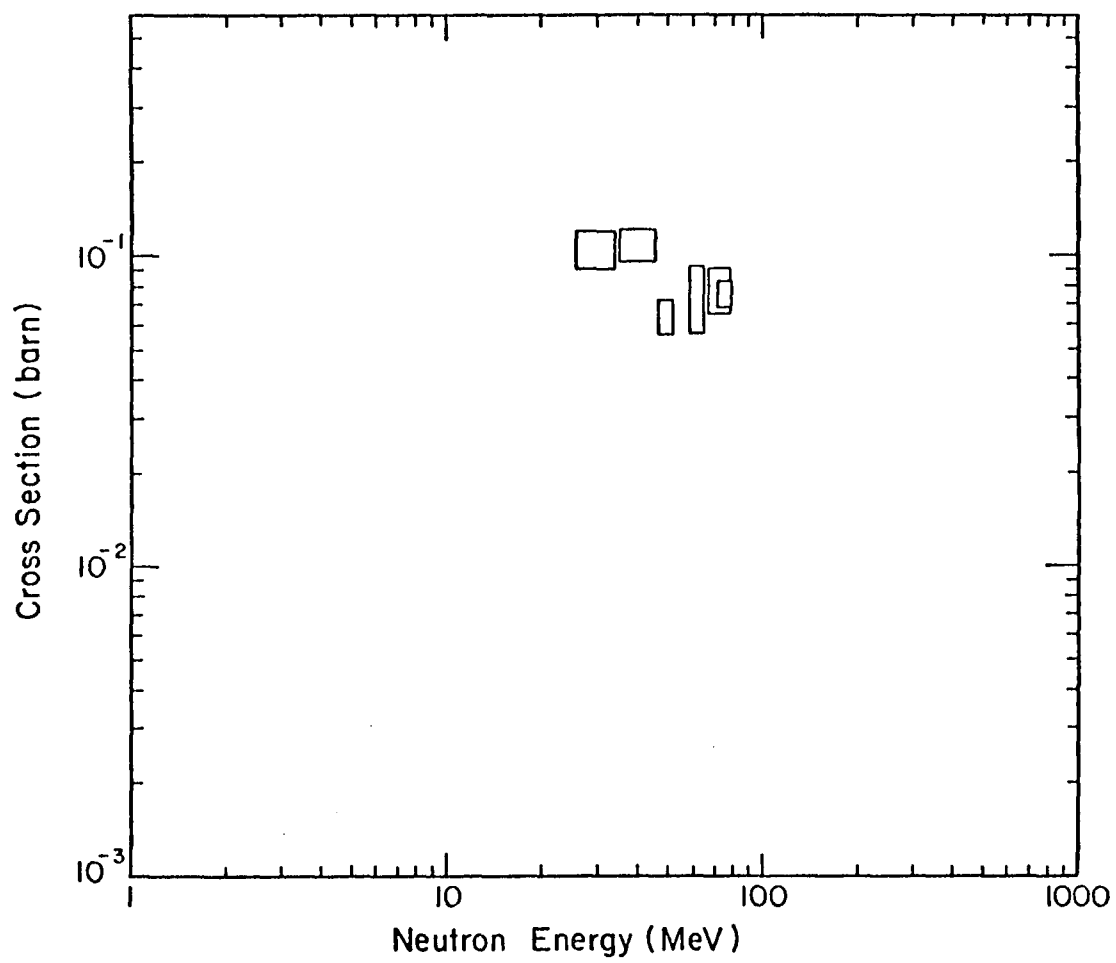
FIGURE 7-13
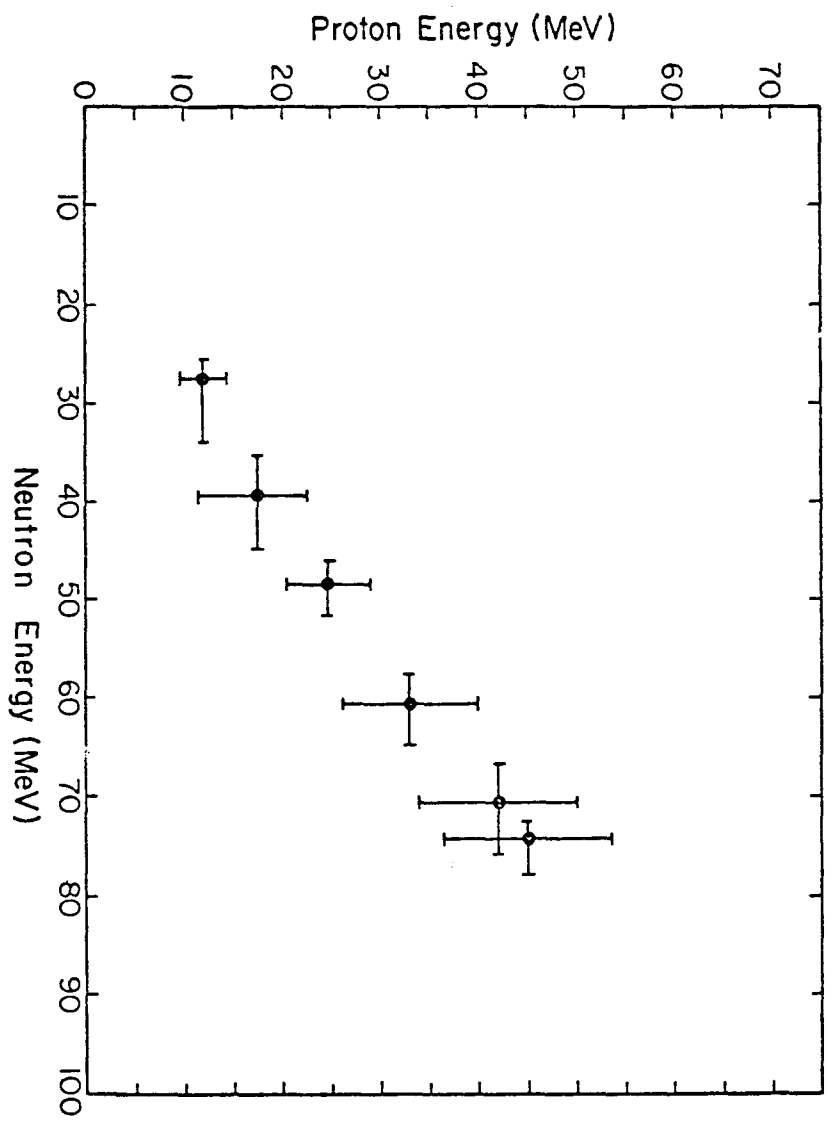
FIGURE 7-14

FIGURE 7-15

FIGURE 7-16

PROTONS/Mev   (Arbitrary Scale)

E_p(Mev)

0

50

100

a

b

FIGURE 7-17

FIGURE 9-1

2"

Proton Recoil Spectrum
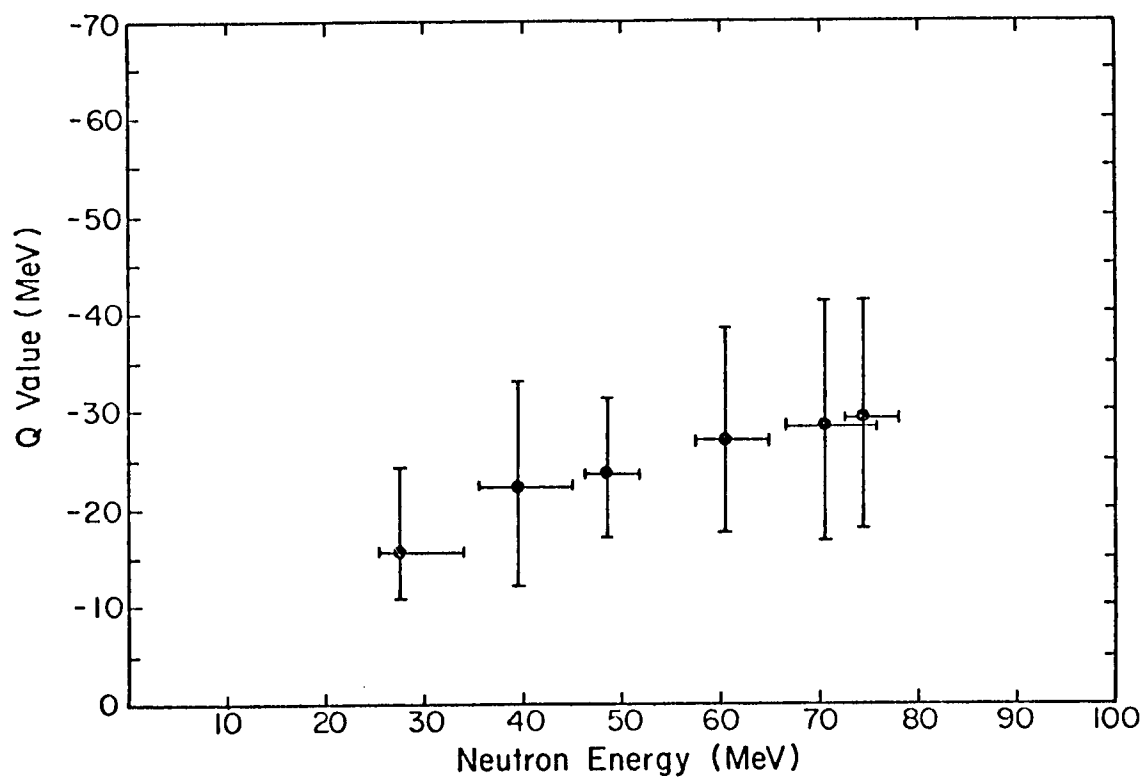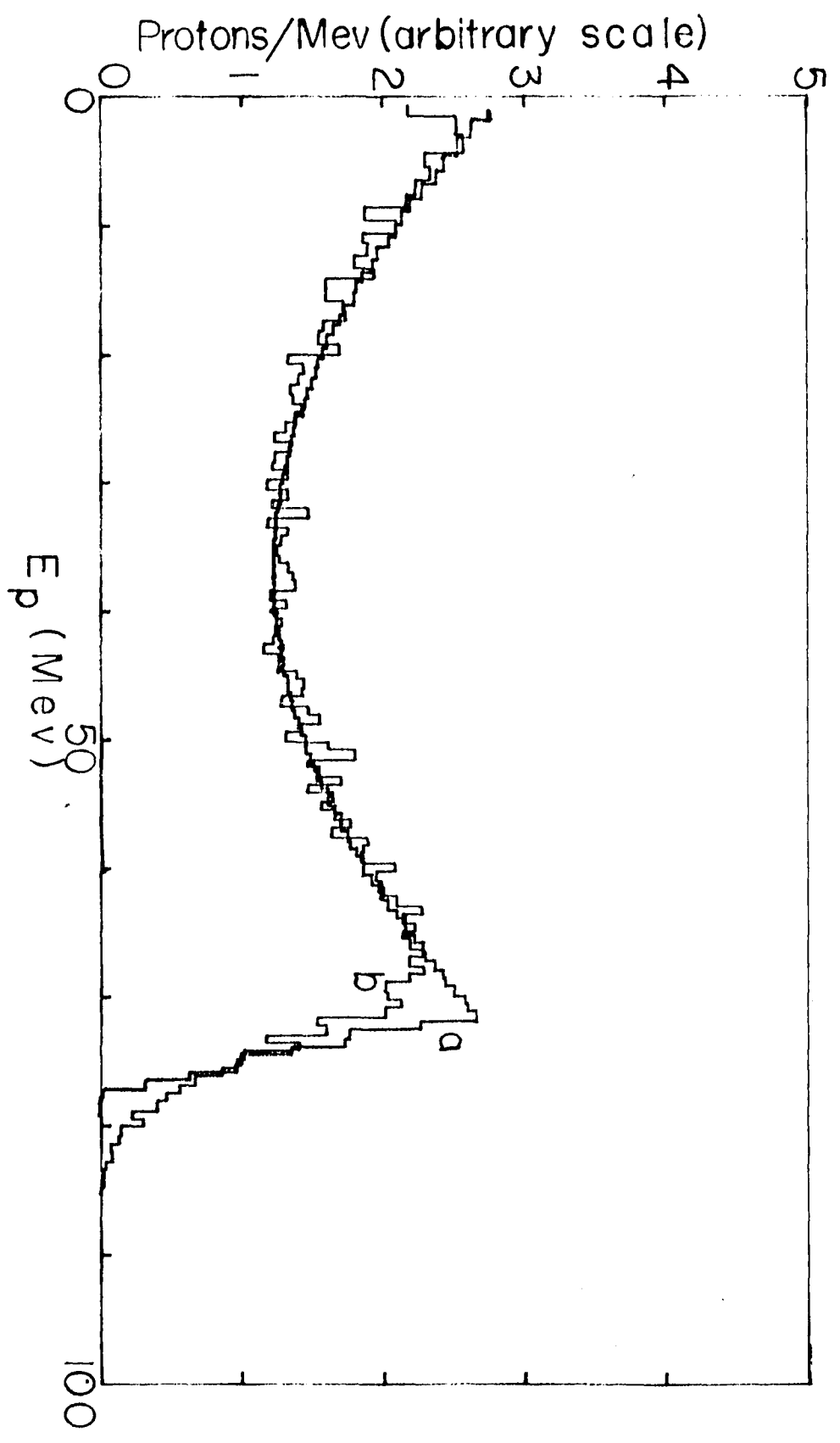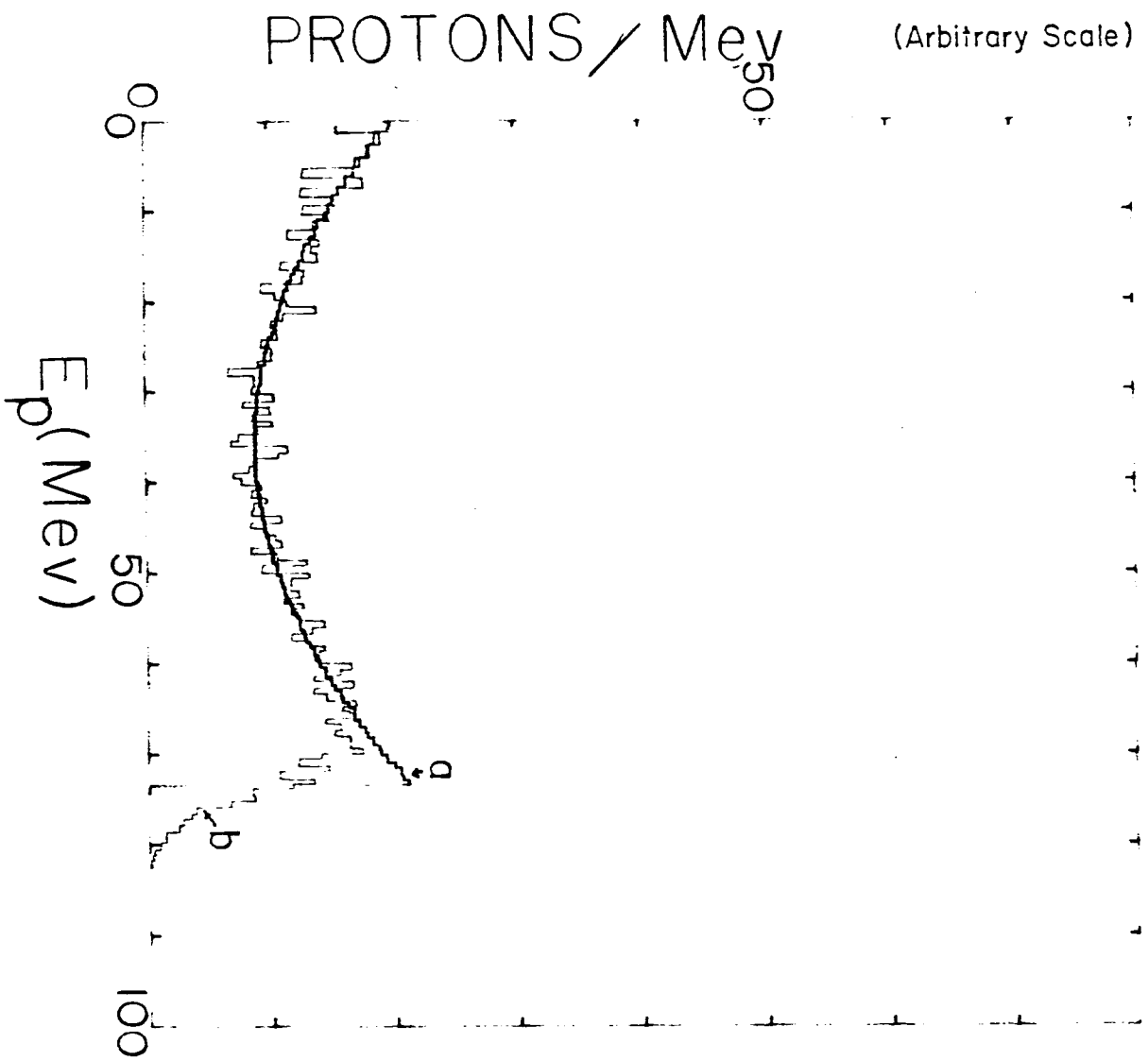
FIGURE 9-2

FIGURE 9-3

FIGURE 9-4

X scale: proton energy, 10 Mev/division

Y scale: 10 protons/Mev/division

NOTE: The base line is shifted one division in Y scale for every response function.

66Mev

69 Mev   (interpolation)

70.6 Mev   (interpolation)

          (calibration)

74.3 Mev

          (calibration)

77 Mev   (extrapolation)

80 Mev   (extrapolation)

PROTON ENERGY (Mev)

FIGURE 9-5

PROTON ENERGY (Mev)

FIGURE 9-6

Neutron Leakage
Solar Minimum
42° Geomagnetic Latitude

(high latitude)

Neutron Leakage Current (cm² sec MeV)⁻¹

Neutron Energy (MeV)

.... Newkirk (1963)
---- Lingenfelter (1963)
⌐L Armstrong & Chandler (1972)
⌐ Wilson, Lambiotte & Foelsche (1969)
▪⊢ White, et al. (1972)
—·— Heidbreder, et al. (1970)
Freden & White (1962)
—⊢ Kanbach, et al. (1974)
This Experiment

FIGURE 10-1

Neutron Leakage
Solar Minimum
42° N Geomagnetic Latitude

Kanbach, et al. (1974)
—·—Albernhe and Talon (1969)
—·····—Haymes (1964)
—·—Holt, et al. (1966), Mendell (1971)
·······Jenkins, et al. (1971)
White, et al. (1972)
——Lingenfelter (1963)
········Baird and Wilson (1966)
————Klumpar, et al. (1973)
This Experiment

FIGURE 10-2

Calculated from Measured
Neutron flux at 5g/cm²
(Preszler et al,1974)

Measured Proton
Energy Spectrum

Calculated "best fit"

Lower Limit

Proton Energy (MeV)

Protons

FIGURE 10-3

FIGURE A-1

Probability (Arbitrary Scale)

Electron Energy (MeV)

1 MeV

2 MeV

3 MeV

4 MeV

5 MeV

FIGURE A-2

Probability (Arbitrary Scale)

Electron Energy (MeV)

6MeV

7MeV

8MeV

9MeV

10MeV

FIGURE A-3

FIGURE A-4

FIGURE A-5

FIGURE A-6

FIGURE A-7
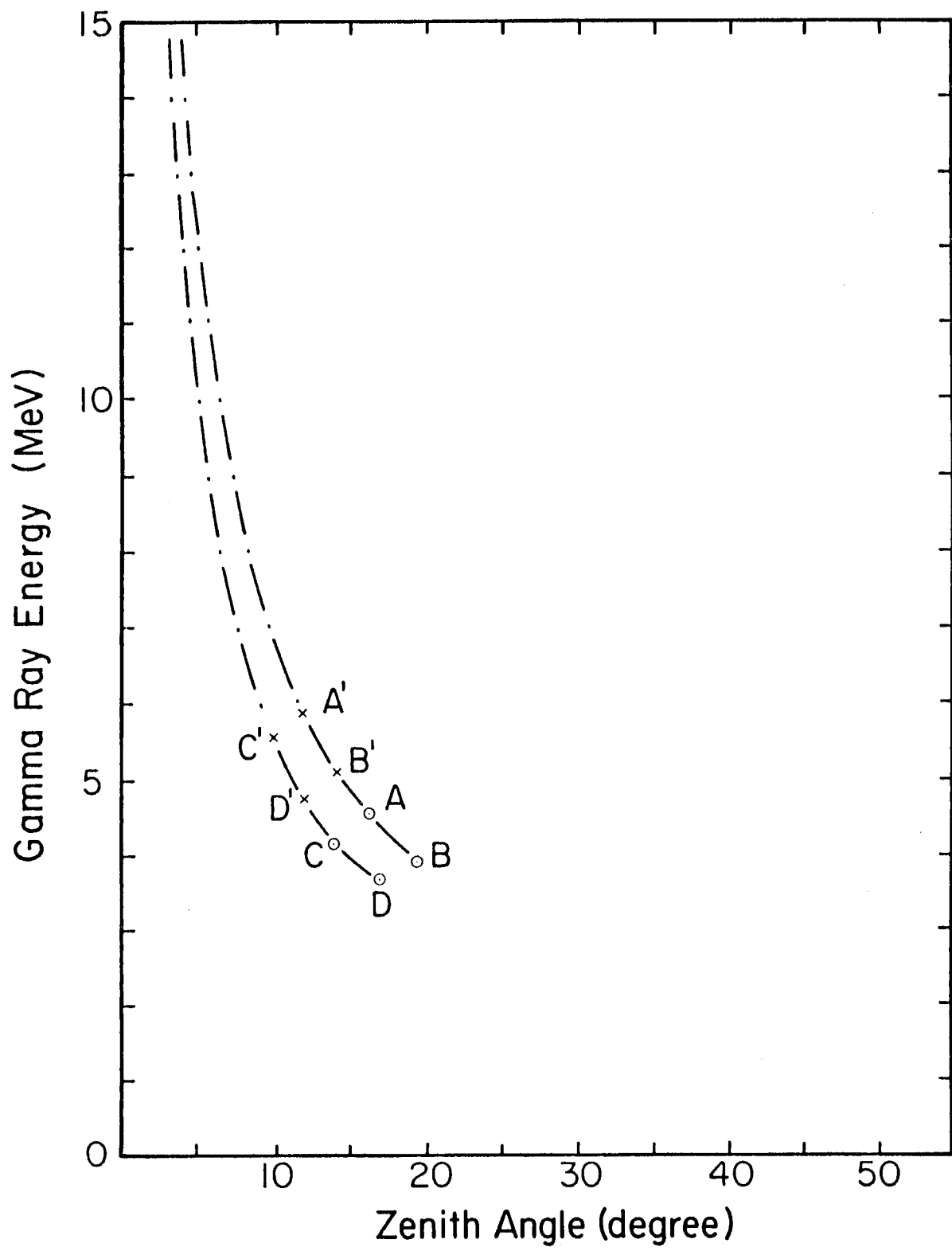
FIGURE A-8
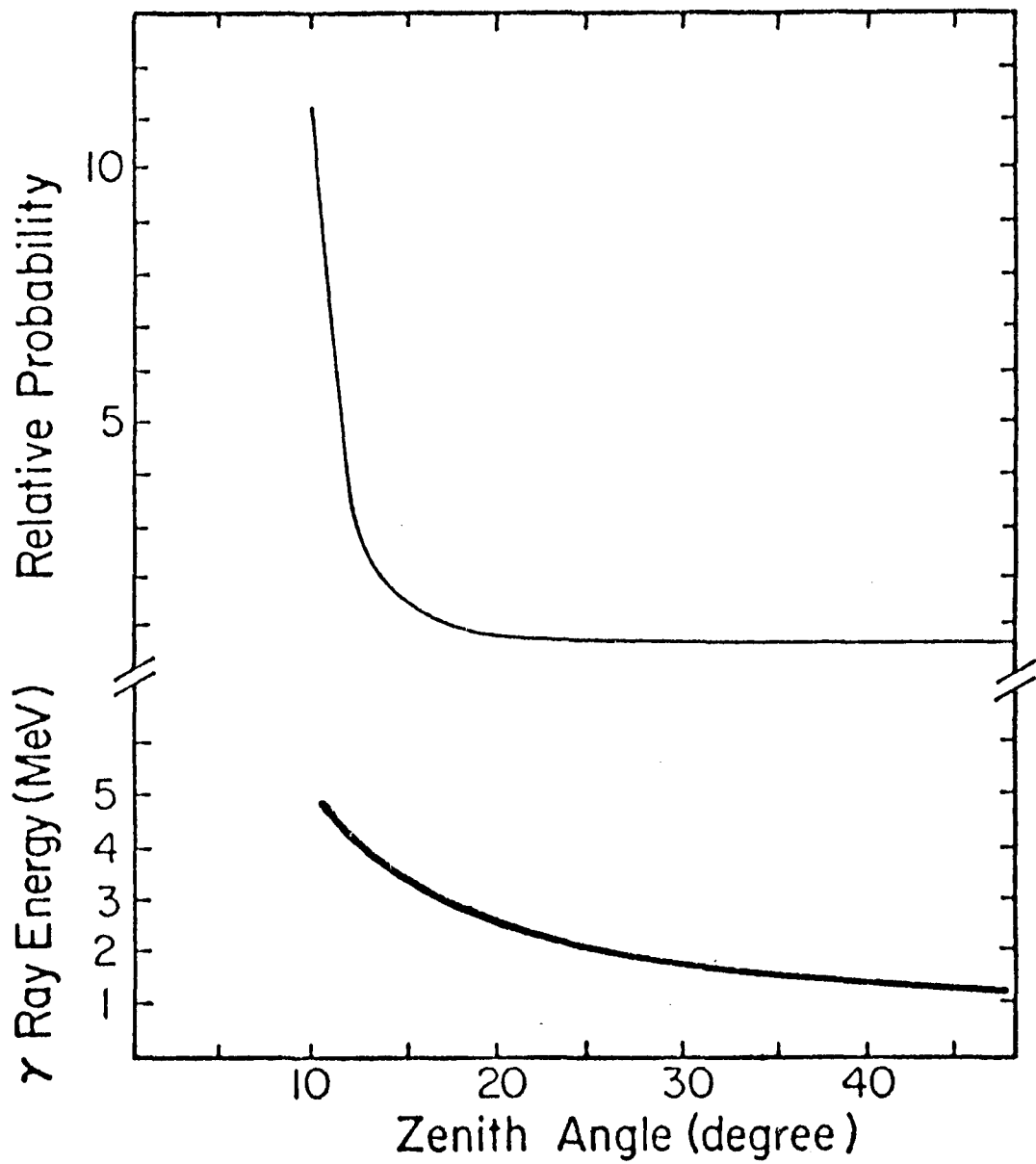
FIGURE A-9
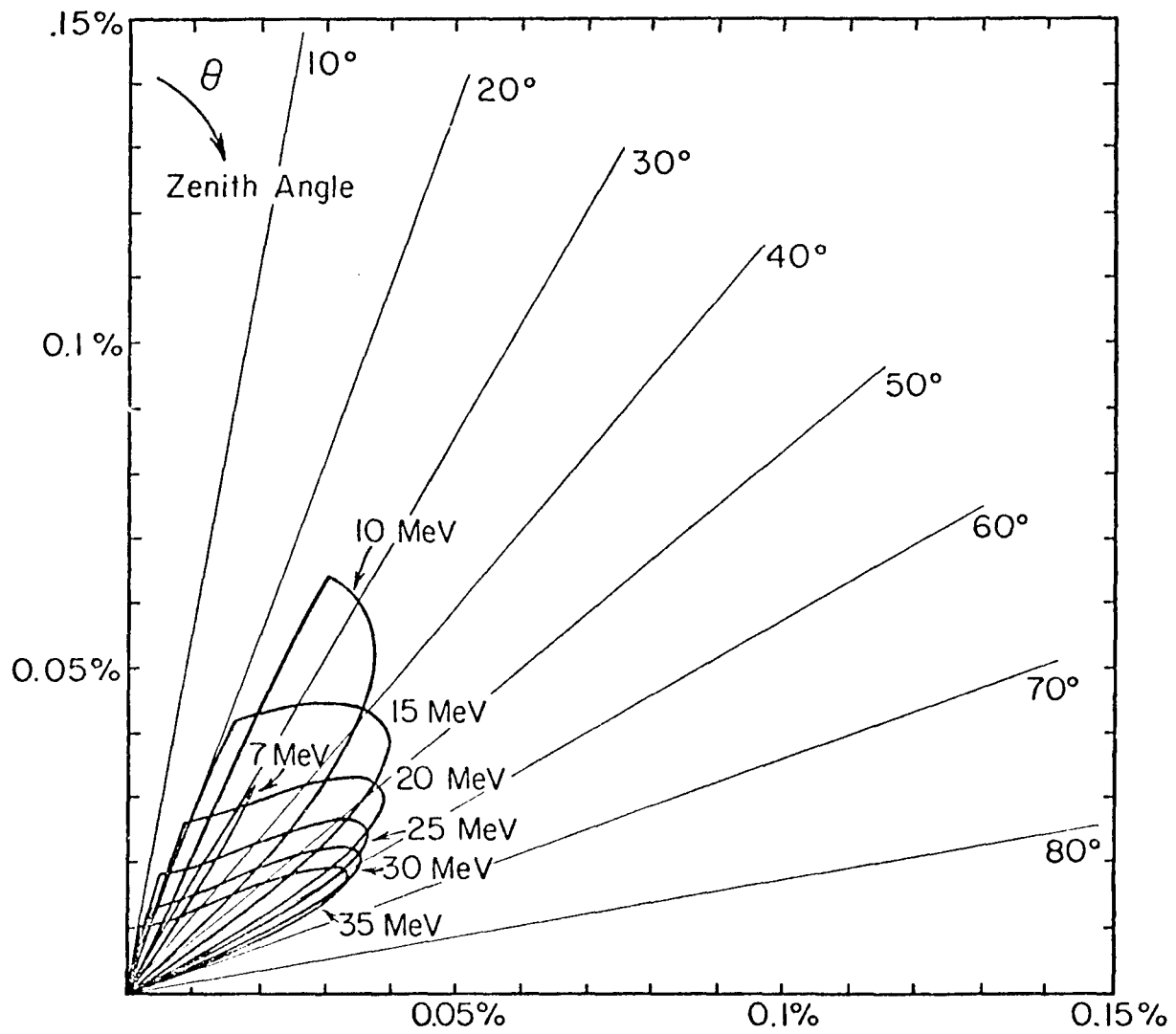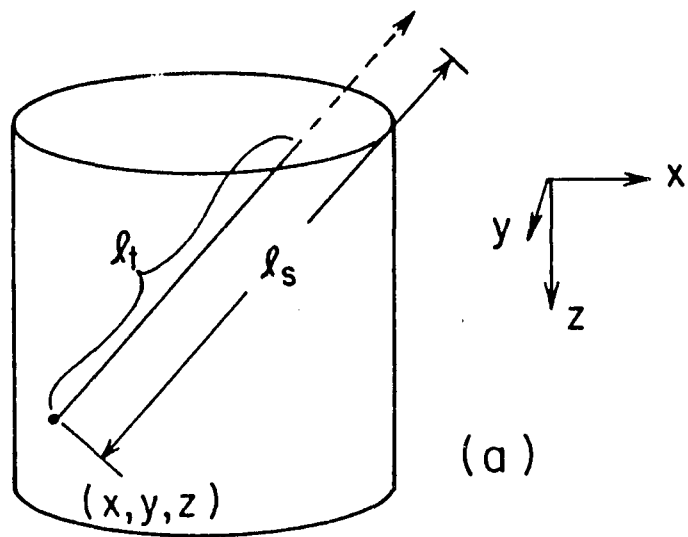
FIGURE A-10
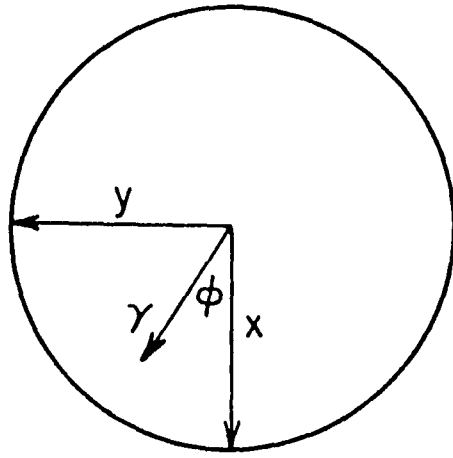
$$A_1 = \pi R^2$$
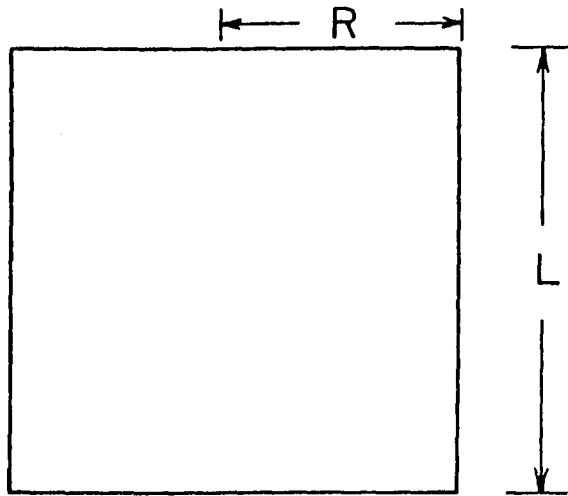
$$A_2 = L \times 2R$$

FIGURE B-1

FIGURE B-2
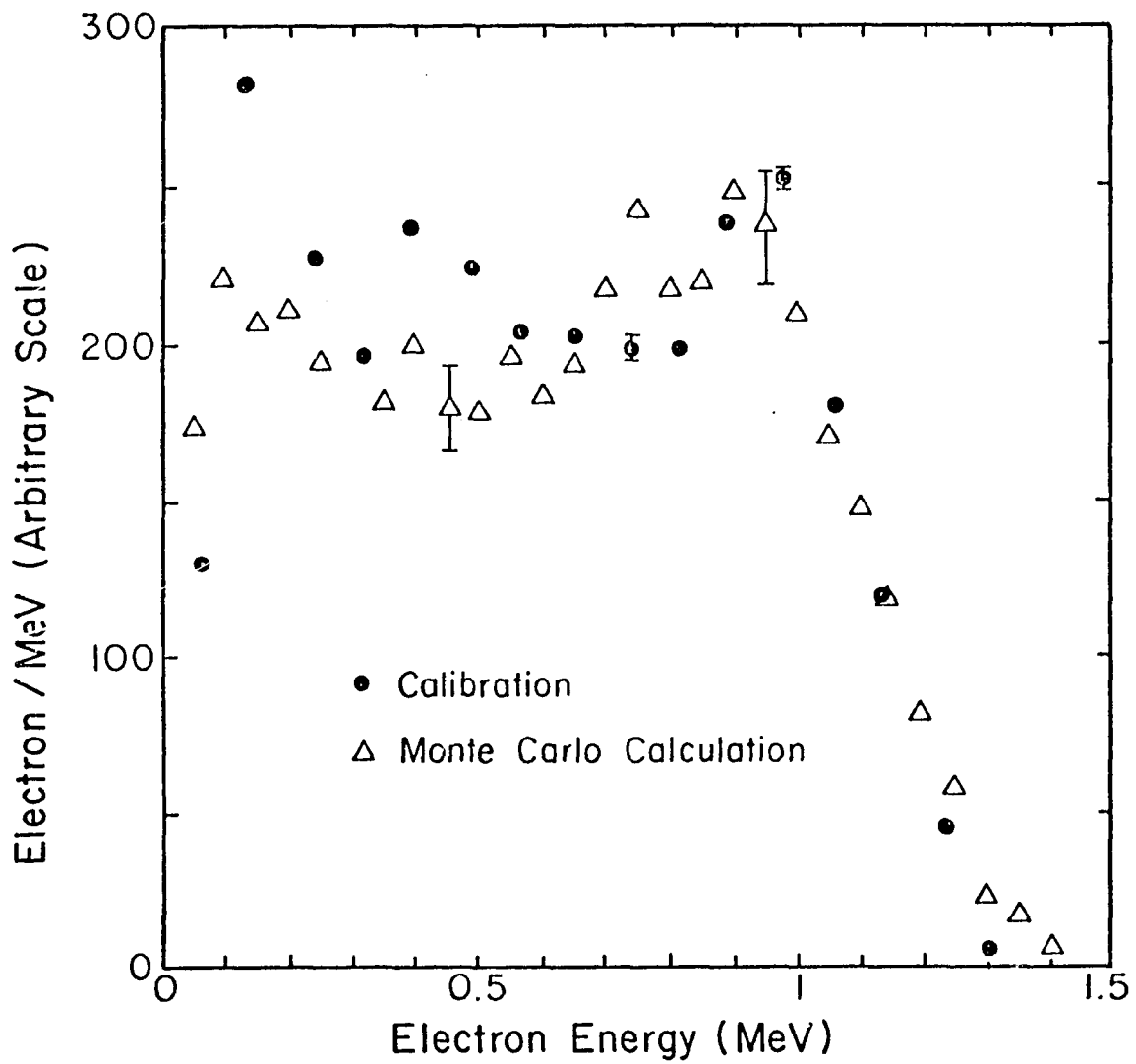
FIGURE B-3

Proton Recoil Spectrum

-----Down Flux Mode

——— Up Flux Mode

——— Horizontal Flux Mode

FIGURE C-1